Forschungszentrum Karlsruhe
Technik und Umwelt

Wissenschaftliche Berichte

FZKA 6388

Status Report on experiments and modelling of the cleavage fracture behaviour of F82Hmod using local fracture criteria

(Task TTMS-005)

H. Riesch-Oppermann, M. Walter

Institut für Materialforschung
Projekt Kernfusion
Association Forschungszentrum Karlsruhe / EURATOM

Forschungszentrum Karlsruhe GmbH, Karlsruhe

2001

Impressum der Print-Ausgabe:

Als Manuskript gedruckt

Forschungszentrum Karlsruhe GmbH
Postfach 3640, 76021 Karlsruhe

Mitglied der Hermann von Helmholtz-Gemeinschaft
Deutscher Forschungszentren (HGF)

ISSN 0947-8620

Abstract

Within the European Fusion Technology Programme framework, a fracture mechanics description of the material behaviour in the ductile to brittle transition-regime is developed using local fracture criteria. Based on experimental results using axisymmetrically notched and pre-cracked specimens together with a numerical stress analysis at fracture load, a statistical evaluation of cleavage fracture parameters can be performed along the lines described in various code schemes such as the British Energy R6-Code or the ESIS P6 procedure.

The report contains results of the experimental characterization of the deformation and fracture behaviour of the fusion candidate RAFM steel variant F82Hmod, details and background of the numerical procedure for cleavage fracture parameter determination as well as additional statistical inference methods for transferability analysis. Fractographic results give important information about fracture mode and fracture origin sites and their location. Numerical prediction of fracture origin distribution is an important tool for transferability assessment.

Future issues comprise constraint effect and ductile damage as well as incorporation of irradiation effects, which are topically addressed.

The methodology developed and described in the present report will be applied to characterize material behaviour of future RAFM variants as the EUROFER 97, for which analysis is currently under way.

Zusammenfassung

Beschreibung des Sprödbruchverhaltens des niedrigaktivierbaren Stahles F82Hmod mit Hilfe lokaler Versagenskriterien

Innerhalb des Europäischen Fusionsprogramms wird eine bruchmechanische Beschreibung des Materialverhaltens im Bereich des spröd-diktilen Übergangs auf Basis lokaler Versagenskriterien angestrebt. Auf Grundlage von geeigneten Experimenten an gekerbten sowie angerissenen Rundzugproben erfolgt mittels numerischer Auswerteprozeduren eine statistische Beschreibung der Sprödbruchparameter entsprechend der in verschiedenen Regelwerken bereits eingearbeiteten Verfahren.

Der vorliegende Bericht enthält Ergebnisse und Grundlagen der Modellierung für den niedrigaktivierbaren japanischen Stahl F82Hmod. Fraktografische Analysen geben Auskunft über Bruchmodus und Art sowie Verteilung der Bruchursprünge. Mittels ebenfalls bestimmter numerischer Vorhersagen der Verteilung der Bruchursprünge erhält man ein wichtiges Hilfsmittel für Übertragbarkeitsaussagen.

Kurz gestreift werden weiterführende Themen wie Einfluss von Dehnungsbehinderung oder starker Spannungsgradienten, duktiler Schädigung sowie die Berücksichtigung von Bestrahlungseffekten.

Eine Fortführung der hier dargestellten Arbeiten wird augenblicklich mit der Charakterisierung der europäischen Variante EUROFER97 eines niedrigaktivierbaren Stahls durchgeführt.

Contents

List of Figures

List of Tables

1

Introduction

The present analysis is part of the **EURATOM Fusion Technology - Blanket** programme for 1999 to 2002. It was related to the former Work Package SM 5 **Structural Materials**, the Task 5.2 **Fracture Mechanics Concept** and the subtask 5.2.1 **Local Fracture Criteria for EUROFER in the DBT regime** and is now incorporated within the **EFDA Technology Workprogramme 2001** under EFDA Reference TT MS - 005 **RAFM STEELS: Rules for Design, Fabrication, and Inspection**.

Within this framework, it is intended to develop a fracture mechanics concept for the description of the ductile-to-brittle-transition behaviour of ferritic-martensitic steels and to incorporate the concept into the structural design codes. Due to the need of transferability, a concept based on the mechanisms of ductile or brittle behaviour is indispensable for the assessment of size and geometry effects, irradiation effects, and effects due to complex mechanical as well as thermal loading conditions.

In contrast to the global approaches, where geometrical limits on validity of test results are imposed to ensure transferability of test data to component design, a local approach relies on the combination of local (i.e. micro-structurally based) fracture criteria and stress field analyses of selected geometries to ensure the transferability of material data. That is, within a local approach transferability is inherently guaranteed as long as the local fracture mechanism remains unchanged, which has to be verified by suitable investigations of the fractured specimens.

A key issue of the local fracture description is the determination of the fracture parameters, which requires considerable (numerical and experimental) efforts. Fracture parameters are obtained by numerical Finite Element (FE) elasto-plastic deformation analyses of fracture tests. In the case of brittle fracture, a statistical approach is necessary because of the inherent scatter. If the metallographic investigations of fractured specimens indicate that ductile damage precedes final cleavage fracture, changes in the stress field have to be accounted for by appropriate damage models and competing failure modes of ductile and cleavage fracture have to be appropriately incorporated into the statistical fracture modelling.

The present report is a compilation of results obtained during characterization experiments on the Japanese F82Hmod RAFM steel. It contains both experimental results, which serve as a database for the applicability of local fracture criteria, and modelling achievements. Modelling is concerned with material behaviour of deformation and fracture as well as with the development of statistical inference approaches that are necessary for transferability assessment.

In Chapter 2, some basic information about background and application of local approach methods is given.

Chapter 3 contains relations for numerical analysis of cleavage fracture parameters and the calculation of Weibull stresses from experimental data including statistical evaluation using maximum likelihood methods. The local risk of rupture is introduced which enables prediction of fracture origin distribution and thus verification of fracture modelling by experiments.

Chapter 4 gives background and results of a novel statistical approach based on resampling method which is a useful statistical inference tool that goes beyond the limits of conventional maximum likelihood methods.

Chapter 5 contains the results on deformation behaviour of smooth axisymmetric specimens and subsequent specimen design while Chapter 6 covers fracture behaviour and Weibull stress results of the F82Hmod RAFM steel under investigation obtained at notched and pre-cracked axisymmetric specimens.

In Chapter 7, a summary of future work or work outside the scope of the present report is given together with the state of development that is available today. This includes irradiation damage, multiaxial loading, constraint effects and dynamic failure.

1.1 Objective

Main objective of the work presented in this report is to characterize the F82Hmod steel using the methodology of the Local Approach as well as to develop numerical tools for the statistical characterization of uncertainties in the material parameters that characterize cleavage fracture. For the comparison between experimental results and numerical predictions, the local risk of rupture was used. The local risk of rupture is available from fractographic analyses via the distribution of fracture origin locations. Predictions of the local risk of rupture require statistical treatment and a suitable numerical integration procedure, which was developed within this subtask.

Evaluation of cleavage fracture parameters is currently under standardization efforts in different contexts (SINTAP [50], R6 [8], ESIS [21], ASTM [19]). Part of the procedures developed and presented in the report were tested and verified within an ESIS round robin [55].

1.2 Outlook

The characterization of cleavage fracture as described in this report is currently performed for the European variant of a RAFM steel, EUROFER 97 [56]. Results will provide an extended data base for future modelling efforts.

For design considerations, simplified approaches may be of some value as described e.g. in Ref. [17], where a parametrized description of material behaviour is used to obtain suitable design curves.

Various authors deal with implications of irradiation effects on fracture toughness, e.g. [46, 48, 62, 74, 75]. The basic effect of irradiation on fracture toughness is a shift of the ductile-to-brittle transition temperature (DBTT) towards higher values and a reduction of the upper shelf Charpy energy. Unfortunately, DBTT of Charpy and fracture toughness data do not coincide. It is claimed [74] that the Charpy-V transition shift has a tendency to underestimate the true fracture toughness shift due to irradiation. In terms of local approach, irradiation damage is

described mainly by the influence on yield stress. It turned out that the critical cleavage stress is not affected by irradiation effects so that the basic framework of the local approach is therefore easily adopted and it is only necessary to identify a suitable description of irradiation hardening [46, 48].

Application of the local approach to Charpy test results was shown successfully by [64] and [67]. A modelling of the strain-rate dependent deformation material behaviour is required, which is also a matter of the available data base.

2

Background

Body-centered cubic materials exhibit a transition from brittle (low toughness, cleavage) fracture behaviour at low temperature to ductile (microvoid initiation and coalescence) fracture at high temperature. In the transition regime, the material is characterized by a large scatter of toughness [9] and the presence of a pronounced size effect of critical toughness parameters such as K_{Ic} or J_c [40]. This behaviour can be described using ideas known as "Local Approach" [5].

2.1 Physical description of fracture processes

The basic background of this methodology is that global failure of the material is triggered by the local behaviour in the vicinity of stress concentrations [61]. In the cleavage regime, fracture is caused by unstable growth of crack initiation sites whose activation is thought to coincide with the onset of plastic deformation [69]. The worst (in some sense) initiation site is determining failure, which leads to an extreme value distribution of the fracture (toughness) parameter. Basic assumptions which are essential for the validity of the model are that the possible initiation sites are statistically independent and (for fracture mechanics specimens) that the stress field obeys small scale yielding (SSY) conditions. Also, it is essential that the fracture mode is purely cleavage and that there is no void initiation (i.e. no ductile damage). If these basic assumptions are violated, modification of the model is necessary to take into account the effects of gross yielding and of microvoid initiation [6].

Result of the model is the description of the dependence of toughness parameters like K_{Ic} or J_c of temperature as well as the scatter of the parameters in the different temperature regimes.

In the ductile regime, the fracture mechanism is characterized by the formation and growth of voids from inclusions. Void formation is thought to coincide with the onset of plastic deformation, the initial void volume fraction thus given by precipitations, inclusions etc.. The growth rate of voids triggered by stress triaxiality is given in the model of Rice & Tracey [54], its corrections [30] or other models, e.g. Gurson [32, 65]. Main purpose of the "Local Approach" is to combine stress and strain field analyses with micro-structural features of the material causing failure events. This approach allows predictions with respect to size effects and with respect to scatter in the material behaviour at the expense of an increased numerical effort.

2.2 Historical development of Local Approach ideas

Basic ideas of the Local Approach for cleavage fracture have its foundation in a long tradition of micro-mechanical investigations, theoretical as well as using fractography which all aim at a fundamental understanding of the fracture processes on a microscopic scale. Among others, there are Stroh [69] (formation of micro-cracks within grains due to inhomogeneous plastic deformation), Ritchie et al. [33, 62], Rosenfield [63], Hahn [28] etc. Substantial progress was made during the last years with the advent of more powerful computers. Accurate numerical analysis of stress and strain fields even for cracked specimens is possible with moderate effort.

Essential ingredients for a successful application of the ideas of the Local Approach consist of firstly a precise description of the initiation of unstable crack propagation and an exact description of the stress field in the material. Also an appropriate statistical treatment of the experimental data and its numerical evaluation is essential. Fractography is indispensable for an appropriate interpretation of the applied model and also to ensure that the basic assumptions of the model with respect to the fracture mode are justified.

Recent efforts to model cleavage by self-consistent models of dislocation arrangements in the vicinity of a crack tip and their impact on crack propagation and cleavage fracture should be mentioned [4], but are not feasible for an engineering level of modelling.

Local fracture criteria in the ductile regime rely on models of void formation, growth [30, 32, 54, 65], and coalescence [72, 73].

In the transition regime, competition between cleavage and ductile fracture is present and governs the failure behaviour. While uncoupled models essentially consider void formation in a stress field of undamaged material [2], coupled models contain the effect of damage on the stress field [39]. Uncoupled models have some application in the post-processing of existing results, where stress field solutions are already available, while new problems are usually analysed using coupled models that are currently available in most academic as well as commercial FE codes.

For intergranular brittle fracture and multiaxial loading conditions, [37] provide a verification of the Beremin model after observation of the orientation of fracture surfaces and the necessity of plastic deformation for the initiation of brittle fracture.

3

Numerical analysis of cleavage fracture parameter in the lower shelf regime

Cleavage fracture is a process that is triggered by micro-crack formation and propagation within the material. Micro-crack formation is a local process and governed by the microstructure of the material. Inhomogeneous plastic deformation leads to yielding of suitably oriented grains and causes dislocation pileups that lead to the formation of a population of micro-cracks im the material. The size and orientation of the micro-cracks depend on the microstructure of the material, especially on inhomogeneities such as precipitations, grain boundaries, or inclusions. While in the beginning most of the initiating cracks remain stable and do not propagate, with increasing load level, the stress acting on a certain micro-crack may exceed its critical value and unstable fracture will lead to final failure.

The overall stress level at which final failure occurs will depend on the size of the micro-crack; for inhomogeneous stress fields, it will also depend on its location and orientation. The size of the micro-crack is random, micro-cracks will also be distributed randomly within the material so that location and orientation are random quantities as well.

Final cleavage fracture is therefore a stochastic event and has to be treated accordingly.

The stochastic variable that is used for cleavage fracture modelling is called the Weibull stress. It is obtained by an elasto-plastic analysis of the stress field at fracture. A suitably chosen loading parameter is necessary which is accessible experimentally and numerically.

The basic relations and numerical procedure of the Weibull stress analysis, known as the local approach to cleavage fracture, are given in the following section. After that, statistical analysis of experiments is addressed leading to distribution parameters of the Weibull stress. Finally, statistical uncertainties are investigated.

3.1 Basic relations and numerical procedure

The basic line of arguments in the establishment of Local Approach in the field of cleavage fracture ([2, 5, 37, 44]) are based on some essential assumptions which are summarized below. The reasoning which leads to the essential relations that govern Weibull stress considerations is given in the sequel. The following assumptions characterize the micromechanical and statistical model:

- There is a large population of weak spots in the material, which can be modelled in the framework of fracture mechanics (e.g. as penny-shaped cracks)
- Failure of the material starts from and is triggered by the most dangerous 'weak spot'
- The weak spots are randomly distributed within the material
- The weak spots are acting independently, i.e. there is no interaction
- The weak spots become 'active' with the onset of plastic deformation, i.e. only weak spots within the plastic zone are relevant for failure
- The size of the weak spots is a random variable
- The critical size of a weak spot is described within the framework of fracture mechanics through a relation of the form

$$a_c(\vec{r}) = \frac{W_p}{\sigma_c^2(\vec{r})} \tag{3.1}$$

where W_p contains parameters of the material relevant for fracture resistance as well as crack geometry parameters and σ_c is the stress at location $\vec{r}$ that is responsible for fracture (usually the first principal stress).

Based on these assumptions, the probability for failure of a single weak spot is just the probability that its size a exceeds the critical size a_c (Eqn. 3.1) and is given by the relation

$$P(a > a_c) = \int_{a_c(\vec{r})}^{\infty} f_a(a)\,\mathrm{d}a \tag{3.2}$$

where f_a is the probability density of the size distribution of the weak spots.

Now we are prepared to calculate the probability of failure for a given specimen or component.

We will proceed in two steps. In the first step, *Step 1*, we will assume, that there is *exactly one* weak spot in the specimen. In the second step, *Step 2*, we will take into account the contribution of a random number of k weak spots per specimen.

Step 1 - One weak spot of random size in the specime n

We calculate the probability Q_1 for the weak spot to cause failure of the specimen. Q_1 is given by

$$Q_1 = \frac{1}{V_{pl}} \int_{V_{pl}} \int_{a_c(\vec{r})}^{\infty} f_a(a)\,\mathrm{d}a\,\mathrm{d}V \tag{3.3}$$

where f_a is the probability density of the size distribution and V_{pl} denotes the volume of the plastic zone. Here, it is assumed that weak spots are distributed randomly within the plastic zone and that the location of the weak spots follows a uniform distribution. Thus, V_{pl} can be interpreted as a normalization parameter of the location distribution and $dV_{pl}\ /V_{pl}$ is the probability of having a weak spot in a randomly chosen volume dV_{pl} at an arbitrary location within the plastic zone. Now we proceed to

Step 2 - k weak spots in the specimen

We now assess the probability for at least one out of a random number of k weak spots in the specimen to cause failure. If we have k independent weak spots, the survival probability R_k of the specimen is

$$R_k = (1 - Q_1)^k \tag{3.4}$$

where Q_1 is the failure probability of one weak spot. If there is a mean number of M weak spots per unit volume, the probability p_k of having exactly k weak spots in the plastic zone is given by the POISSON distribution with mean MV_{pl} and leads to

$$p_k = \frac{(MV_{pl})^k}{k!} \exp(-MV_{pl}) \tag{3.5}$$

We obtain the survival probability P_s of the specimen by summing up the contributions for all possible numbers of weak spots in the specimen

$$P_s = \sum_{k=0}^{\infty} p_k R_k \tag{3.6}$$

and, using Eqns. (3.4) and (3.5), we finally end up with the relation

$$P_s = \exp(-MV_{pl}Q_1) \tag{3.7}$$

which leads to the failure probability P_f of the following form:

$$\begin{aligned} P_f &= 1 - P_s \\ &= 1 - \exp\left(-MV_{pl}Q_1\right) \\ &= 1 - \exp\left(-M \int\limits_{V_{pl}} \int_{a_c(\vec{r})}^{\infty} f_a(a)\,\mathrm{d}a\,\mathrm{d}V \right) \end{aligned} \tag{3.8}$$

To determine the failure probability P_f, some knowledge of the size distribution of the weak spots is necessary. Assuming a decay of the probability density f_a which is of a power-law type: $f_a(a) \propto a^{-n}$, the second integral of Eqn. (3.8) takes on the following form:

$$\int_{a_c(\vec{r})}^{\infty} f_a(a)\,\mathrm{d}a = \frac{C}{n-1} a_c(\vec{r})^{-(n-1)} \tag{3.9}$$

with a normalization constant C. With Eqns. (3.1) and (3.9) we obtain Q_1 from Eqn. (3.3) as

$$Q_1 = \frac{C}{(n-1)W_p^{n-1}} \frac{1}{V_{pl}} \int\limits_{V_{pl}} \sigma_c^{2(n-1)}\,\mathrm{d}V \tag{3.10}$$

and it is now possible to define a new variable termed the Weibull stress σ_W. This is done by inserting Q_1 into Eqn. (3.8) and observing that we may write P_f in the following alternate form:

$$P_f = 1 - \exp\left(-\left(\frac{\sigma_W}{\sigma_u}\right)^m\right) \tag{3.11}$$

with σ_W defined through

$$\sigma_W^m = \frac{1}{V_0}\int_{V_{pl}} \sigma_c^m \, dV \qquad \text{with} \qquad m = 2(n-1) \tag{3.12}$$

and σ_u defined through

$$\sigma_u^m = \frac{(n-1)W_p^{n-1}}{MV_0C} \tag{3.13}$$

so that it is possible to interpret the failure probability P_f as the value of the cumulative distribution function of the Weibull stress σ_W at failure:

$$\begin{aligned} P_f &= F_{\sigma_W}(\sigma_W) \\ &= 1 - \exp\left(-\left(\frac{\sigma_W}{\sigma_u}\right)^m\right) \end{aligned} \tag{3.14}$$

This means, that we have introduced the Weibull stress σ_W as a random variable that characterizes the fracture resistance of the material against cleavage (brittle) fracture. The Weibull stress σ_W at failure is a material parameter (i.e. it is independent of the stress state in the material) but may depend on temperature. (Recent work, however, indicates that this is perhaps not the case [29].) The Weibull slope m characterizes the scatter of the Weibull stress. The C.O.V (coefficient of variation) of σ_W is a function of m alone and given by

$$COV_{\sigma_W} = \frac{\sqrt{\Gamma(1+\frac{2}{m}) - \left(\Gamma(1+\frac{1}{m})\right)^2}}{\Gamma(1+\frac{1}{m})} \tag{3.15}$$

(see Fig. 3.1). The parameter σ_u gives the $1-1/e$ (=63.2%)-quantile of σ_W.

The unit volume V_0 which appears in eqns. (3.12) and (3.13) is introduced for dimensional purposes only and is usually set to 1mm^3. [1]

For the analysis, the Weibull stress at fracture has to be determined from suitably chosen experimental loading parameters, such as e.g. the diameter reduction for notched tensile specimens at fracture or the value of the J-integral for cracked specimens.

[1] Some authors use V_0 as an additional parameter related to σ_u (see e.g. [5, 44]) chosen to be small enough that stress gradients can be neglected and large enough that the weakest link argument for finding a micro-crack of a given size still holds (e.g. 10 grains). If stress gradients are important for the fracture behaviour, this can be directly incorporated into the fracture model leading to eq. (3.14) at the expense of losing the meaning of σ_u and m as material parameters (see Chapter 7).

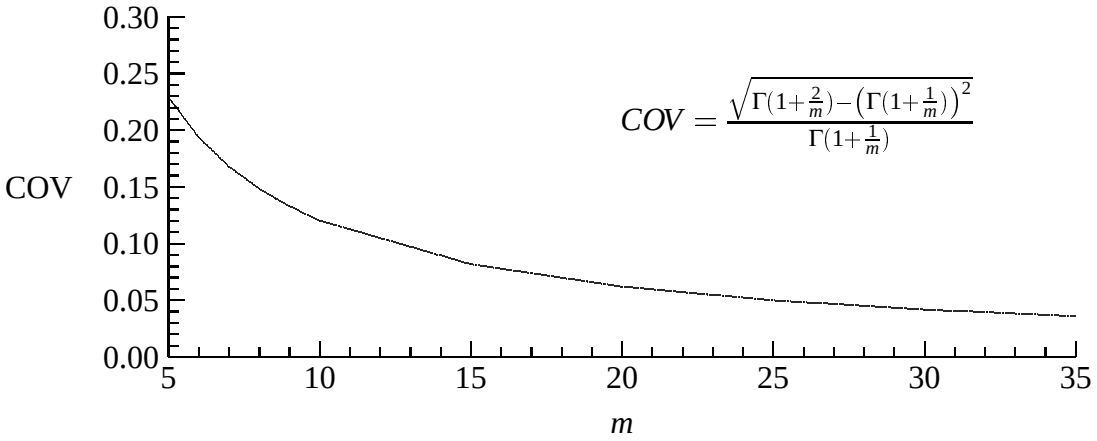

Figure 3.1: COV of Weibull distributed random variate for different moduli m

3.2 Numerical integration of finite element stress results

For numerical reasons, the integration of the Weibull stress according to eq. (3.12) is performed after normalizing σ_1 by a suitably chosen reference stress, e.g. the flow stress. This is done to avoid numerical difficulties resulting from large values of the Weibull exponent m which is typically in the range of 10-30. The correction is removed after the numerical integration is complete. Eq. (3.12) then reads:

$$\left(\frac{\sigma_W}{\sigma_{\text{ref}}}\right)^m = \frac{1}{V_0}\int_{V_{pl}} \left(\frac{\sigma_1}{\sigma_{\text{ref}}}\right)^m \mathrm{d}V \tag{3.16}$$

and final correction is simply made by multiplying the resulting integral value by the value of the reference stress σ_{ref}^m.

The first principal stress values σ_1 are obtained from the ABAQUS stress analysis with the help of the post-processing routine WEISTRABA described in [58]. Stresses are given at the integration points of the ABAQUS elements. Reduced integration is used, which means that we have 2x2=4 integration points per element in the 2D case and 2x2x2=8 integration points in 3D problems. The Weibull stress is integrated element-by-element. In the general case of a 3D model, we have

$$\begin{aligned} \sigma_W &= \sigma_{\text{ref}} \left[\frac{1}{V_0}\sum_{\text{el}} \sigma_{W_{\text{el}}}\right]^{\frac{1}{m}} \qquad \text{with the auxiliary quantity of} \\ \sigma_{W_{\text{el}}} &= \sum_{i=1}^{k_i} w_i \sum_{j=1}^{k_j} w_j \sum_{k=1}^{k_k} w_k \left(\frac{\sigma_1(r_i, s_j, t_k)}{\sigma_{\text{ref}}}\right)^m (\det J(r_i, s_j, t_k)) \end{aligned} \tag{3.17}$$

with k_i, k_j, k_k the number of integration points in each dimension and w_i, w_j, w_k the respective weights. The contributions from each element are summed up to give the final result. For $k_i = k_j = k_k = 2$, we have $w_i = w_j = w_k = 1$ and r_i, s_j, $t_k = \pm 1/\sqrt{3}$.

A plastic zone indicator flag is used to extend numerical integration only over the plastic zone and not over the entire volume of the specimen. This plasticity flag is set to 1 for each integration point where plasticity occurs (in terms of a von Mises yield criterion or by checking the plastic strains of the FE output) and 0 otherwise. Any averaging procedures are avoided. Only the stress values at the integration points, which are known to be the most exact values within an element [3], are used.

For each FE load step, corresponding to a specimen fracture event, the first principal stress values are checked against the values of the previous step and a stress envelope is constructed to take into account locally decreasing stresses due to stress redistribution which may lead to decreasing values of the local risk of rupture.

3.3 Statistical inference

Due to the large scatter present in cleavage fracture parameters, statistical inference methods are necessary. Point estimators and confidence bounds are obtained by using well established statistical inference methods such as the maximum likelihood method. In the statistical literature, special results are available for the parameter estimation in case of Weibull distributed random variates [71]. These results are used for initial parameter estimation and determination of confidence bounds. However, the use of maximum likelihood confidence bounds is of limited value because it turns out that the distribution parameters m and σ_u according to Eqn. (3.14) are not independent as can be seen from Eqn. (3.12).

If different samples have to be investigated with respect to compatibility, advanced statistical inference methods are preferred. These are addressed shortly and described in more detail in Chapter 4.

The maximum likelihood parameter estimates are used to calculate the local risk of rupture. The local risk of rupture is a useful quantity for the prediction of the fracture origin location distribution and allows comparison with fractographic results.

3.3.1 Maximum likelihood parameter estimation

The determination of the two parameters m and σ_u has to be performed iteratively as σ_W depends on the (unknown) parameter m [43].

Step 1: A starting value of e.g. $m = 20$ is used and the Weibull stress σ_W at fracture is calculated for each fractured specimen (i.e. at different load steps according to the experimental loading parameter) as described above.

Step 2: A plotfile is generated containing the results in increasing order of Weibull stress σ_W together with $\ln\ln[\frac{1}{1-\overline{F(x_{(i)})}}]$ as a function of $\ln x_{(i)}$, where $x_{(i)}$ is the Weibull stress of the specimen with rank i and $\overline{F(x_{(i)})} = \frac{i}{N+1}$ is the mean (cumulative) frequency of the i-th observation (using $\frac{i}{N+1}$ as plotting position is generally recommended for statistical reasons – e.g. [27] –, although it plays no role provided that the maximum likelihood

method is used for parameter estimation). As the theoretical relation between failure probability and σ_W is given by

$$P_f = 1 - \exp\left[-\left(\frac{\sigma_W}{\sigma_u}\right)^m\right] \quad ,$$

a plot of $\ln\ln[\frac{1}{1-\overline{F(\sigma_{W_{(i)}})}}]$ versus $\ln\sigma_{W_{(i)}}$, where $\sigma_{W_{(i)}}$ is the "experimental" Weibull stress for the specimen with rank i, should give an approximately linear relation.
(Step 2 is only for illustration and not necessary for Step 3)

Step 3: The maximum likelihood method is used to determine the parameters m and σ_u of the Weibull distribution of the Weibull stress. The maximum likelihood estimators of m and σ_u are denoted by $\hat{m}$ and $\widehat{\sigma_u}$, respectively. $\hat{m}$ is the solution of the non-linear equation

$$\frac{N}{\hat{m}} + \sum_{i=1}^{N} \ln\sigma_{W_{(i)}} - N\frac{\sum_{i=1}^{N}\sigma_{W_{(i)}}^{\hat{m}}\ln\sigma_{W_{(i)}}}{\sum_{i=1}^{N}\sigma_{W_{(i)}}^{\hat{m}}} = 0$$

which is obtained by an interval sectioning procedure. Using $\hat{m}$, the maximum likelihood estimator $\widehat{\sigma_u}$ is obtained from the equation

$$\widehat{\sigma_u} = \left(\frac{1}{N}\sum_{i=1}^{N}\sigma_{W_{(i)}}^{\hat{m}}\right)^{\frac{1}{\hat{m}}}$$

The parameter $\hat{m}$ is corrected with the unbiasing factor $b(N)$ [71]:

$$\hat{m}_{unb} = \hat{m} * b(N)$$

(see also Table B.5).

Step 4: If the maximum likelihood estimators $\widehat{\sigma_u}$ and $\hat{m}_{unb}$ agree within a fixed tolerance with those of the previous iteration, their values are considered acceptable. Otherwise, steps 2-4 are repeated. A flow diagram is given in Figure 3.2 on page 14 to illustrate the iterative procedure.

3.3.2 Maximum likelihood confidence intervals for m and σ_u

Confidence intervals for the Weibull parameters m and σ_u determined by the maximum likelihood method are obtained according to the following procedure:

1. For a confidence level $1-\alpha$ (80 %, 90% or 96% is possible, i.e. $\alpha = 0.20$, $\alpha = 0.10$ or $\alpha = 0.04$) $\alpha_1 = \alpha/2$ and $\alpha_2 = 1-\alpha/2$ are calculated.

2. $t_1(N, \alpha_1)$ and $t_2(N, \alpha_2)$ are taken from Table B.6
   $A = \widehat{\sigma_u} * \exp(-t_2/\hat{m})$ and $B = \widehat{\sigma_u} * \exp(-t_1/\hat{m})$ are calculated.
   $[A, B]$ is reported to be the confidence interval for σ_u for a confidence level of $1-\alpha$.

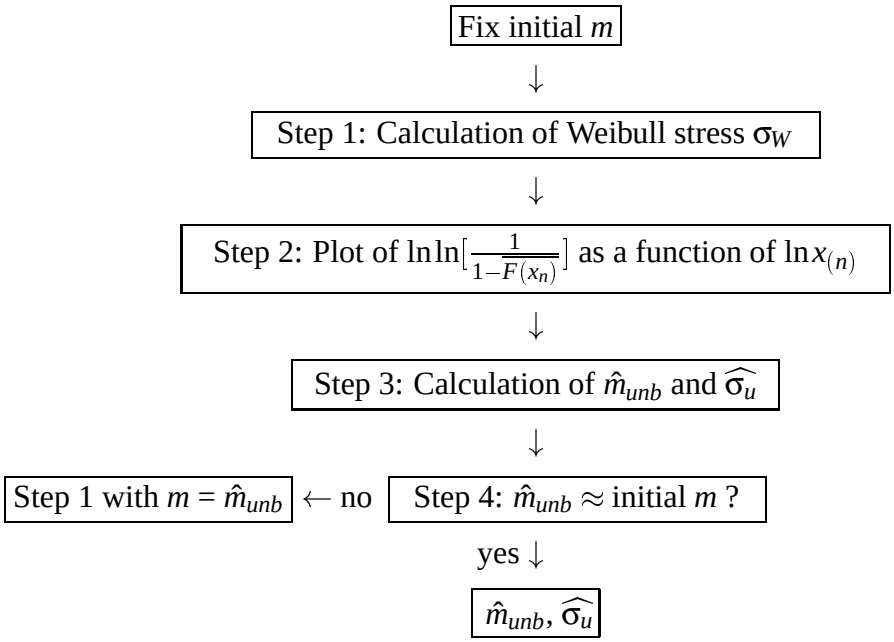

Figure 3.2: Flow diagram for iterative Weibull parameter estimation procedure

3. $l_1(N, \alpha_1)$ and $l_2(N, \alpha_2)$ is taken from Table B.7
   $C = \hat{m}/l_2$ and $D = \hat{m}/l_1$ are calculated.
   $[C, D]$ is reported to be the confidence interval for m for a confidence level of $1 - \alpha$.

These quantities have to be calculated with the maximum likelihood estimate of m without the unbiasing factors, $\hat{m}$, and not from $\hat{m}_{unb}$.

Note: The confidence intervals for m and σ_u are valid **only, if** $\hat{m}$ and $\widehat{\sigma_u}$ were obtained by the **maximum likelihood method**. Any other estimation procedure for the Weibull parameters yields different confidence intervals.

The Tables B.5 - B.7 were taken from Ref. [71]. [2]

Upon completion of the analysis, a plotfile is generated. It contains the values of the Weibull stress as well as pre-processed data in a form that allows immediate generation of a Weibull plot via some plotting programs like e.g. `gnuplot`. Figures A.42 and A.43 are generated in this way. The calculated values for $\ln\sigma_W$ are plotted together with the Weibull distribution which is a line with the slope $\hat{m}$ and containing the point $(\widehat{\sigma_u}, 0)$.

3.3.3 Improved confidence intervals from bootstrap procedures

It should be emphasized that the evaluation of the distribution parameters of σ_W, namely m and σ_u, is based on statistical inference methods that are applied without fully meeting the conditions of their applicability. It is not clear beforehand whether the maximum likelihood parameter estimation gives valid results for the present case, where the random variate depends on the distribution parameter itself and an iterative procedure is used to obtain consistent results.

[2] An EXCEL template for the evaluation of the Weibull parameters is available upon request from the first author: riesch-oppermann@imf.fzk.de.

There are no methods available to quantify the statistical properties of the estimators of the Weibull parameters.

For these reasons, the confidence intervals based on the results found by Thoman et al. [71] and used in the ESIS P6 procedure [21] may only approximately reflect the statistical uncertainty of the parameter estimates. This situation is completely different from the Weibull parameter estimation in the strength measurement for ceramics, where no iterative procedure is required.

There are novel statistical techniques capable to reflect the complex behaviour of random variates because they are not based on parametric models: so-called bootstrap or resampling methods can be used to generate confidence intervals by simulation [20]. The parent distribution used for the simulation is the empirical distribution of the available experimental sample. The essential advantage over classical statistical inference methods is the fact that these methods use empirical distributions of statistical estimates for the generation of confidence intervals. Thus, there is no need to know the closed-form solution for the distribution of the statistical estimate as is the case in the classical methods. From a statistical point of view, this is equivalent to the use of non-parametric maximum-likelihood estimators instead of parametric maximum-likelihood estimators, for which the usual confidence intervals are generated [14].

Resampling methods are well-known in the field of medicine and biology, but only begin to enter in materials science [24], though there is some effort to base coding schemes on resampling ideas [12].

In Chapter 4, results for parameter correlation and confidence intervals are given and compared with standard Maximum Likelihood results.

3.4 Local risk of rupture prediction

Using weakest link arguments, it is possible to obtain the probability that fracture is initiating from a micro-crack at a specific location in the specimen with arguments similar to those used in [82]. Two events must be present: (A) a micro-crack must be present at this location and, (B), the stress must be sufficiently high to cause unstable propagation of the micro-crack.

3.4.1 Basic relations

In statistical terms, we obtain the local risk of rupture as conditional probability of having a micro-crack in some sub-volume, V_s, of the specimen under the condition that this micro-crack causes unstable fracture. If A denotes the event that a micro-crack is located within a certain sub-volume, V_s, the probability $P(A)$ is given by

$$P(A) = \frac{V_s}{V_{pl}} \tag{3.18}$$

for a material with homogeneously distributed micro-cracks within the plastic zone V_{pl}. The probability $P(B)$ that a given micro-crack causes failure is identical with Q_1 given in Eqn. (3.10):

$$P(B) = Q_1 = \tilde{C} \int_{V_{pl}} \sigma_1^m \, \mathrm{d}V \tag{3.19}$$

The proportionality factor, $\tilde{C}$, contains material characteristics of micro-crack fracture resistance as given in Eqn. (3.10). The conditional probability $P(A|B)$, i.e. the probability that a certain micro-crack that causes fracture is located within sub-volume V_s, is obtained using Bayes' theorem by

$$\begin{aligned} P(A|B) &= \frac{P(A \cap B)}{P(B)} \qquad \text{(Bayes}' \text{ theorem) with} \\ P(A \cap B) &= \tilde{C} \int_{V_s} \sigma_1^m \, \mathrm{d}V \end{aligned} \tag{3.20}$$

$P(A \cap B)$ is obtained according to Eqn. (3.20) by integrating $P(B)$ over V_s only (instead of V_{pl}) so that finally $P(A|B)$ is obtained as:

$$P(A|B) = \frac{\tilde{C} \int_{V_s} \sigma_1^m \, \mathrm{d}V}{\tilde{C} \int_{V_{pl}} \sigma_1^m \, \mathrm{d}V} = \frac{\int_{V_s} \sigma_1^m \, \mathrm{d}V}{V_0 \, \sigma_W^m} \tag{3.21}$$

Eqn. (3.21) shows that $P(A|B)$ depends only on the scatter of the Weibull stress σ_W, which is characterized by the Weibull modulus, m, but not on its characteristic value, σ_u. This is expressed by the fact that $\tilde{C}$ can be cancelled in Eqn. (3.21).

For infinitesimal V_s, we obtain from the integrand of Eqn. (3.21) a (conditional) probability density $\pi_i(\vec{x}|\sigma_W(i))$ of the local risk of rupture at location $\vec{x}$ which is given by:

$$\pi_i(\vec{x}|\sigma_W(i)) = \frac{\sigma_1^m(\vec{x}, i)}{V_0 \, \sigma_W^m(i)} \tag{3.22}$$

$\pi_i(\vec{x}|\sigma_W(i))$ characterizes a certain load level i, so that only the fracture origin distribution at this particular load level is obtained. Experimentally, however, the observed fracture origins correspond to different load levels. In the experiment, we observe the (unconditioned) probability density $\pi(\vec{x})$, which can be obtained by integrating $\pi_i(\vec{x}|\sigma_W(i))$ over the whole range of σ_W. The integrated local risk of rupture density $\pi(\vec{x})$ is then obtained as:

$$\pi(\vec{x}) = \int_0^\infty \pi_i(\vec{x}|\sigma_W) \, f_{\sigma_W}(\sigma_W) \, \mathrm{d}\sigma_W \tag{3.23}$$

where $f_{\sigma_W}(\sigma_W)$ denotes the probability density of the Weibull stress σ_W. Eqn. (3.23) can be solved by numerical integration over a suitable load level range covering the experimental values of σ_W.

$$\pi(\vec{x}) \approx \sum_{i=0}^{n} \pi_i(\vec{x}|\sigma_W(i)) \, [\sigma_W(i) - \sigma_W(i-1)] \tag{3.24}$$

with $\sigma_W(0),\ \ldots,\ \sigma_W(n)$ chosen appropriately.

Appropriate choice of the range $\sigma_W(0),\ldots,\sigma_W(n)$ and the necessary refinement of loading range intervals $\Delta\sigma_W(i)$ can be checked by the fact that $\pi(\vec{x})$ is a probability density so that integration over the total volume of the specimen should give a value of unity:

$$\int_V \pi(\vec{x})\,\mathrm{d}V = 1. \tag{3.25}$$

3.4.2 Results for notched specimens

Figures A.31 and A.32 show the integrated local risk of rupture for the 1mm and 2mm notched specimens tested at -150° C.

In case of the 2mm notched specimens, the fracture origins tend to be located near the specimen axis. For the 1mm notched specimens, the fracture origin locations are predicted to lie in the middle region between specimen axis and notch root.

These results agree with the fracture origin distributions from the corresponding experiments, which are shown in Figure A.33 [76].

It is essential to integrate the local risk of rupture over the whole range of Weibull stresses because otherwise only results for specific loadcases would be obtained. A typical example is shown in Figures A.29 and A.30, where the local risk of rupture density for small and large Weibull stress values are showed. With increasing loading, the region of maximum density values for the local risk of rupture is shifted towards the specimen axis.

3.4.3 Results for pre-cracked specimens

For pre-cracked specimens, preliminary calculations lead to a predicted local risk of rupture which is confined to a small region ($\leq 40\mu$m) close to the crack tip. Interpretation of this result has to be done with some caution, because no effects of stress redistribution due to ductile void formation were taken into account. Figure A.49 shows the contours of the local risk of rupture density at a load level corresponding to the highest fracture strain for deeply notched pre-cracked specimens (see also Chapter 6).

4

Statistical inference by bootstrap simulation

This chapter contains results obtained with the help of some novel statistical techniques, known as bootstrap or resampling techniques as well as some background needed for basic understanding of the methodology. Bootstrap methods (also known by the more descriptive name resampling methods) have been well-known since about 20 years in the field of biological and medical research [20] both because of the large economic impact of statistically-based decisions and because of the lack of analytical solutions for sophisticated statistical models, but they are relatively unknown in materials science. The methods rely heavily on the availability of sufficient computing power, which is the main reason for their coming up only recently.

Their essential advantage is that analytical solutions are replaced by suitably designed statistical simulations. Parametric as well as non-parametric stochastic models can be used which makes it possible to adapt modelling to the available knowledge. Especially for the case of small sample sizes, where statistical inference methods based on large sample approximations fail, use of bootstrap methods leads to significantly enhanced power of statistical inference results.

4.1 Background and procedure

Traditional methods of statistical inference are based on the fact that estimates of parameters calculated from random samples are themselves random variates (also known as statistics). Often, they have known statistical distributions, at least under certain conditions with respect to the sample value distribution and/or the sample size. As an example, the mean of a sample of independent identically distributed variables is known to follow a normal distribution for large sample sizes, the variance of a random sample of known mean value is χ^2-distributed. If closed-form distributions cannot be obtained, it is sometimes possible to obtain special-case solutions and to derive general solutions by an appropriate transformation of the variables. This is for instance done in [71] for the distribution of the maximum likelihood estimates $\hat{m}$ and $\widehat{\sigma_u}$ which can be obtained from the special case of a Weibull distribution with $m = \sigma_u = 1$, i.e. a standard exponential distribution.

From the known statistical distributions, confidence intervals are obtained easily by using quantiles of the respective distributions.

In the present case, however, where the Weibull stress σ_W is the random variable under consideration, the situation becomes somewhat difficult. From the definition of σ_W (see Eq. (3.12)), it follows that σ_W itself contains the (originally unknown) distribution parameter m. This, in principle, violates the conditions of applicability of conventional methods of statistical inference. The results obtained for estimates and confidence intervals are therefore only approximate.

4.1.1 Basic idea of bootstrapping

One way of dealing with the lack of closed-form expressions for statistical quantities is to use Monte Carlo methods. Bootstrapping is one of them. In the following, a *very* concise description of the bootstrap method mainly based on [20] is given. (We use the traditional nomenclature, hats ($\hat{.}$) denote estimates, asterisks ($.^*$) denote quantities related to bootstrap samples, n is the sample size, B is the number of bootstrap simulations.)

Suppose we observe $x_1, \ldots, x_n$ independent data points, from which we compute a statistic of interest $s(x_1, \ldots, x_n)$.

A *bootstrap sample* $x^* = (x_1^*, \ldots, x_n^*)$ is obtained by randomly sampling, n times, with replacement, from the original data points $x_1, \ldots, x_n$. If this is repeated B times, we can generate a large number of independent bootstrap samples $x^{*1}, \ldots, x^{*B}$, each of size n.

Corresponding to each bootstrap sample x^{*b} there is a bootstrap replication of s, namely $s(x^{*b})$, the value of the statistic of interest computed for sample x^{*b}.

Besides $s(x^{*b})$, we also obtain a bootstrap estimate for its standard deviation, namely

$$\widehat{\mathrm{se}}_{\mathrm{boot}} = \sqrt{\frac{1}{B-1}\sum_{b=1}^{B}\left[s(x^{*b}) - s(.)\right]^2} \tag{4.1}$$

where $s(.) = \sum_{b=1}^{B} s(x^{*b})/B$ is the mean value of the statistic s after B bootstrap simulations.

4.1.2 Bootstrap confidence intervals

Using $\widehat{\mathrm{se}}_{\mathrm{boot}}$ and $s(.)$, it is possible to attribute confidence intervals to bootstrap estimates $\hat{\theta}^*(.) = \sum_{b=1}^{B} \hat{\theta}^*(b)/B$, where $\hat{\theta}^*(b) = s(x^{*b})$ is the bootstrap replication of $\hat{\theta} = s(x_1, \ldots, x_n)$ as defined above. For example, we obtain the usual standard normal $(1-2\alpha)$-confidence interval for θ, which is

$$\hat{\theta} \pm z^{(\alpha)} \times \widehat{\mathrm{se}} \tag{4.2}$$

where $z^{(\alpha)}$ is the α-quantile of a standard normal distribution, e.g. $z^{(0.95)} = 1.645$ for the 90% confidence intervals. This leads to the so-called *standard bootstrap confidence intervals* which still rely on normal theory assumptions as can be seen from Eq. (4.2), which only holds exactly if $\hat{\theta}$ follows a normal distribution.

But it is also possible to obtain accurate confidence intervals for non-normally distributed statistics, i.e. without relying on normal theory assumptions. This is done by using $\hat{G}$, the cumulative distribution of the bootstrap replications $\hat{\theta}^*$. The $1-2\alpha$ *percentile interval* for θ is defined by

the α- and $(1-\alpha)$-quantiles of $\hat{G}$. From B independent bootstrap samples, we obtain the percentile confidence intervals by taking the $B \times \alpha$-th value in the ordered list of the B bootstrap replications of $\hat{\theta}^*$ as the lower limit and the $B \times (1-\alpha)$th value of the list as the upper limit of the confidence interval. These empirical percentiles are denoted $\hat{\theta}_B^{*(\alpha)}$ and $\hat{\theta}_B^{*(1-\alpha)}$ respectively and the percentile confidence interval reads

$$[\hat{\theta}_B^{*(\alpha)},\ \hat{\theta}_B^{*(1-\alpha)}] \tag{4.3}$$

for a confidence level of $1-2\alpha$.

Some drawbacks of the percentile intervals with respect to coverage probabilities are handled by an improved version of the percentile method including bias correction in the bootstrap replications. Bias correction z_0 is obtained from the cumulative distribution function $\hat{G}$ of the bootstrap replication and the original estimate $\hat{\theta}$ of the original sample via

$$z_0 = \Phi^{-1}(\hat{G}(\hat{\theta})) \tag{4.4}$$

where $\Phi^{-1}(.)$ is the inverse standard normal cumulative distribution function (CDF). We obtain the bias-corrected bootstrap confidence intervals as

$$\left[\hat{G}^{-1}\left(\Phi(2z_0+\Phi^{-1}(\alpha))\right),\ \hat{G}^{-1}\left(\Phi(2z_0+\Phi^{-1}(1-\alpha))\right)\right] \tag{4.5}$$

with z_0 from Eq. (4.4). Confidence intervals according to Eq. (4.5) are used throughout the presentation of the bootstrap results in the following section. Calculation of z_0 is indicated in some of the Figures, e.g. A.36, A.37, A.39, A.38. $z_0 = 0$ indicates no bias correction. In that case, the lower limits of the confidence intervals would coincide with the empirical CDF shown, as nearly is the case in Figure A.39. $z_0 \neq 0$ leads to a shift of the confidence intervals.

Further improvements of confidence levels can be obtained by application of still more advanced methods like the BC_a-method or the ABC-method suggested in the statistical literature [20]. These methods have not yet been implemented and therefore are not used in the sequel.

4.2 Results

The general ideas presented in the previous section are now applied to obtain confidence intervals in the specific case of the Weibull parameter estimation of the Weibull stress.

4.2.1 Weibull stress bootstrapping procedure

In the present case, where we are interested in statistical inference about the distribution parameters m and σ_u of σ_W, the basic situation is as follows: the original sample consists of the n values of ΔD at fracture or - equivalently - of the n maximum principal stress envelopes at fracture, from which the σ_W-values are computed. In this case, the statistic under consideration is not available as an analytical expression, but only numerically as a result of an iteration algorithm. When doing bootstrap simulations, this does not cause any problem. The procedure

is explained for the parameter m for the sake of simplicity; more accurately, we should use $(m,\ \sigma_u)$ as a two-dimensional statistic.

From the original sample, we obtain the original estimate $\hat{\theta} = \hat{m}$ using the iterative maximum likelihood procedure together with the usual maximum likelihood confidence intervals.

Bootstrapping is now performed by randomly sampling, n times, with replacement, from the sample of the ΔD at fracture, from which n values, $\sigma^*_{W_{(1)}}, \ldots, \sigma^*_{W_{(n)}}$, are computed. This is repeated B times, thus giving B samples σ^{*b}_W. For each bootstrap sample, a value of $\hat{m}^*(b)$ is obtained by the iterative maximum likelihood procedure.

After completion of the bootstrap simulations, the bootstrap confidence intervals are generated according to Eq. (4.5) for confidence levels $(1-2\alpha)$ corresponding to $\alpha = 0.02; 0.05; 0.10$ in agreement with the maximum likelihood confidence intervals available from literature [21, 71].

4.2.2 Bootstrap results for parameter estimation

The pairs of corresponding outcomes for the parameters of the Weibull stress distribution, $(\hat{m}^*(b),\ \hat{\sigma_u}^*(b)),\ b = 1, \ldots,\ B$ are directly available from the bootstrap simulation. m and σ_u appear to be strongly correlated as can be seen from Figure A.34 for the 1mmm notched specimens tested at 150° C.

Incidentally, this remarkably strong dependency of the two parameters does not occur in the case of a Weibull parameter estimation for strength measurements in ceramics, where also weakest link mechanisms determine the fracture behaviour. Even if a strong R-curve behaviour suggests some deviation from the Weibull distribution assumptions, the correlation seems to be very small [57].

The pronounced correlation which is present in the Weibull stress results is a consequence of the fact that σ_W contains the Weibull modulus m (see Eqn. (3.12) on page 10).

4.2.3 Bootstrap results for confidence intervals

Figure A.36 shows the bootstrap results for m in terms of the empirical CDF $\hat{G}$ for the 1mm notched specimens tested at -150° C. Bootstrap confidence intervals for confidence levels are indicated by horizontal lines at the appropriate CDF levels of 2, 5, and 10%, respectively, corresponding to 96%-, 90%-, and 80%- confidence intervals. From the value of the bias correction variable $z_0 = -0.29$, it can be seen that there is a considerable bias in the bootstrap estimate towards higher values. The confidence interval limits are therefore shifted towards lower m-values, as can be seen in Figure A.36 (see also Table B.4 for the numerical results).

For the 2mm notched specimens tested at -150° C, results for m in terms of the empirical CDF $\hat{G}$ are shown in Figure A.37. The bias correction variable z_0 amounts to $z_0 = -0.20$. The shape of $\hat{G}(m)$ indicates that there is a considerable fraction of quite large values of m in the simulation.

The empirical CDF $\hat{G}$ of the parameter $\hat{\sigma_u}$ for the 2mm notched specimens, which is shown in Figure A.39 shows a quite strange behaviour, if compared to corresponding results for the 1mm notched specimens in Figure A.38. A pronounced plateau around $\sigma_u \approx 2000$MPa indicated a gap in the simulation results around this value.

Examination of the corresponding $(\hat{m}, \hat{\sigma_u})$-points shows a clustering of the bootstrap simulation results (see Figure A.35). Clustering does not occur for the r=1mm notched specimens (results in Figure A.34). Figures A.35 and A.34 contain also the 90% confidence intervals for $\hat{m}$ and $\hat{\sigma_u}$, respectively, based on the maximum likelihood method. It is obvious, that the confidence intervals give a poor reflection of the uncertainty in the two parameters, $\hat{m}$ and $\hat{\sigma_u}$, so that their use is of limited value for a transferability analysis of results for different specimen geometries.

Here, an additional feature of the bootstrap method has a useful application: the assessment of confidence intervals for the complete CDF.

4.2.4 Bootstrap intervals for probabilities

Bootstrapping does not only allow conclusions to be drawn with regard to parameters, but also inferences to be made regarding the entire CDF. This is not possible using ML confidence intervals.

Figure A.40 contains results of the empirical CDF of the Weibull stress σ_W as outcome of the bootstrap simulation procedure together with the respective 0.05- and 0.95- confidence limits. The procedure to obtain these confidence limits is as follows:

During bootstrap simulations, a number of, say, B bootstrap samples is generated. From all of the B bootstrap samples, we obtain B values corresponding to the quantiles of interest, e.g. 0.05- or 0.95-quantiles for each of the n probability levels corresponding to the original sample.

For each probability level, i/n, corresponding to the i-th value of an ordered sample of size n, a 90% confidence interval is so obtained. Figure A.40 contains two empirical CDFs, namely for 1mm- and 2mm- notched specimens tested at -150° C. Each of the two CDFs is enclosed in a band formed by the limits of the 0.05- and 0.95-quantiles at the corresponding probability level.

The 90% confidence bands do overlap for all Weibull stress values. The empirical CDF of the 1mm notched specimens is completely contained in the quite wide 90% confidence band of the 2mm notched specimens. Conversely, the empirical CDF of the 2mm notched specimens is contained in the (smaller) 90% confidence band of the 1mm notched specimens only in the upper regime of Weibull stress values. Figure A.40 indicates that both samples of Weibull stresses are compatible.

Increasing the bootstrap sample size from $B = 200$ to $B = 1000$ does not change the width of the confidence intervals significantly. Results are shown in Figure A.41 for the 2mm notched specimens. This confirms that stable results even for confindence bounds are usually obtained with a quite small number of simulations.

It should be emphasized that statistical inference based on bootstrap confidence intervals does not rely on underlying assumptions about probability models and therefore is not restricted in applicability like e.g. inference procedures based on the ML approach.

5

Material characterization and design of RNB specimens

5.1 Material characterization

The ferritic-martensitic chromium steel with designation F82H-mod was produced by NKK-corporation (Japan). The material was vacuum-induction-melted and rolled plates of 7.5 as well as 15 mm thickness were available for specimen fabrication. The plates were consecutively numbered and submitted to a heat treatment procedure which was performed by the manufacturer.

5.1.1 Chemical composition and microstructure

The chemical composition is given in table B.1. The material is available in a reference heat treatment condition of 1040°C/38min + 750°C/60min with a DBTT observed in Charpy V tests of about -70 to -50°C [59]. In the reference condition, the material has fully martensitic structure and is free of δ-ferrite. The average grain size is about 70μm with no significant difference in LT, LS and TS orientation.

Due to the low carbon content, lath martensite is present with laths of about 2 μm thickness. Laths are oriented along $<111>$-direction within the former austenite grains. The laths as well as the former austenite grain boundaries are decorated with $(Fe,Cr,W)_{23}C_6$ precipitates. These $M_{23}C_6$ special carbides are homogeneously distributed. Their average size is about 0.20 μm and the volume fraction is about 1.9%.

Additionally, oxide particles in the form of $(Ti,Ta)_{(1-x)}O_x - Al_2O_3$ are present in the material with an average size of 5.7 μm and a volume fraction of about 0.057%. Fig. A.1 shows a SEM image of a metallographic section in the reference condition.

5.1.2 Elasto-plastic deformation behaviour

A detailed knowledge of the stress-strain relation up to fracture of the material is required for the calculation of the Weibull stress at fracture at various temperature levels. Tensile tests with smooth cylindrical bars were conducted at -150° C, -75° C and ambient temperature. Young's

modulus E and true stress-strain curves were obtained from load F vs. extensometer longitudinal displacement l measurements (see Fig. A.15) up to necking of the specimens. True stresses σ and ε were calculated from engineering stresses $s = F/A_0$ and strains $e = \Delta l/l_0$ according to the relations:

$$\varepsilon = \ln(1+e) \qquad \text{and} \qquad \sigma = s(1+e). \tag{5.1}$$

Eqns. (5.1) are based on the presence of a homogeneous strain distribution along the gage length and a constant volume relationship and thus are valid only to the onset of necking of the specimen [16]. An elastic-plastic material law with a hardening exponent of $n = 0.07$ and temperature dependent parameter K was fitted to the true plastic strain range of $[.1, \ldots, 10\%]$ according to the so-called Ludwik [41] or Hollomon relation

$$\sigma = K\varepsilon_{\mathrm{pl}}^{n}. \tag{5.2}$$

A summary of the parameters that were used for the subsequent analysis of the RNB specimens is given in Table B.2.

Figure A.14 shows the obtained stress-strain curves for -150° C, -75° C, and ambient temperature up to necking together with the Ludwik approximation that was used to extrapolate beyond the range of extensometer recordings.

Beyond necking (i.e. for strains exceeding about 7-13%, see Fig. A.16), the calculated stresses and strains from load-displacement recordings become invalid, for reasons mentioned above. For a detailed analysis of the uniaxial stress-strain behaviour after necking, stress corrections using the shape of the developing neck [7] would be necessary because of the multiaxial stress state after necking and the corresponding increase of the yield stress compared to uniaxial loading.

Fig. A.16 shows that the power-law fit is relatively poor at low strains, especially in cases, where a slight yielding plateau can be observed. However, a parametric description of the stress-strain law is useful if systematic investigations on material behaviour are envisaged [17]. In the following, mainly the parametric description of the stress-strain law is used. Due to difficulties in the numerical stability, piecewise linear approximation of the stress-strain law is preferred if large fracture strains are to be modelled.

5.2 Design of axisymmetrically notched (RNB) specimens

The results of the elasto-plastic characterization were used to select suitable notch geometries. In order to avoid effects from notch root finishing and to ensure that fracture is initiating from locations well inside the material, the final geometries were selected in a way that the axial stress in the plane perpendicular to the notch root attains its maximum inside the specimen. Also the course of the axial and circumferential stresses as well as the degree of multiaxiality in that plane should vary significantly for the various geometries.

5.2.1 Finite Element analysis of RNB specimens

Large strain deformation plasticity calculations with the ABAQUS Finite Element code [1] with a Ramberg-Osgood material law equivalent to Eqn. (5.2) were performed. Eight-node axisymmetric elements with reduced integration were used for the analysis. A basic geometry of cylindrical notched bar specimens with 10mm diameter, notch depth 2.5mm was selected. From the results of the Finite Element Analysis, notch radii of 1, 2, and 5mm were chosen. An example of the obtained stress distributions for the 1mm notched specimen at the three different temperature levels is shown in Fig. A.17 together with the used finite element mesh. Figures A.18 and A.19 show the results for the 2mm and 5mm notched specimens, respectively. The stress curves show the axial stresses along a line from the notch root to the specimen centre. Results for the multiaxiality h, which is defined as

$$h = \frac{\sigma_{kk}}{3\sigma_{eq}} \tag{5.3}$$

are shown in Figures A.20, A.21 and A.22, respectively, each Figure containing results for the three different temperature levels of -150° C, -75° C, and ambient temperature. Figures A.23, A.24 and A.25 show corresponding results for the von Mises stress distribution, Figures A.26, A.27 and A.28 contain the equivalent plastic strains along the line from the notch root to the specimen centre.

6

Cleavage fracture results

Chapter 6 contains experimental results for Weibull stress parameters obtained from on axisymmetrically notched specimens. Additionally, axisymmetrically pre-cracked specimen results are given. For both cases, Weibull stress results and results of the accompanying fractographic investigations are compared.

6.1 Tensile tests on axisymmetrically notched bars

Following the results of the Finite Element stress and multiaxiality results, axisymmetrically notched bar specimens with a raw diameter of 10mm and a minimum diameter of $d_0 = 5$mm were fabricated from plates of 15mm thickness. The orientation of the specimen axis was perpendicular to the main rolling direction. Notches of 1, 2, and 5mm radius were introduced and surface finish of the notches was achieved by polishing in axial direction. All specimens were measured and the initial notch diameter compared to the nominal values.

The tests were performed on a Instron 50kN servohydraulic tensile testing machine under displacement control with a crosshead speed of .5mm/min and continuous recording of load F and minimum notch diameter d. Continuous recording of the minimum notch diameter d was performed using an optical data acquisition system described in Ref. [77].

A brief description of the experimentally determined quantities at fracture as well as the respective fractographic results is given in this section.

6.1.1 Deformation and fracture

For the numerical evaluation of the tests, the load (F) vs. reduction of diameter (Δd) curve is required. For a temperature level of -150° C, Figure A.4 shows the calculated curves together with the values of the specimens at fracture. For the sharp (1 mm) notched specimens, the fracture occurred before maximum load within a relatively small Δd- range, whereas for the 2 mm notched specimens a larger range of Δd at fracture was observed and some doubt on the homogeneity of the data is caused by one specimen fracturing at a considerable larger Δd than the rest. Fractographic investigations revealed that the fracture appearance was quite different from the rest of the sample (see below). This could be attributed to some irregularities in the specimen preloading before testing.

For the 5mm notched specimens, Δd at fracture attained considerable larger values and excessive plastic deformation occured. Surprisingly, the experimentally obtained values were still met with good accuracy by the calculated $F - \Delta d$-curve despite the fact that no ductile damage was contained in the constitutive Ramberg-Osgood model.

This behaviour is also reflected in the results of the observed mean stress $\sigma_M = 4F/(\pi d^2)$ and mean strain $\varepsilon_M = 2\ln d/d_0$ at fracture given in Figures A.5 and A.6. At -75° C, all of the 5mm notched specimens as well as some of the 2mm notched specimens exhibited pronounced drop in the mean stress value which is also associated with an audible crackling during the course of the test. This stress drop was taken as indicative for specimen failure and the corresponding stress and strain values at fracture are those shown in Figure A.6.

Fractographic results given below will provide an explanation of the observed fracture behaviour.

6.1.2 Fractography

All of the tested specimens were fractographically investigated. Low resolution SEM images were taken to show the overall fracture appearance and as basis for a subsequent location of fracture origin location identification. A quantitative analysis of the fracture origins was performed with respect to the kind of initiation sites, their size, and their location at the fracture surface. A sizing of the fracture initiating defect was performed for a subsequent calculation of local fracture toughness values.

Fracture appearance

Pure trans-granular cleavage fracture was observed for 1 and 2mm notched specimens at -150° C. A mixed trans- and intergranular fracture appearance with some amount of ductile damage was observed for the 5mm notched specimen at -150° C as well as for the 1mm notched specimens at -75° C. The 2 and 5mm notched specimens at -75° C showed a substantial amount of axial cracking, i.e. several micro-cracks are visible on the fracture surface with the micro-crack planes in direction of the specimen axis. At RT, ductile fracture occurred for all specimen geometries with populations of small and large voids corresponding to carbides and oxide inclusions, respectively.

Representative for the differences in the fracture behaviour, typical examples of fracture surfaces are shown in Figs. A.7 (pure trans-granular cleavage fracture, -150° C, 2mm), A.8 and A.9 (mixed trans- & inter-granular cleavage fracture, -75° C, 2mm and -150° C, 5mm), and A.13 (ductile fracture, RT, 1mm).

Fracture origin sites

Fracture origins were identified by following the river patterns in case of pure cleavage fracture. At -150° C, for the 1 and 2mm notched specimens, oxide inclusions could be identified at most of the fracture origin sites. The size of the inclusion was determined and a corresponding micro-crack was approximated by a penny-shaped crack geometry. Here, we assume that initiation and propagation of the micro-crack are uncoupled events. Initiation may occur in an early stage at comparatively low stress levels. Initiated cracks lead to spontaneous fracture if the local stress

exceeds some critical value. From the local stress at fracture and the micro-crack size, local fracture toughness values can be obtained. Results are described later.

For the 5mm notched specimens, no identification of inclusions etc. at fracture origin sites was possible. For two specimens, micro-cracks were identified at the respective sites.

At -75° C, mixed trans/inter-crystalline fracture was prevalent in all specimens. For the 1mm notched specimens, fracture originated from the vicinity of ductile islands on the fracture surface. For the 2 and 5mm notched specimens, axial cracking became even more pronounced with fracture surfaces showing two large axial cracks of T- or X-shape which join at the specimen centre (see Fig. A.10).

At ambient temperature, ductile fracture was observed for all specimen geometries (see Fig. A.13 for a 1mm notched specimen). Two different void populations were present. The large voids correspond to oxide particles whereas the small voids are generated by carbides.

Distribution of fracture origin locations

A quantitative statistical analysis of the fracture origin locations was performed in cases where fracture origin localization was possible.

For the -150° C specimens with 1mm notch radius, fracture origins were evenly distributed over a range from about 350 to 2100 μm measured from the specimen centre. A tendency was observed that, with increasing fracture strain, fracture origins were located at lower distances from the specimen centre.

For the -150° C specimens with 2mm notch radius, fracture origins were evenly distributed over a range from about 250 to 1000μm measured from the specimen centre. No correlation between the fracture origin locations and the fracture strains, which were larger than for the 1mm notched specimens, was observed.

For the -150° C specimens with 5mm notch radius, fracture origins were concentrated within a small region of 250-350μm measured from the specimen centre. The observed notch diameter reduction at fracture was considerable larger than for the 1 and 2mm notched specimens.

Fig. A.46 gives the fracture origin locations and the corresponding fracture strain characterized by the notch diameter reduction Δd.

For the -75° C specimens, fracture origins were located evenly distributed along a distance of 5-700μm from the specimen axis. For the 5mm notched specimens, no fracture origins could be localized.

Complementary analysis on axial cracking

Complementary investigations were performed to reveal the cause of axial cracks present in some of the broken specimens. Flat specimens were tested at ambient temperature and after fracture micrographs were taken from undeformed regions (Figure A.11) and from adjacent to the necking region of the specimen (Figure A.12). The different orientation of the carbide decorations indicating martensite laths is clearly visible. While the orientation of the martensite laths is uniformly distributed in Figure A.11, plastic deformation of the specimen causes alignment of the martensite laths in axial (i.e. loading) direction. Change in orientation is connected

with shear stresses acting on carbide decorated martensite laths so that finally cracks may be able to initiate. The origin of cracks as shown in Figures A.7, A.10 and A.9 is attributed to that kind of shear-controlled crack initiation mechanism.

6.1.3 Weibull stress results

Numerical analysis of the samples tested at -150° C and -75° C was performed according to the numerical scheme described in Chapter 3 and led to the results given in Table B.3. Here, maximum likelihood estimators $\hat{m}$ and $\hat{\sigma_u}$ are given together with the respective ML confidence bounds. Bias correction for $\hat{m}$ was applied according to Table B.5 to account for finite sample size.

Two groups of results can be identified. The first group is characterized by moderate values of $\hat{m}$, whereas in the second group, $\hat{m}$ attains high values of about 80-100. The first group corresponds to low temperature testing conditions and small notch radii (see Weibull plot in Figure A.42). The second group failed at considerable larger strains (see also Figures A.5 and A.6).

As mentioned above, larger fracture strains correspond to the presence of a mixed trans- and inter-granular fracture appearance. For the 2mm notched specimens tested at -150° C, one specimen failed at considerable larger strain than the rest of the sample and exhibited also a mixed trans- and intergranular fracture appearance contrary to the rest of the sample that failed by pure trans-crystalline cleavage. There was some evidence that experimental conditions may be responsible for the untypical fracture mode. An accidental preload was imposed to the specimen. On the other hand, in some cases cleavage fracture was observed well above the transition temperature [13]. A stress analysis showed that the related loading was well below the elastic limit so that there was no reason to exclude the specimen from the analysis.

Excluding the specimen from the sample would lead to a considerable change in the $\hat{m}$-value from 10.7 to 17.3 and to a change of σ_u from 2107 MPa to 1843 MPa. This shows the large influence of single results on the distribution parameters for small sample sizes. For the purpose of statistical inference, the full sample size was retained.

For future analyses, a complementary analysis has to be provided where the formation of cracks due to plastic deformation of the material is addressed.

6.2 Tensile tests on axisymmetrically pre-cracked specimens

Tensile tests on axisymmetrically pre-cracked (RCB) specimens were performed in order to confirm transferability of cleavage fracture parameters obtained at notched specimens to pre-cracked specimens. RCB specimens are favoured for a number of reasons such as easy numerical analysis and absence of edge effects in the stress field an have attracted special emphasis for small specimen testing purposes [15]. Transferability between cleavage fracture parameters obtained from notched and pre-cracked specimen tests is still an open issue and remains topic of investigation for different materials [49].

6.2.1 Geometry and pre-cracking procedure

The specimen geometry is based on the RNB basic geometry and is shown in Figure A.44. Pre-cracking was done under rotating bend loading with a setup as shown in Figure A.45. The initial prestressing load was adjusted by imposing a fixed deflection. After crack initiation, the load drops due to the increasing compliance of the system. At a final load value, the specimen is unloaded and dismounted.

For all of the specimens, a symmetric circular pre-crack could be obtained with negligible eccentricity.

A total of fifteen specimens was available for testing at -150° C. Additionally, one specimen was tested at -75° C and ambient temperature, respectively.

6.2.2 Testing and Weibull stress analysis

The specimens were tested under displacement controlled loading with a crosshead speed of 0.5mm/min. Load and longitudinal displacement were continuously recorded. An extensometer (gage length 25mm) was used for the recording of the displacements that later served as loading variable for the numerical analysis of the specimens.

The geometry of the FE mesh is shown in Figures A.47 and A.48. Initial blunting of the crack tip was introduced as proposed by McMeeking [42] with an initial blunting radius of about 1μm. The initial blunting radius should be smaller than the CTOD value at limit load of the specimen. According to McMeeking [42], the value of CTOD can be calculated from

$$CTOD = \frac{0.6K^2}{E\sigma_0}\left[\frac{2\sigma_0(1+\nu)(1+n)}{\sqrt{3}nE}\right]^n \tag{6.1}$$

where n is the strain hardening exponent, ν is the Poisson ratio and E is Young's modulus. σ_0 is the yield stress of the material.

For the F82Hmod at -150° C, using values of $E \approx 200$GPa, $n = 0.09$, $\sigma_0 \approx 800$MPa and $\nu = 0.3$, we obtain a CTOD-value of about 3μm at $K \approx 30\text{MPa}\sqrt{\text{m}}$. The initial blunting radius actually used was 1μm, so that we expect to obtain quite accurate results for the stress and strain fields.

It turned out, however, that the values if the initial diameters exhibited considerable variations from specimen to specimen, so that an analysis with one single Finite Element model was not feasible. Due to the high numerical effort (each specimen would require its own Finite Element model) the full analysis was postponed and only one representative specimen was analysed with respect to local risk of rupture prediction (see 3.4.3).

A full analysis of all tested specimens will be subject of future work, where prediction of cleavage fracture parameters between pre-cracked and notched specimen geometries has to be validated.

6.2.3 Fractography

All specimens tested at -75 and -150° C showed pure trans-crystalline cleavage fracture [76]. Identification of fracture origins was possible. Fracture origins were located in the vicinity

of the crack front at a distance of about 150-400 μm. Unlike for the notched specimens, no cleavage fracture facets were observed and oxide inclusions were found at only about 40% of the fracture origin sites.

At ambient temperature, trans-crystalline cleavage fracture after some amount of ductile crack propagation was observed. No numerical analysis was performed because material parameters for ductile damage were not available.

Using material parameters for -150° C, calculation of the local risk of rupture predictions showed a concentration to a small region ($\leq 40\mu$m) ahead of the crack tip. A typical result is shown in Figure A.49, where the contours of the local risk of rupture density $\pi_i(\vec{x}|\sigma_W(i))$ (Eqn. 3.22) are shown for a value of $\sigma_W(i) = 1378$MPa. This corresponds to the deeply notched RCB specimen fractured at the highest σ_W-level. It is remarkable that the corresponding Weibull stress of $\sigma_W(i) = 1378$MPa leads to a CDF value of $F_{\sigma_W}(\sigma_W) \approx 0.2$ which is fairly below unity. A fracture origin location prediction would therefore require an extended range of σ_W, say, $\sigma_W \approx 1800$MPa with $F_{\sigma_W}(1800) \approx 0.98$ for the integration according to Eqn. (3.23) or (3.24), respectively.

The numerical values of the local risk of rupture are calculated with parameters $m = 11.6$ and $\sigma_u = 1943$MPa obtained from the analysis of the 1mm notched RNB specimens tested at -150° C.

6.3 Evaluation of local fracture toughness values

Results of fractographic analyses together with numerical analyses of fracture stresses are used for the evaluation of local fracture toughness values. For this purpose, a sizing procedure for the fracture origin sites was established, which is sketched in Figure A.50. The cleavage origin surrounds an oxide inclusion. The size of the cleavage origin site was modelled as penny-shaped crack, from which a critical crack size a_c was obtained. Using the results of the stress analysis, a local fracture toughness k_c can be obtained via

$$k_c = 2\sigma_1\sqrt{\frac{a_c}{\pi}} \tag{6.2}$$

according to [70]. Eqn. (6.2) provides a rather simplified measure of toughness. It has to be kept in mind that it is based on linear elastic fracture mechanics considerations, while the material undergoes substantial plastic deformation before fracture occurs. Also the existence of a stress gradient along the crack is neglected, which seems of less importance in case of notched specimens but may become of concern for crack tip situations.

In principle, k_c should lead to similar results for notched and pre-cracked specimens, if the underlying fracture mechanics description of the fracture process is adequate. A quantitative analysis is difficult, however, because even if fracture origin initiation locations could be detected, identification and sizing of cleavage fracture origin sites was not always possible, so that the resulting sample sizes mostly were too small for statistical inference purposes.

Figure A.51 shows results obtained at the -150° C temperature level. The step curves show the empirical cumulative distribution of the k_c-values while the continuous curves are maximum likelihood fits to a Weibull distribution. There is an obvious discrepancy between the results obtained at notched and pre-cracked specimens. Scatter for notched specimens is considerable

smaller than for pre-cracked specimens while the average local fracture toughness values are larger for the pre-cracked specimens. Uncertainty in the results for pre-cracked specimens may partly be attributed to the fact that the stress distribution used for the calculation of the k_c-values did not account for residual stresses which might be present due to the pre-cracking procedure.

For the notched specimens tested at -75° C, scatter in k_c is considerable larger, but due to small sample sizes of the local fracture toughness values that were available, no statistical evaluation was performed.

7

Present limitations and future work

Despite the successful application of local approach methods for cleavage fracture modelling of structural steels, some questions remain to be solved. Main issues are 1) the transferability between results from notched specimens to crack tip situations and 2) the behaviour in the transition regime, where void nucleation and ductile damage leads to different fracture appearance. For crack tip situations, constraint influence is an important parameter. A method for constraint correction in cleavage fracture modelling is therefore addressed in this Chapter. Steep stress gradients that are present in crack tio situations may play a role in difficulties with transferability from notched to pre-cracked specimens. Steep stress gradients require refined analysis of critical stresses an lead thus to modifications of the weakest link model. The main consequences are described below.

In the transition regime, statistical modelling is not determined by pure weakest link arguments but has to be extended to cover presence of void formation. The basic arguments are summarized shortly.

A topic of future investigation will be the characterization of material behaviour under irradiation conditions, where also analysis of Charpy results (dynamic fracture) has to be provided.

7.1 Constraint correction in cleavage fracture modelling

Constraint influence is handled by so-called toughness scaling relations. Various approaches are possible (e.g. [11, 18, 66] and, more recently, [25]). The main idea behind these approaches is to take into account the variations in the stress fields due to limited size of specimens or cracks in a systematic way by establishing relations between J_c for infinite bodies (i.e. J_{Ic}) and measured J_c-values for low constraint specimens.

Constraint correction is inherent in the Weibull stress for fracture mechanics (pre-cracked) specimens (see e.g. [11]).

For a power-law hardening material

$$\frac{\varepsilon}{\varepsilon_0} = \frac{\sigma}{\sigma_0} + \alpha\left(\frac{\sigma}{\sigma_0}\right)^n \tag{7.1}$$

(σ_0 - reference stress, $\varepsilon_0 = \sigma_0/\varepsilon_0$, n - hardening exponent, α - strain offset at σ_0), the stress field in the vicinity of a mode I crack tip can be described by a three-term asymptotic expansion [81]

$$\frac{\sigma_{ij}}{\sigma_0} = A_0 \bar{r}^s \tilde{\sigma}_{ij}^{(0)}(\theta) - A \bar{r}^t \tilde{\sigma}_{ij}^{(1)}(\theta) + \frac{A^2}{A_0} \bar{r}^{2t-s} \tilde{\sigma}_{ij}^{(2)}(\theta) \tag{7.2}$$

with the dimensionless quantities

$$\begin{aligned} \bar{r} &= \frac{r}{J/\sigma_0}, \text{ where } J \text{ is the J-integral} \\ \tilde{\sigma}_{ij}^{(k)} &- n \text{ - dependent angular stress functions.} \end{aligned} \tag{7.3}$$

The coefficient A_0 is given by

$$A_0 = (\alpha \varepsilon_0 I_n)^{-1/(n+1)} \tag{7.4}$$

with I_n according to [35]. The exponent $s = -1/(n+1)$ is theoretically known [35, 53] and for the exponent t an eigenvalue problem has to be solved (e.g. [81]). The amplitude A is determined by curve fitting of eq. (7.2) to FE crack tip stress results. The three-term approximation of the stress field is used for the calculation of the Weibull stress σ_W (see eq. (3.12)). In case of small scale yielding, i.e. if the first term of eq. (7.2) yields a good approximation of the stress field, and for two-dimensional cracks with a constant J along the crack front, it can be shown [5, 44] that σ_W can be re-written as

$$\sigma_W^m = \frac{J_c^2}{\sigma_0^2} \frac{B}{V_0} \int_{U_{pl}} \sigma_1^m \, \mathrm{d}U \tag{7.5}$$

where B is the specimen thickness, J_c is the value of the J-integral at the onset of cleavage fracture and U_{pl} is the normalized plastic zone size of a specimen of unit thickness given in terms of $\bar{r} = r\sigma_0/J$.

Under small-scale yielding conditions, and in case of a constant J along the crack front, σ_W and J_{Ic} can thus be expressed in terms of each other by identifying corresponding values of the cumulative distribution function of both quantities. This leads to the relation (see e.g. [44])

$$1 - \exp\left(-\left(\frac{\sigma_W}{\sigma_u}\right)^m\right) = 1 - \exp\left(-\left(\frac{J_{\mathrm{Ic}}}{b}\right)^2\right) \tag{7.6}$$

where b is a distribution parameter of the J_{Ic} distribution, or, solved for σ_W:

$$\left(\frac{\sigma_W}{\sigma_u}\right)^m = \left(\frac{J_{\mathrm{Ic}}}{b}\right)^2 \qquad \text{or} \qquad J_{\mathrm{Ic}} = b\left(\frac{\sigma_W}{\sigma_u}\right)^{m/2} \tag{7.7}$$

If there is a significant loss of constraint, higher-order terms are needed for a description of the stress field. In this case, the Weibull stress is of the form

$$\left(\frac{\sigma_W}{\sigma_0}\right)^m = \frac{J_c^2}{\sigma_0^2} \frac{B}{V_0} G(A, M) \tag{7.8}$$

where M stands for the material parameters and the dimensionless function

$$G(A, M) = \int_{U_{pl}} \left(\frac{\sigma_1}{\sigma_0} \right)^m \mathrm{d}U \tag{7.9}$$

depends on the load level only and not explicitly on the crack size or specimen geometry. Thus, it is possible to select a reference solution for A, e.g. the small-scale yielding value, A_{SSY}. A_{SSY} can be obtained by a modified boundary layer solution for small-scale yielding for suitably selected values of the stress intensity factor K and the amplitude T resulting in prescribed elastic displacements at the boundary of the elasto-plastic boundary value problem. For a given value of σ_W, J_c can then be transformed into an equivalent small-scale yielding value, J_{SSY}, by

$$\left(\frac{J_c}{J_{\mathrm{SSY}}} \right)^2 = \frac{G(A_{\mathrm{SSY}}, M)}{G(A, M)} \tag{7.10}$$

which, as $\sigma_W \propto J^{2/m}$ holds for SSY, implies that the failure probability can be written in terms of a Weibull distribution for the transformed values of J_{SSY} with a shape factor of $m = 2$.

For a given amplitude A, is is thus possible to predict J_{Ic} from the σ_W results using the following two-step procedure:

1. Compute σ_W at fracture from the J_c results according to eq. (7.8).
2. Calculate J_{Ic} from experimentally obtained J_c values according to eq. (7.10) and determine the parameter b of the J_{Ic} distribution (which is a Weibull distribution with $m = 2$)

This procedure additionally allows the scatter bands in the data to be determined by using the appropriate relations for the respective quantiles of σ_W and J_{Ic}.

Analysis of literature data in Ref. [11], where J_c/J_{Ic} was predicted for typical fracture mechanics specimens (ECP, CCP, 3PB, CT) showed promising results. Good agreement was found for the following function

$$G(A, M) = \exp\left(a_0(M) + a_1(M)A + a_2(M)A^2 \right) \tag{7.11}$$

with the material-dependent parameters a_i.

The essential advantage of this scaling approach is the fact that there is no explicit dependence of crack size or specimen geometry. Thus, the stress field is characterized by the (elastic) boundary conditions (J and T) of an elasto-plastic (modified) boundary layer (MBL) problem, from which the scaling function $G(A, M)$ is deduced, and FE analysis of the specimen is replaced by use of appropriate stress amplitudes in the MBL approach.

In the field of nuclear fusion energy applications, this scaling approach seems to be especially promising for the processing of data from small (sub-sized) specimen testing results, provided that the influence of material heterogeneity on this scale still allows the use of a continuum mechanics approach.

Dodds et al. [18, 66] use the concept of equivalent stressed volumes ahead of the crack front for the correction of toughness values in the lower transition regime obtained by testing SENB specimens with different a/W ratios. A significant reduction in the scatter of the results is obtained, also the corrected J_c-values for different a/W ratios agree very well.

A somewhat different approach based on a process zone crack instability model is used in [47].

7.2 Modifications in case of steep stress gradients

If steep stress gradients exist, which means that the assumption of a constant stress along the existing cleavage origins is violated, the weakest link argument leading to the Weibull distribution of σ_W still holds. However, the fracture mechanics description of the cleavage origins as micro-cracks with a critical crack size $a_c \propto 1/\sigma_c^2$ (or, equivalently: $K \propto \sqrt{a}$) is no longer valid. Instead, a_c depends not only on the magnitude of the local stress field, but additionally on the stress gradient, or, equivalently, on the location of the crack. As a consequence, m loses its significance as material parameter [10, 23] and becomes dependant on the relation between stress intensity factor K and crack length a (which depends on the type of loading). Steep stress gradients may be relevant at very low temperatures due to very small plastic zone sizes as well as for thermal loading. In these cases, weight function methods are necessary [22] and the evaluation of the stress integral requires the use of location-dependent critical stresses which may be obtained e.g. by neural network approaches [68].

7.3 Transition behaviour and the influence of ductile damage

In the transition regime, a competitive process between ductile and cleavage fracture mechanisms takes place [52]. Void nucleation and growth change the stress and strain field and final cleavage fracture can only occur, if the stresses remain sufficiently high to trigger unstable crack propagation. So, for a volume element dV, the two competitive processes can be stated as follows: Cleavage occurs, if a critical cleavage stress is exceeded in dV, while ductile failure by void coalescence occurs, if a critical void volume fraction $f_0^c(\varepsilon_{\mathrm{eq}}^p)$ (depending on the equivalent plastic strain $\varepsilon_{\mathrm{eq}}^p$) is exceeded in d$V$.

The modelling of this competitive process must consider the respective probabilities (see e.g. [78, 79, 80]). In case of ductile and cleavage fracture being independent of each other, the respective survival probabilities multiply and give the overall survival probability for combined fracture [39, 51, 52]. This means, that Eqns. (3.3) and (3.4) have to be modified and now read:

$$Q_1^{duc} = \frac{1}{V_{nuc}} \int_{V_{nuc}} 1 - F_{f_0}(f_0^c(\varepsilon_{eq}^p, \vec{r}))\,\mathrm{d}V \tag{7.12}$$

and

$$R_k^{duc} = (1 - Q_1^{duc})^k \tag{7.13}$$

where Q_1^{duc} is the failure probability of one ductile fracture initiation site and R_k^{duc} is the corresponding survival probability if k ductile fracture initiation sites are present. The void nucleation volume V_{nuc} is determined by a critical nucleation stress. The probability distribution F_{f_0} of the initial void volume fraction, f_0, has to be obtained by image analysis. In [52], a lognormal probability distribution was used.

A weakest link argument for ductile fracture leads to the following form of the failure probability P_f^{duc}:

$$P_f^{duc} = 1 - \sum_{k=0}^{\infty} p_k R_k^{duc} \tag{7.14}$$

where $p_k = \frac{(M_d V_{nuc})^k}{k!} \exp(-M_d V_{nuc})$ is the Poisson density and M_d is the mean number of void initiation sites per unit volume. Summing up the terms of Eqn. (7.14) we end up with

$$\begin{aligned} P_f^{duc} &= 1 - \exp(-M_d V_{nuc} Q_1^{duc}) \\ &= 1 - \exp(-M_d \int_{V_{nuc}} 1 - F_{f_0}(f_0^c(\varepsilon_{eq}^p, \vec{r}))\,\mathrm{d}V \end{aligned} \tag{7.15}$$

which is similar to Eqn. (3.8) and has to be solved via a Finite Element post-processing routine.

For the modelling of the ductile-to-brittle transition, competition between ductile and cleavage fracture modes is assumed to take place without interaction. This can be justified for fracture mechanics specimens, if ductile crack growth preceding fracture is negligible.

The overall survival probability for k_c spots triggering cleavage and k_d ductile void nucleation sites is given by the product of the survival probabilities of either cleavage or ductile fracture:

$$R_k^{trans} = (1 - Q_1)^{k_c} (1 - Q_1^{duc})^{k_d} \tag{7.16}$$

The failure probability can then be obtained by summing up all possible contributions according to

$$\begin{aligned} P_f^{trans} &= 1 - \sum_{k_c=0}^{\infty} \sum_{k_d=0}^{\infty} p_{k_c} (1 - Q_1)^{k_c} p_{k_d} (1 - Q_1^{duc})^{k_d} \\ &= 1 - \exp(-M V_{pl} Q_1) \exp(-M_d V_{nuc} Q_1^{duc}) \\ &= 1 - \exp\left(-\left(\frac{\sigma_W}{\sigma_u}\right)^m\right) \exp\left(-M \int_{V_{nuc}} 1 - F_{f_0}(f_0^c(\varepsilon_{eq}^p, \vec{r}))\,\mathrm{d}V\right) \end{aligned} \tag{7.17}$$

To solve Eqn. (7.17), calculation of σ_W together with knowledge about the distribution of inclusion size and number of inclusions per unit volume is required.

A detailed analysis is scope of current work but experimental results are not yet available.

7.4 Material characterization under irradiation conditions

In terms of the local approach, irradiation damage is described mainly by the influence on yield stress. It turned out that the critical cleavage stress is not affected by irradiation effects. The basic framework of the local approach is therefore easily adopted and it is only necessary to identify a suitable description of irradiation hardening [48, 46]. It has to be ensured, however, that for the material under consideration neutron irradiation does not generate additional populations of flaws.

7.5 Failure under multiaxial loading

The influence of the degree of multiaxiality on fracture toughness of F82H steel is investigated by Huaxin Li et al. [31] for mixed mode I-III-loading. Gao & Fong Shi [26] deal with the influence of mode-mixity on ductile fracture. Hourlier & Pineau [34] and Itoh et al. [36] use tests on circumferentially pre-cracked specimens for fatigue crack propagation under mixed mode I-III-loading.

8

Summary and Conclusions

Within the present report, the status of experimental and modelling work is given for the analysis of cleavage fracture using local fracture criteria.

The experimental programme contained

- material characterization of F82Hmod reduced activation steel by specifically designed experiments on axisymmetrical notched specimens,
- identification of fracture appearance and fracture origin distribution using quantitative fractography,
- numerical analysis of stress and strain fields at fracture using elasto-plastic Finite Element Analyses,
- post-processing of Finite Element Analyses and determination of cleavage fracture parameters,
- statistical inference using maximum likelihood methods and statistical resampling techniques,
- transferability analysis between notched and pre-cracked specimens via local risk of rupture prediction,
- modelling of constraint effects for pre-cracked specimens in the framework of local fracture criteria,
- modelling of competitive failure modes in the transition regime between cleavage and ductile fracture.

The numerical models were partly applied and verified within Round Robin activities on material parameter determination for micromechanical models in the cleavage fracture regime of structural steels. The present stage of knowledge can be summarized as follows:

Transferability of cleavage fracture parameters seems to be possible for F82Hmod, if the strains at fracture are limited. For large strains, i.e. higher temperatures or low degree of multiaxiality, plastic deformation leads to the formation of shear cracks and a mixed trans-intercrystalline fracture appearance.

It is possible that different fracture modes occur under nominally identical test conditions. Identification of outliers is possible using statistical resampling methods and can be confirmed by subsequent fractographic analysis.

For transferability analysis, limitations imposed by the use of (maximum likelihood) confidence intervals for distribution parameters can be overcome by direct assessment of the respective distributions using resampling methods.

Agreement between predicted fracture origin distributions from local risk of rupture calculations and experimentally obtained results from fractographic analyses is used as indication of appropriateness of the numerical approach.

Design issues can be addressed via parametrized material behaviour description. Fracture toughness values for low-constraint situations can be obtained from scaling functions using a modified boundary layer (MBL) approach. Constraint effects and impact of multiaxial loading require additional experimental support which will be available from EUROFER97 results.

Modelling of irradiation damage is possible within the framework of local fracture criteria but relies on availability of fracture data from irradiated specimens.

Acknowledgement

This report covers work performed in the framework of the Nuclear Fusion Programme of the Forschungszentrum Karlsruhe.

Support of the European Community via the 5th framework Fusion Technology Programme under task ID TTMS-005 is gratefully acknowledged.

Numerous discussions with Prof. A. Brückner-Foit are appreciated.

References

[1] ABAQUS/Standard User's Manual (Version 5.8), Hibbit, Karlsson & Sorensen, Inc. 1998.

[2] E. Amar, A. Pineau, Application of a Local Approach to Ductil-Brittle Transition in a Low-Alloyed Steel, Nuclear Engineering and Design **105** (1987), 89-96.

[3] K.-J. Bathe, Finite Element Procedures in Engineering Analysis, Prentice-Hall, Englewood Cliffs, NJ 1982.

[4] G.E. Beltz, J.R. Rice, C.F. Shih, L. Xia, A Self-Consistent Model for Cleavage in the Presence of Plastic Flow, Acta mater. **44** (1996), 3943-33954.

[5] F.M. Beremin, A local criterion for cleavage fracture of a nuclear pressure vessel steel, Met. Trans. **14A** (1983), 2277-2287.

[6] F.M. Beremin, Cavity formation from inclusions in ductile fracture of A508 steel, Met. Trans. **12A** (1981), 723-732.

[7] P. W. Bridgman, The stress distribution at the neck of a tension specimen, Trans. ASM, **32** (1943), 553-574.

[8] British Energy Generation Ltd., Assessment of the integrity of structures containing defects - Revision 4, 2001.

[9] A. Brückner-Foit, W. Ehl, D. Munz, B. Trolldenier, The size effect and microstructural implications of the weakest link model, Fatigue Fract. Engng Mater. Struct. **13** (1990), 185-200.

[10] A. Brückner-Foit, P. Hülsmeier, H. Riesch-Oppermann, M. Sckuhr, Limitations of the Weibull Theory in Stress Fields With Pronounced Stress Gradients, Proc. 45^{th} ASME TURBO EXPO 2000, Munich (CD-ROM).

[11] A. Brückner-Foit, G.P. Nikishkov, D. Munz, Prediction of Cleavage Probability Using Higher Order Terms of the Crack Tip Field, Journal de Physique IV **6** (1996), C6-307-314.

[12] J. Cuccio et al., Probabilistic Methods for Ceramic Component Design and Implications for Standards, in: C.R. Brinkman, S.F. Duffy (eds.): Life Prediction Methodologies and Data for Ceramic Materials, ASTM STP 1201, ASTM, Philadelphia, 1994, 291-308.

[13] J.-C. Devaux, G. Rousselier, F. Mudry, A. Pineau, An Experimental Program for the Validation of Local Ductile Fracture Criteria Using Axisymmetrically Cracked Bars and Compact Tension Specimens, Engng. Fract. Mech. **21** (1985), 273-283.

[14] T.J. DiCiccio, B. Efron, Bootstrap confidence intervals, Statistical Science **11** (1996), 189-211.

[15] W.R. Corwin, A.T. Rosinski, E. van Walle (eds.), Small Specimen Test Techniques, ASTM STP 1329, ASTM, West Conshohocken, PA, 1998.

[16] G.E. Dieter, Mechanical Metallurgy, McGraw-Hill Book Company, London, 1988.

[17] M. di Fant et al., Development of a Simplified Approach for Using the Local Approach to Fracture, Journal de Physique IV Colloque C6, **6** (1996), C6-503-512.

[18] R.H. Dodds, T.L. Anderson, M.T. Kirk, A framework to correlate a/W ratio effects on elastic-plastic fracture toughness (J_c) Int. J. Fract., **48** (1991), 1-12.

[19] E 1921 - 97, Standard Test Method for Determination of Reference Temperature, T_0, for Ferritic Steels in the Transition Range, ASTM, Annual Book of ASTM Standards, Vol 03.01., 2001, 1119-1135.

[20] B. Efron, R.J. Tibshirani, An introduction to the bootstrap, Chapman & Hall, Boca Raton, 1993.

[21] ESIS P6 - 98, Procedure to Measure and Calculate Local Approach Criteria Using Notched Tensile Specimens, ESIS Document, European Structural Integrity Society, March 1998.

[22] T. Fett, D. Munz, Stress intensity factors and weight functions, Computational Mechanics Publ., Southampton, 1997.

[23] T. Fett, D. Munz, G. Thun, Strength and toughness test devices with opposite roller loading, Report FZKA 6378, Forschungszentrum Karlsruhe, 2000.

[24] E. Fuller, Mechanical properties of brittle materials, National Institute of Standards and Technology (NIST), MSEL Annual Report 1997 (unpublished).

[25] X. Gao, R.H. Dodds, Jr., An engineering approach to assess constraint effects on cleavage fracture toughness, Eng. Frac. Mech., **68** (2001), 263-283.

[26] X. Gao, C. Fong Shi, A Parametric Study of Mixed-Mode I/III Ductile Fracture in Tough Materials Under Small Scale Yielding, Engng. Fract. Mech. **60** (1998), 407-420.

[27] E.J. Gumbel, Statistics of Extremes, Columbia University Press, 1958.

[28] G.T. Hahn, The Influence of Microstructure on Brittle Fracture Toughness, Met. Trans **15A** (1984), 947-959.

[29] K. Hojo, I. Muroya, A. Brückner-Foit, Fracture toughness transition curve estimation from a notched round bar specimen using the local approach method, Nuclear Engineering and Design **174** (1997), 247-258.

[30] Y. Huang, Accurate Dilatation Rates for Spherical Voids in Triaxial Stress Fields, J. Appl. Mech. **58** (1991), 1084-1086.

[31] Huaxin Li, R.-H. Jones, J.P. Hirth, D.S. Gelles, Effect of loading mode on the fracture toughness of a reduced-activation ferritic/martensitic stainless steel, J. Nucl. Mater. **212-215** (1994), 741-745.

[32] A.L. Gurson, Continuum Theory of Ductile Rupture by Void Nucleation and Growth: Part I - Yield Criteria and Flow Rules for Porous Ductile Media, J. Engng Mat. Tech. **99** (1977), 2ff.

[33] G.T. Hahn, R.G. Hoagland, A.R. Rosenfield, The Variation of K_{Ic} with Temperature and Loading Rate, Met. Trans. **2** (1971), 537-541.

[34] F. Hourlier, A. Pineau, Fissuration par fatigue sous sollicitations polymodales (mode I ondul + mode III permanent) d'un acier pour rotors 26 NCDV 14, Memoires Scientifiques Revue Metallurgie **76** (1976), 175-185.

[35] J.W. Hutchinson, Singular behaviour at the end of a tensile crack in a hardening material, J. Mech. Phys. Solids **16** (1968), 13-31.

[36] Y.Z. Itoh, T. Murakami, H.Kashiwaya, Approximate formulae for estimating the J-integral of a circumferentially cracked round bar under tension or torsion, Eng. Frac. Mech., **31** (1988), 967-975.

[37] E. Kantidis, B. Marini, L. Allais, A. Pineau, Validation of a statistical criterion for intergranular brittle fracture of a low alloy steel through uniaxial and biaxial (tension-torsion) tests, Int. J. Fracture **66** (1994), 273-294.

[38] M. Kirk, A. Bakker (eds.), Constraint Effects in Fracture: Theory and Applications, Second Volume, ASTM STP 1244, ASTM, Philadelphia, 1995.

[39] R.W.J. Koers, A.H.M. Krom, A. Bakker, Prediction of Cleavage Fracture in the Brittle to Ductile Transition Region of a Ferritic Steel, in: [38], 191-208.

[40] J.D. Landes, D.H. Shaffer, Statistical Characterization of Fracture in the Transition Region, in: Fracture Mechanics: Twelfth Conference, ASTM STP 700, American Society for Testing and Materials (1980), 368-382.

[41] P. Ludwik, Elemente der technologischen Mechanik, Springer, 1909.

[42] R.M. McMeeking, Finite Deformation analysis of crack-tip opening in elasto-plastic material and implications for fracture, J. Mech. Phys. Solids **25** (1977), 357-381.

[43] F. Minami, A. Brückner-Foit, D. Munz, B. Trolldenier, Estimation procedure for the Weibull parameters used in the local approach, Int. J. Fract. **54** (1992), 197-210.

[44] F. Mudry, A local approach to cleavage fracture, Nucl. Engng. and Des. **105** (1987), 65-76.

[45] F. Mudry, F. di Rienzo, A. Pineau, Numerical Comparison of Global and Local Fracture Criteria in Compact Tension and Center-Crack Panel Specimens, in: J.D. Landes, A. Saxena, J.G. Merkle (eds.), Nonlinear Fracture Mechanics: Vol. II - Elastic-Plastic Fracture, ASTM STP 995 (1989), 24-39.

[46] M. Al Mundheri, P. Soulat, A. Pineau, Irradiation embrittlement of a low alloy steel interpreted in terms of a local approach of cleavage fracture, Fatigue Fract. Engng Mater. Struct. **12** (1989), 19-30.

[47] G.R. Odette, On the ductile to brittle transition in martensitic stainless steels - Mechanisms, models and structural implications, J. Nucl. Mater. **212-215** (1994), 45-51.

[48] D.M. Parks, Interpretation of irradiation effects on the fracture toughness of a pressure vessel steel in terms of crack tip stress analysis, J. Engng. Mat. Technol. **98** (1976), 30-36.

[49] A. Pineau, G. Rousselier (eds.), 1st European Mechanics of Materials Conference on Local Approach to Fracture, Journal de Physique IV **6** (1996), Colloque C6.

[50] H.G. Pisarski, K. Wallin, The SINTAP fracture toughness estimation procedure, Engineering Fracture Mechanics **67** (2000), 613-624.

[51] S. Renevey, Approches globales et locale de la rupture dans le domaine de transition fragile-ductile d'un acier faiblement allié, Rapport CEA-R-5784, CEA/Saclay, Gif-sur-Yvette, 1998.

[52] S. Renevey et al., Dictile-Brittle Transition of Ferritic Steels Modelled by the Local Approach to Fracture, Journal de Physique IV Colloque C6, **6** (1996), C6-343-352.

[53] J.R. Rice, G.F. Rosengren, Plane strain deformation near a crack tip in a power-law hardening material, J. Mech. Phys. Solids **16** (1968), 1-12.

[54] J.R. Rice, D.M. Tracey, On the ductile enlargement of voids in triaxial stress fields, J. Mech. Phys. Solids **17** (1969), 201-217.

[55] H. Riesch-Oppermann, FZK Contribution to the ESIS TC 8 Numerical Round Robin on Micromechanical Models (Phase II, Task B1), FZKA Report 6338, Forschungszentrum Karlsruhe, 1999.

[56] H. Riesch-Oppermann, Status report on cleavage fracture behaviour of EUROFER97 using local fracture criteria, FZKA Report 6668, (in preparation).

[57] H. Riesch-Oppermann, (unpublished results).

[58] H. Riesch-Oppermann, A. Brückner-Foit, WEISTRABA - A code for the numerical analysis of Weibull stress parameters from ABAQUS finite element stress analyses - Procedural background and code description -, FZKA Report 6155, Forschungszentrum Karlsruhe, August 1998.

[59] M. Rieth, Forschungszentrum Karlsruhe, personal communication.

[60] R.O. Ritchie, On the relationship between fracture toughness and Charpy V-notch energy in ultrahigh strength steel, in: [63], 54-73.

[61] R.O. Ritchie, J.F. Knott, J.R Rice, On the relationship between critical tensile stress and fracture toughness in mild steels, J. Mech. Phys. Solids **21** (1973), 395-410.

[62] R.O. Ritchie, W.L. Server, R.A. Wullaert, Critical Fracture Stess and Fracture Strain Models for the Prediction of Lower and Upper Shelf Toughness in Nuclear Pressure Vessel Steels, Metall. Trans. **10A** (1979), 1557-1569.

[63] R.A. Rosenfield et al., What does the Charpy test really tell us? ASM, Metals Park, 1978.

[64] A. Rossoll et al., Local Approach of the Charpy Test at Low Temperature, Journal de Physique IV Colloque C6, **6** (1996), C6-279-286.

[65] G. Rousselier, Ductile Fracture Models and their Potentials in Local Approach of Fracture, Nuclear Engineering and Design **105** (1987), 97-111.

[66] C. Ruggieri, R.H. Dodds, Jr., A transferability model for brittle fracture including constraint and ductile tearing effects: a probabilistic approach, Int. J. Fract. **79** (1996), 309-340.

[67] C. Sainte Catherine et al., Charpy-V and Sub-Size Charpy Tests and FE Simulation on a Low Alloy RPV Ferritic Steel, ESIS TC1 & 8 - Fracture Mechanics Offshore Structures, Trondheim, August 25-27, 1999.

[68] M. Sckuhr, Spannungssingularitäten und deren Bewertung in mechanisch beanspruchten Zweistoffverbunden unter Berücksichtigung der Plastizität, PhD Thesis, University of Karlsruhe, 1997.

[69] A.N. Stroh, The formation of cracks as a result of plastic flow, Proc. Roy. Soc. **212** (1954), 404-414.

[70] H. Tada, P. Paris, G.R. Irwin. The Stress Analysis of Cracks Handbook, Second Ed., Paris Productions Inc., St. Louis, Missouri, 1985.

[71] D.R. Thoman, L.J. Bain, C.E. Antle, Inferences on the Parameters of the Weibull Distribution, Technometrics, **11** (1969), 445-460.

[72] V. Tvergaard, A. Needleman, Analysis of the cup-cone fracture in a round tensile bar, Acta Metall. **32** (1984), 157-169.

[73] V. Tvergaard, A. Needleman, An analysis of the brittle-to-ductile transition in dynamic crack growth, Int. J. Fract. **59** (1993), 53-67.

[74] M. Valo, K. Wallin, K. Törrönen, Comparison of Charpy-V and J-integral transition temperature shifts in CrMoV pressure vessel steels, Int. J. Pres. Ves. & Piping **55** (1993), 81-88.

[75] K. Wallin, M. Valo, R. Rintamaa, K. Törrönen, R. Ahlstrand, Descriptive characteristics of different types of test for irradiation embrittlement, Nucl. Engng. and Des. **159** (1995), 69-80.

[76] M. Walter, Mechanische und fraktographische Charakterisierung des niedrigaktivierbaren Chromstahls F82H-mod im spröd-duktilen Übergangsbereich, Dissertation, Report FZKA 6657, Forschungszentrum Karlsruhe, (in preparation).

[77] M. Walter, J. Aktaa, M. Klotz, Entw icklung und Aufbau eines Meßsystems zur Erfassung von Konturen gekerbter Zugproben, Report FZKA 6022, Forschungszentrum Karlsruhe, 1997.

[78] L. Xia, C.F. Shih, Ductile Crack Growth - I. A Numerical Study Using Computational Cells With Microstructurally-Based Length Scales, J. Mech. Phys. Solids **43** (1995), 233-259.

[79] L. Xia, C.F. Shih, Ductile Crack Growth - II. Void Nucleation and Geometry Effects on Macroscopic Fracture Behaviour, J. Mech. Phys. Solids **43** (1995), 1953-1981.

[80] L. Xia, C.F. Shih, Ductile Crack Growth - III. Transition to Cleavage Fracture Incorporating Statistics, J. Mech. Phys. Solids **44** (1996), 603-639.

[81] S. Yang, Y.J. Chao, M.A. Sutton, Higher order asymptotic crack tip fields in a power-law hardening material, Engng. Fract. Mech. **45** (1993), 1-20.

[82] C. Ziegler, Bewertung der Zuverlässigkeit keramischer Komponenten bei zeitlich veränderlichen Spannungen und bei Hochtemperaturbelastung, Fortschritt-Berichte VDI Reihe 18 Nr. 238, VDI Verlag Düsseldorf, 1998.

Appendix A

Figures

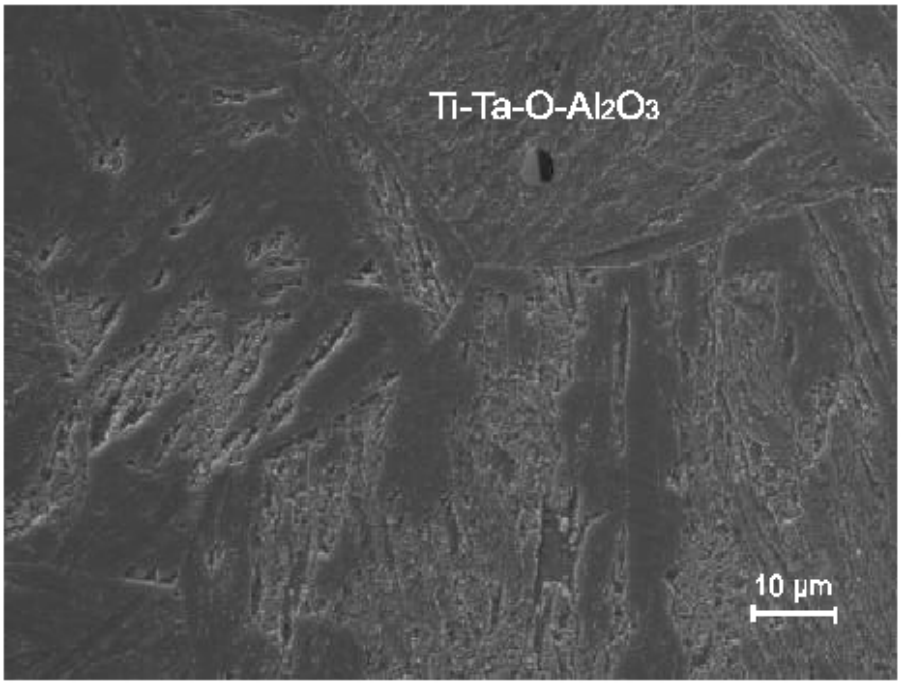

Figure A.1: SEM section of F82Hmod in reference condition.

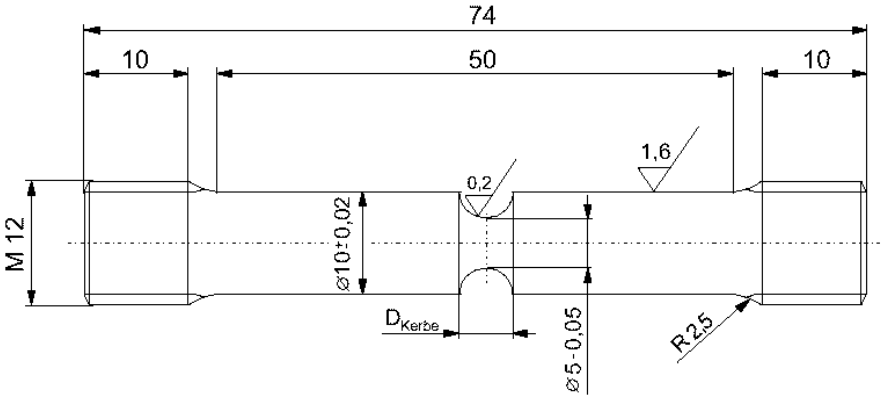

Figure A.2: Geometry of axisymmetrically notched bar (RNB) specimens.

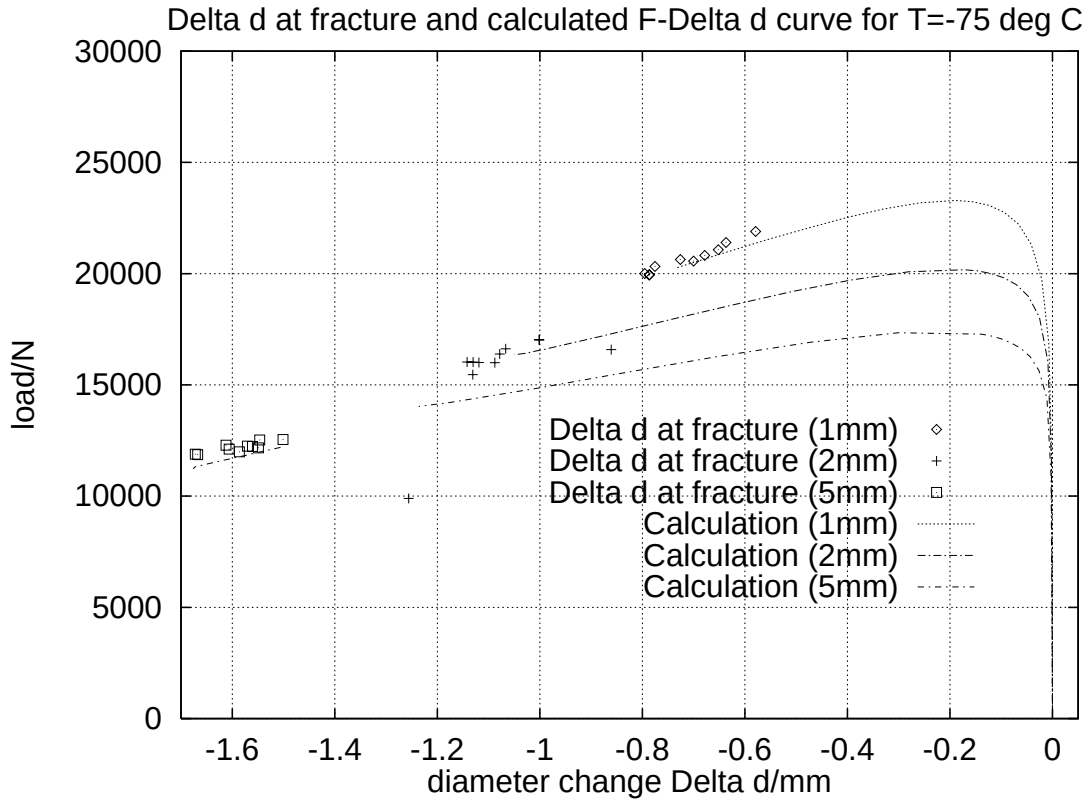

Figure A.3: Calculated $F - \Delta d$-curves and experimental Δd at fracture (-75° C).

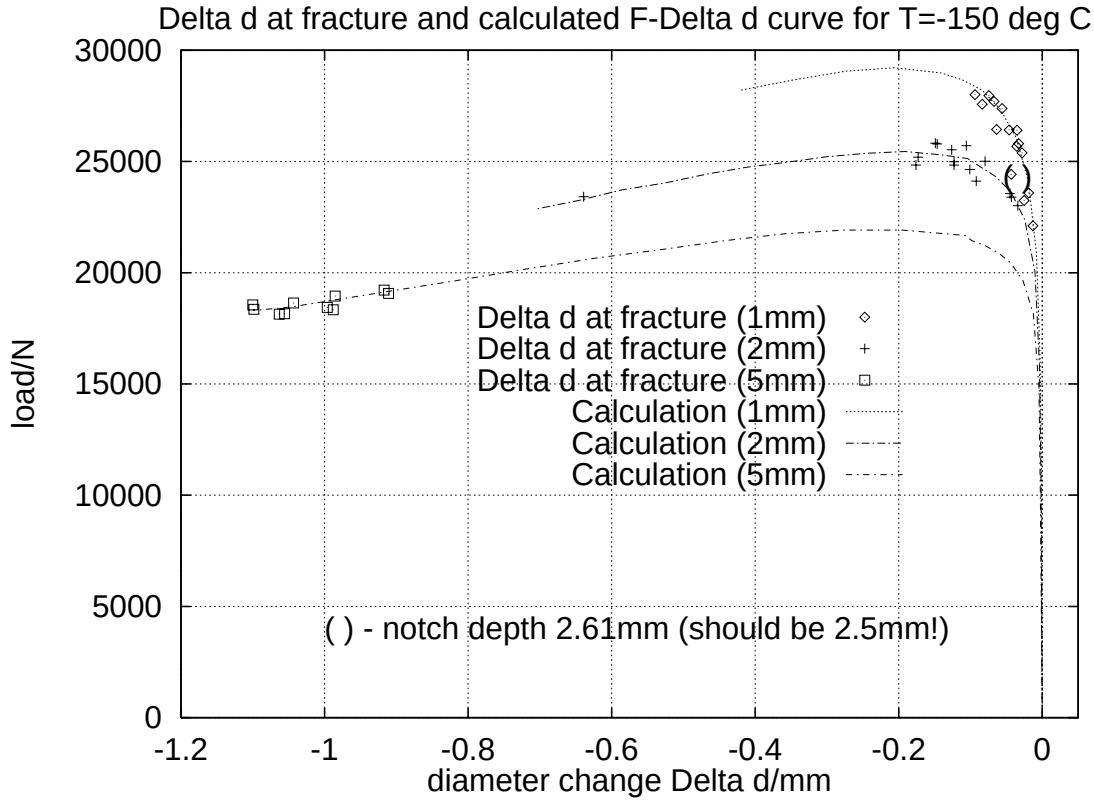

Figure A.4: Calculated $F - \Delta d$-curves and experimental Δd at fracture (-150° C).

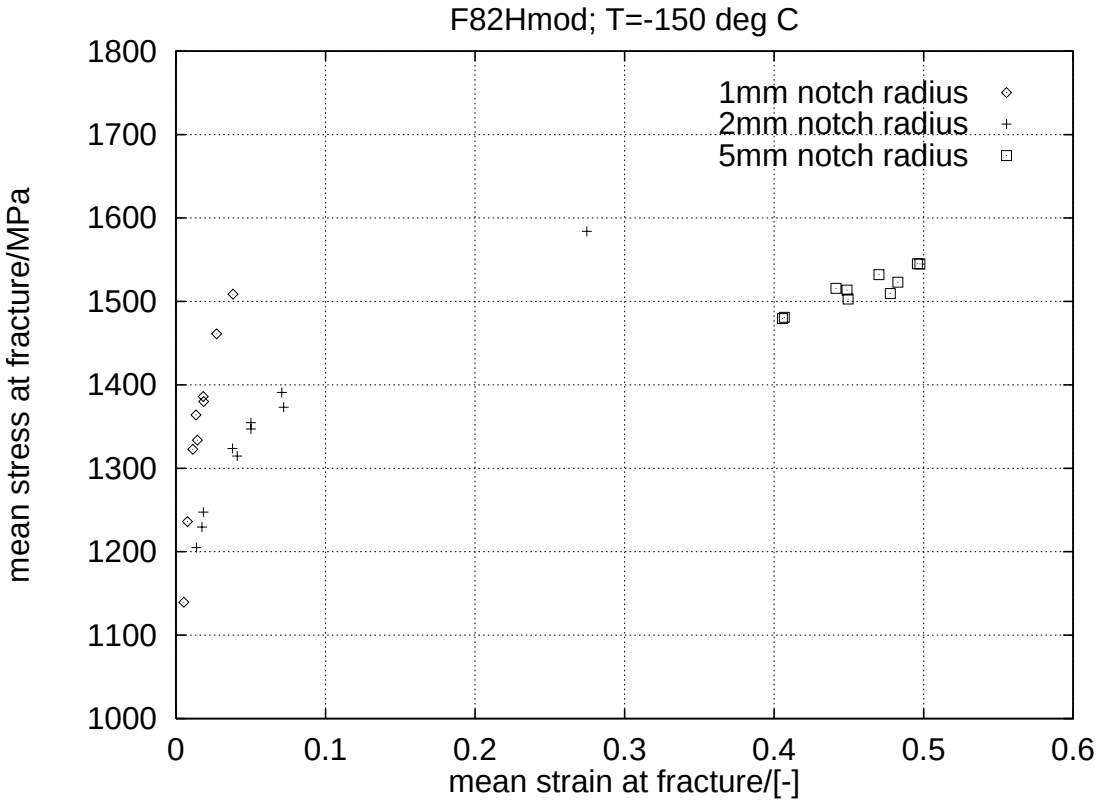

Figure A.5: Mean stress σ_M and strain ε_M at fracture (-150° C).

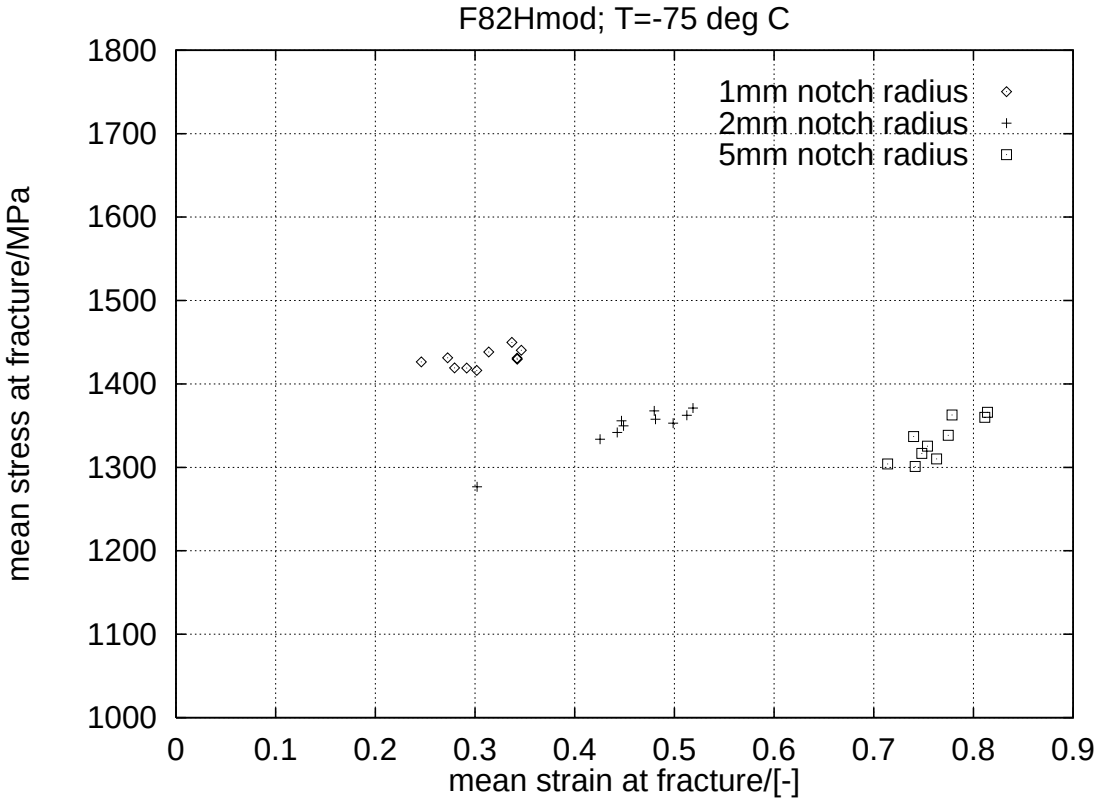

Figure A.6: Mean stress σ_M and strain ε_M at fracture (-75° C).

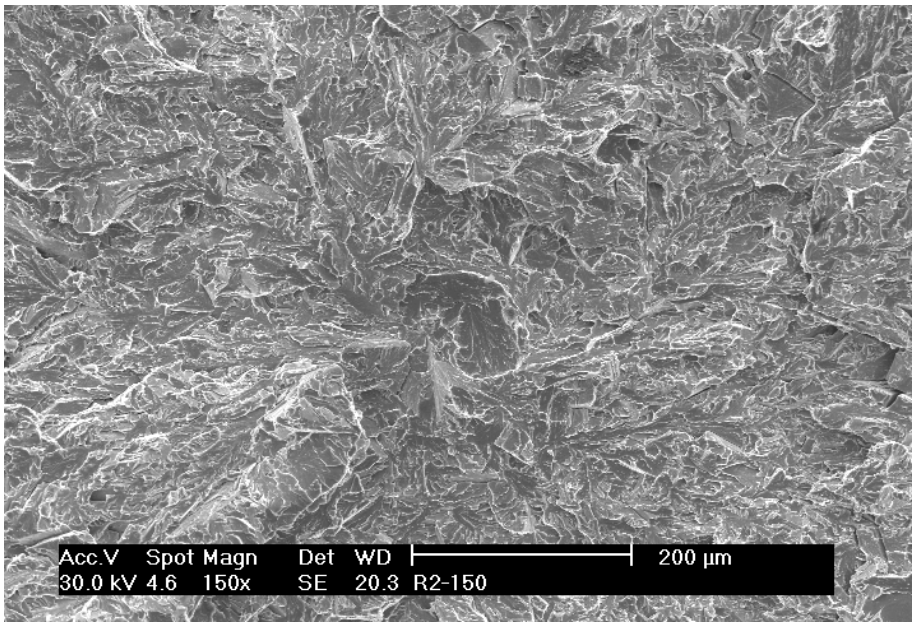

Figure A.7: Fracture surface for 2mm notched specimen tested at -150° C.

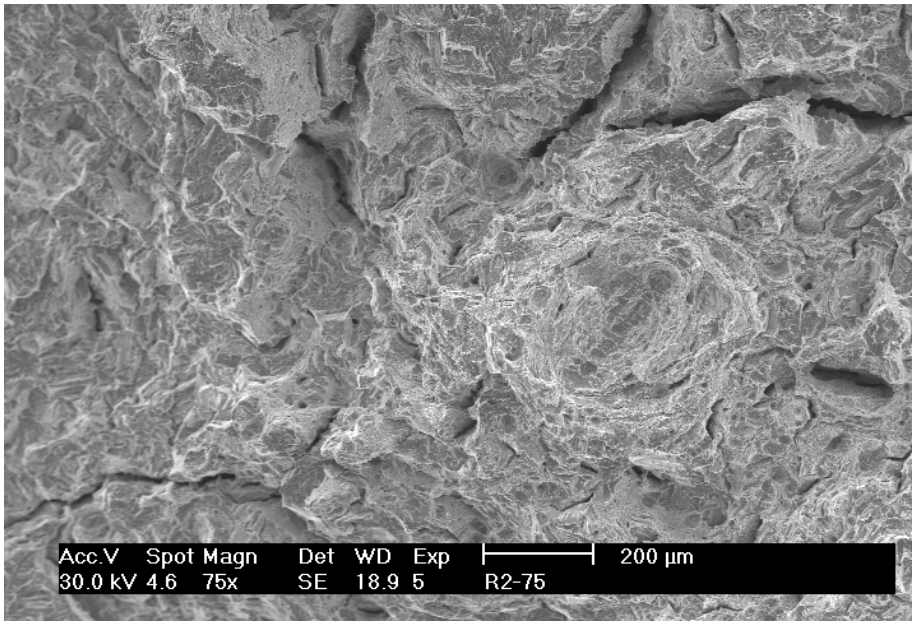

Figure A.8: Fracture surface for 2mm notched specimen tested at -75° C.

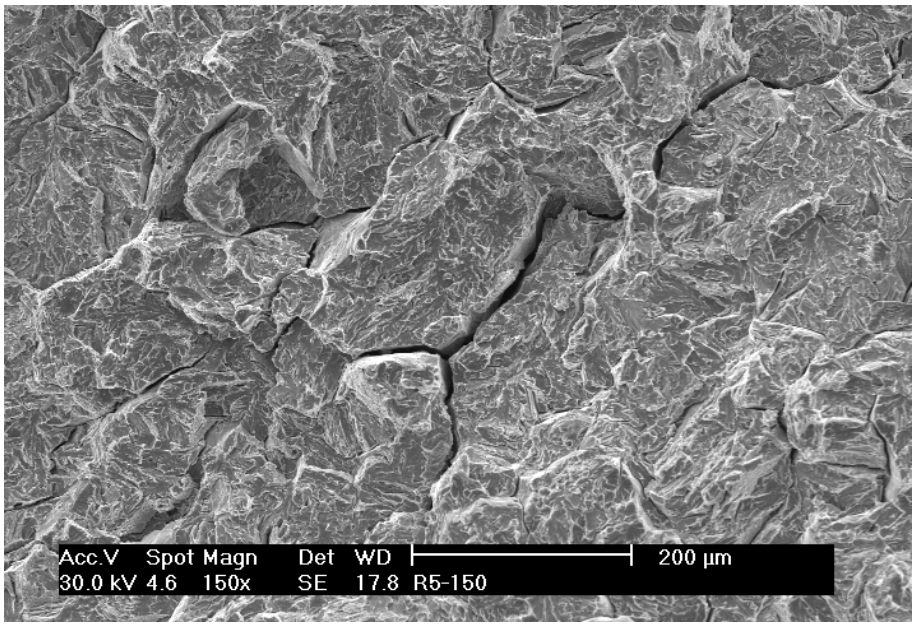

Figure A.9: Fracture surface for 5mm notched specimen tested at -150° C.

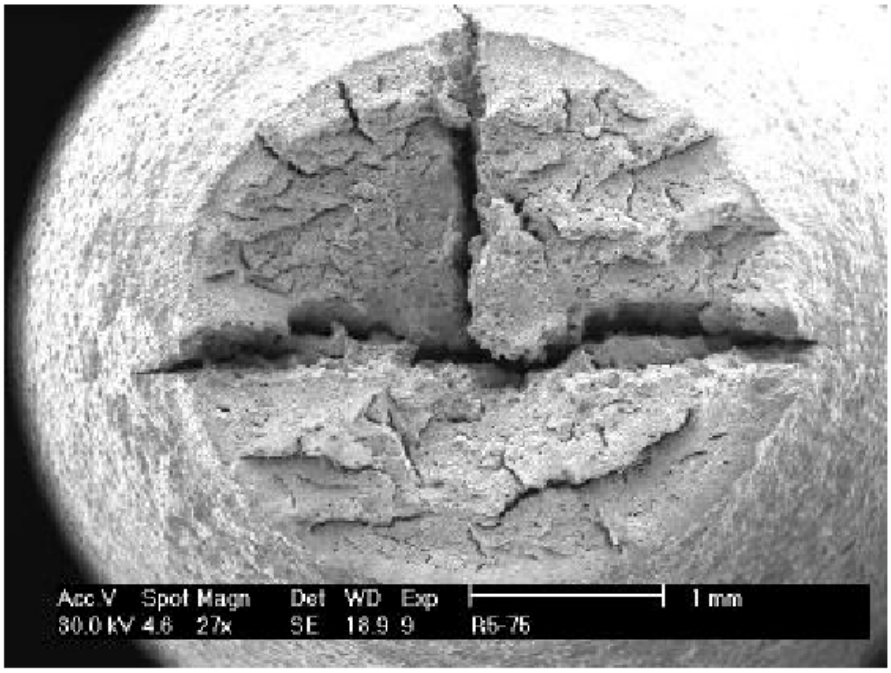

Figure A.10: Axial cracks on fracture surface of 5mm notched specimen tested at -75° C.

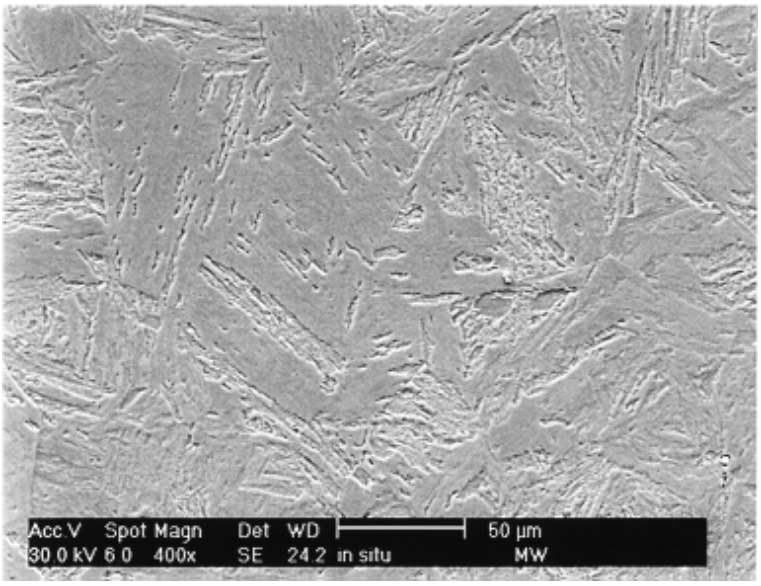

Figure A.11: Orientation of martensite laths in undeformed part of the specimen.

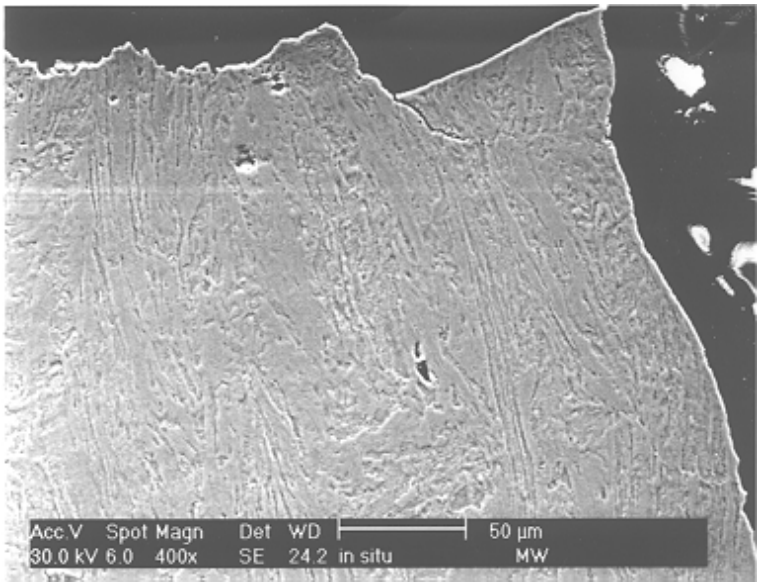

Figure A.12: Orientation of martensite laths in deformed part of the specimen.

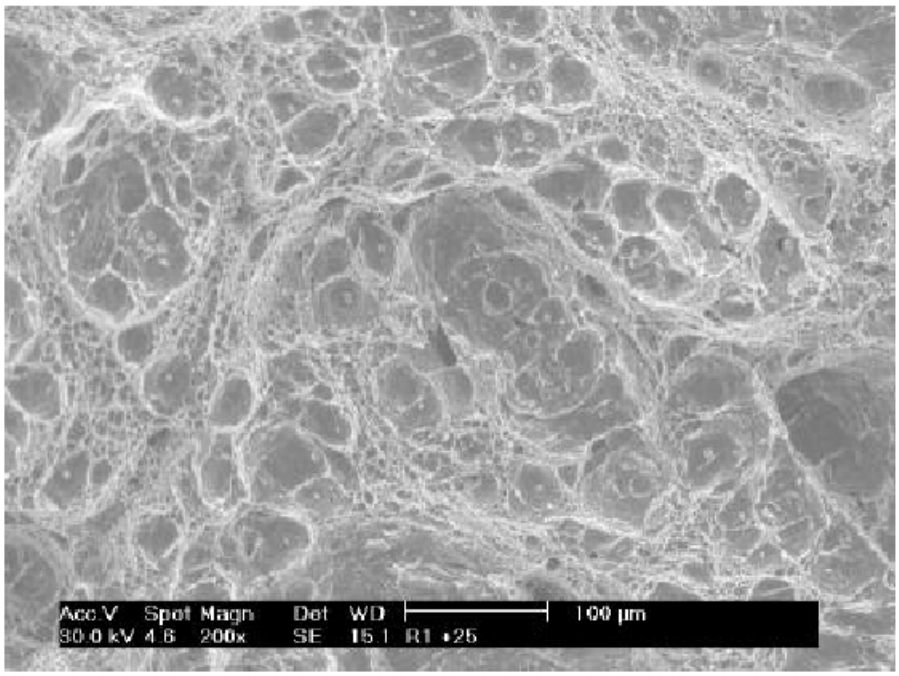

Figure A.13: Fracture surface for 1mm notched specimen tested at ambient temperature.

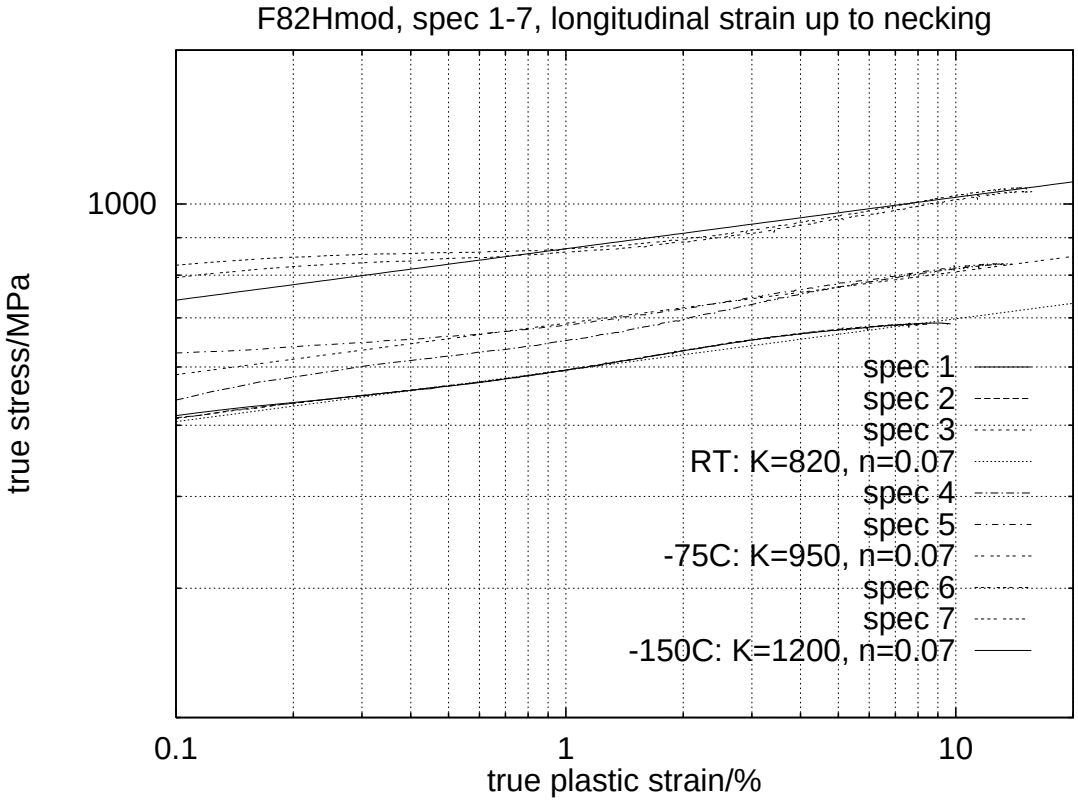

Figure A.14: F82Hmod stress-strain curves for smooth tensile specimens.

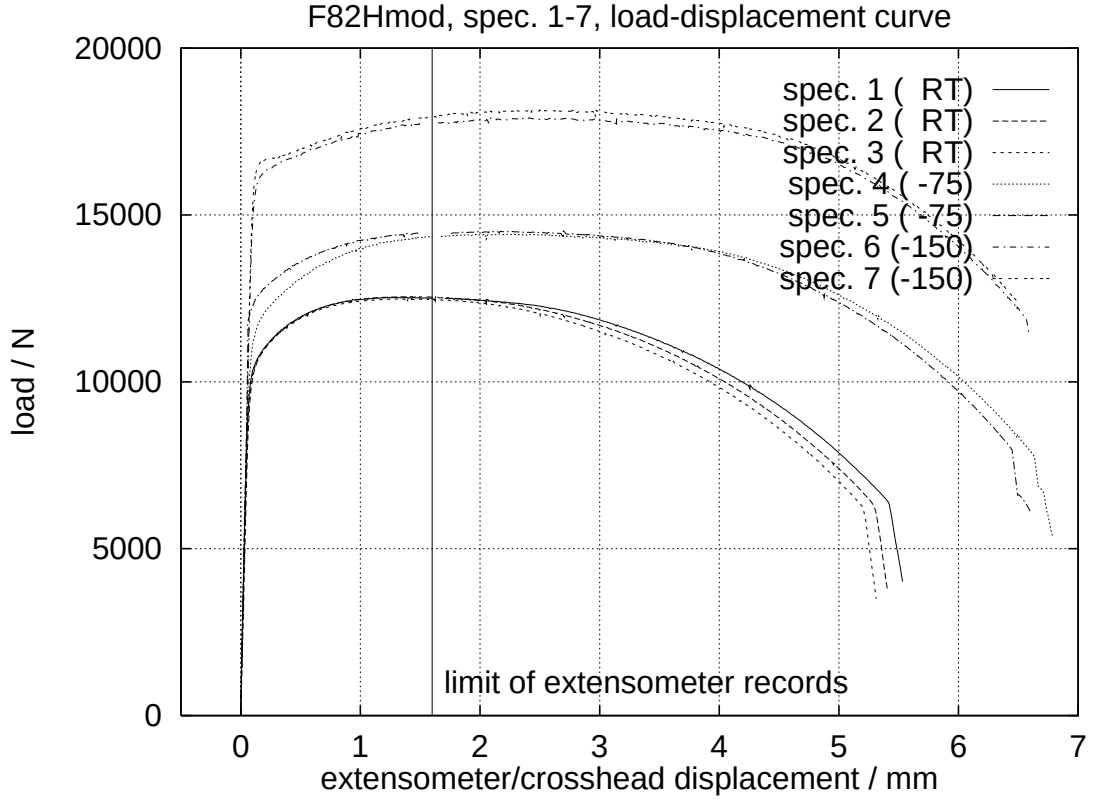

Figure A.15: F82Hmod load-displacement curves for smooth tensile specimens.

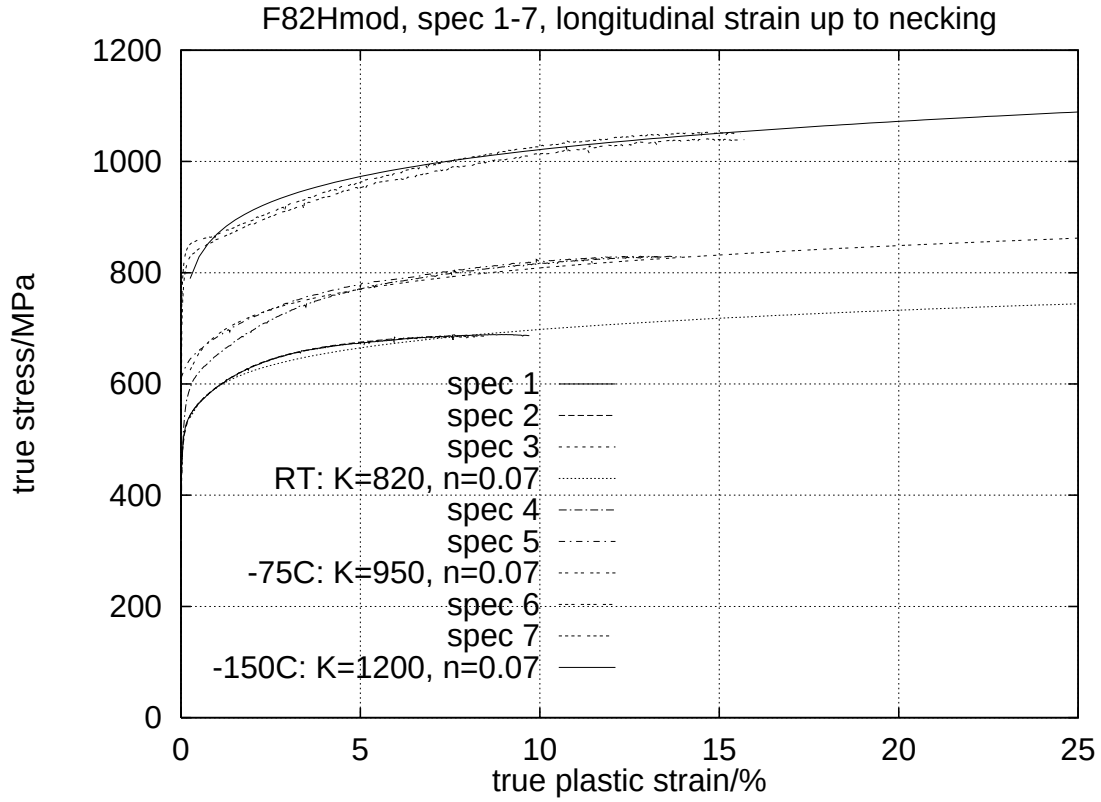

Figure A.16: F82Hmod stress-strain curves for smooth tensile specimens.

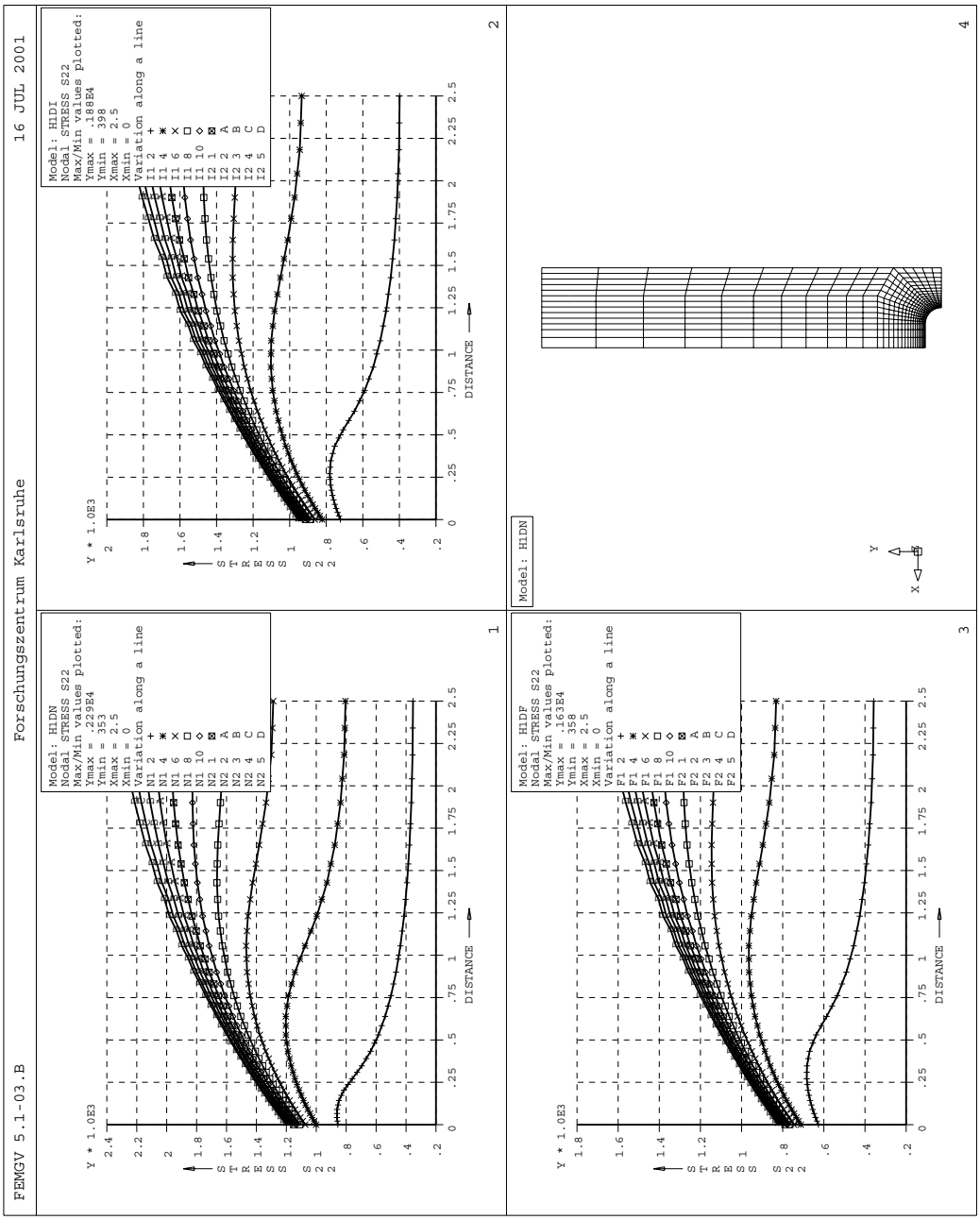

Figure A.17: F82Hmod axial stress curves for 1mm notched tensile specimens.

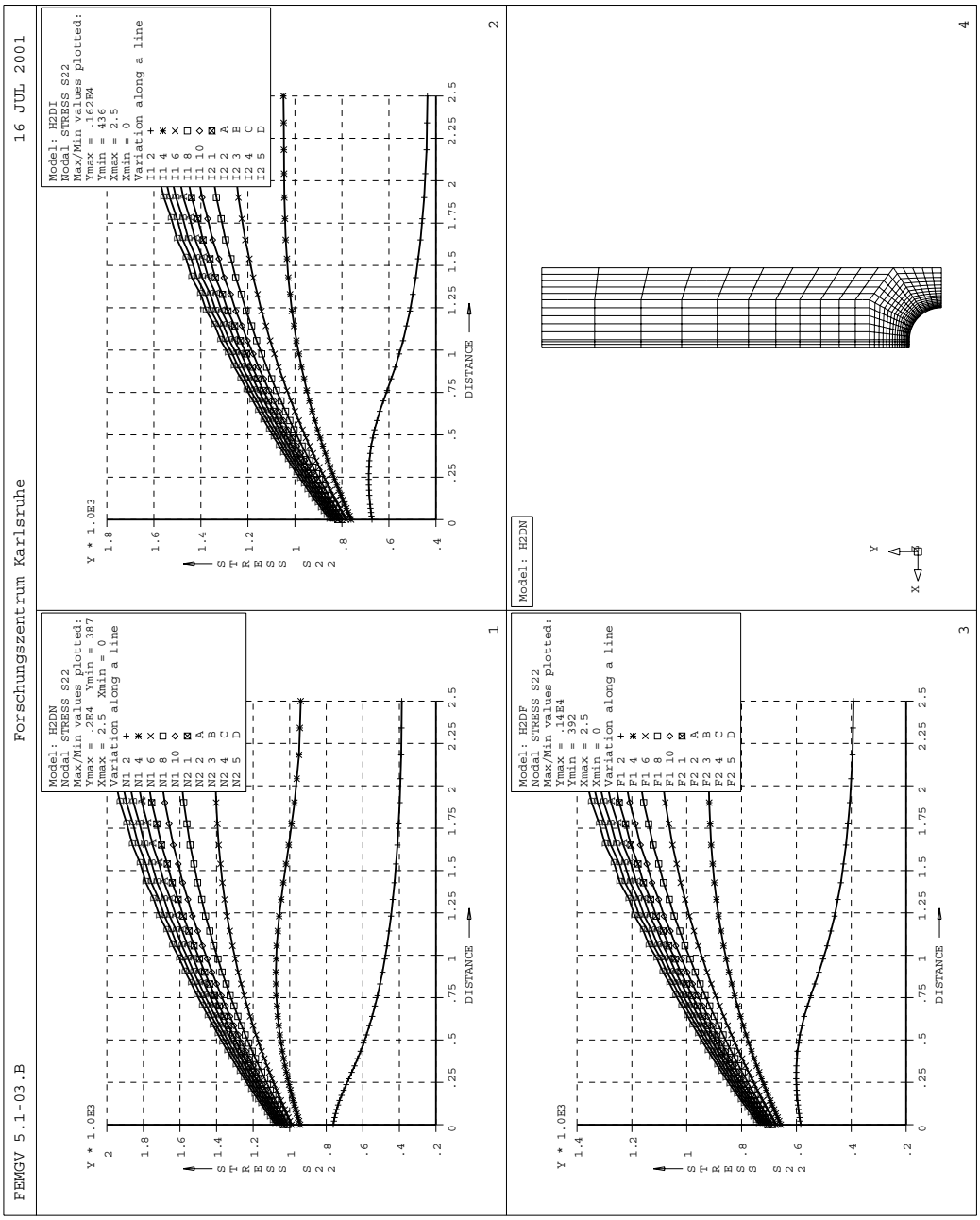

Figure A.18: F82Hmod axial stress curves for 2mm notched tensile specimens.

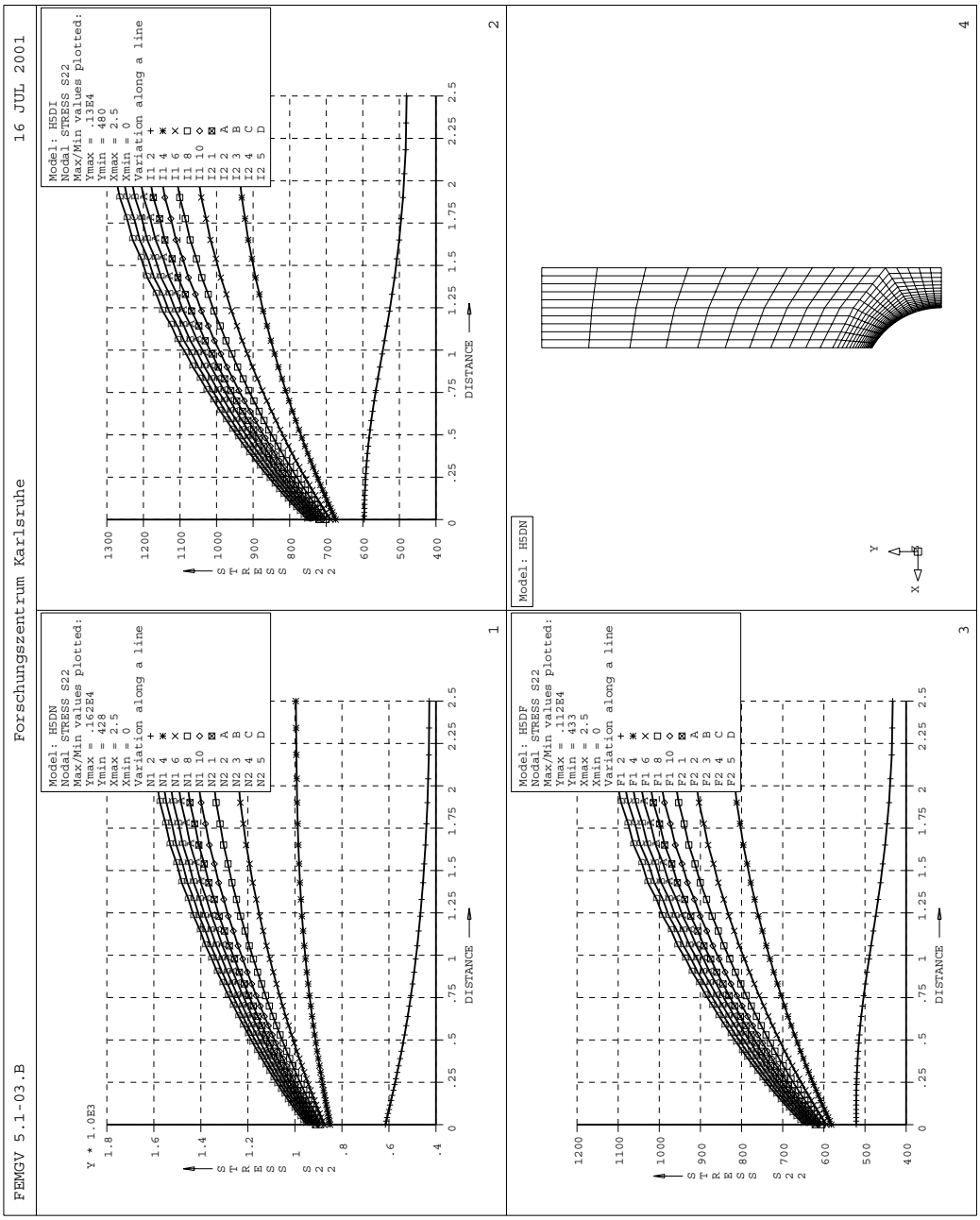

Figure A.19: F82Hmod axial stress curves for 5mm notched tensile specimens.

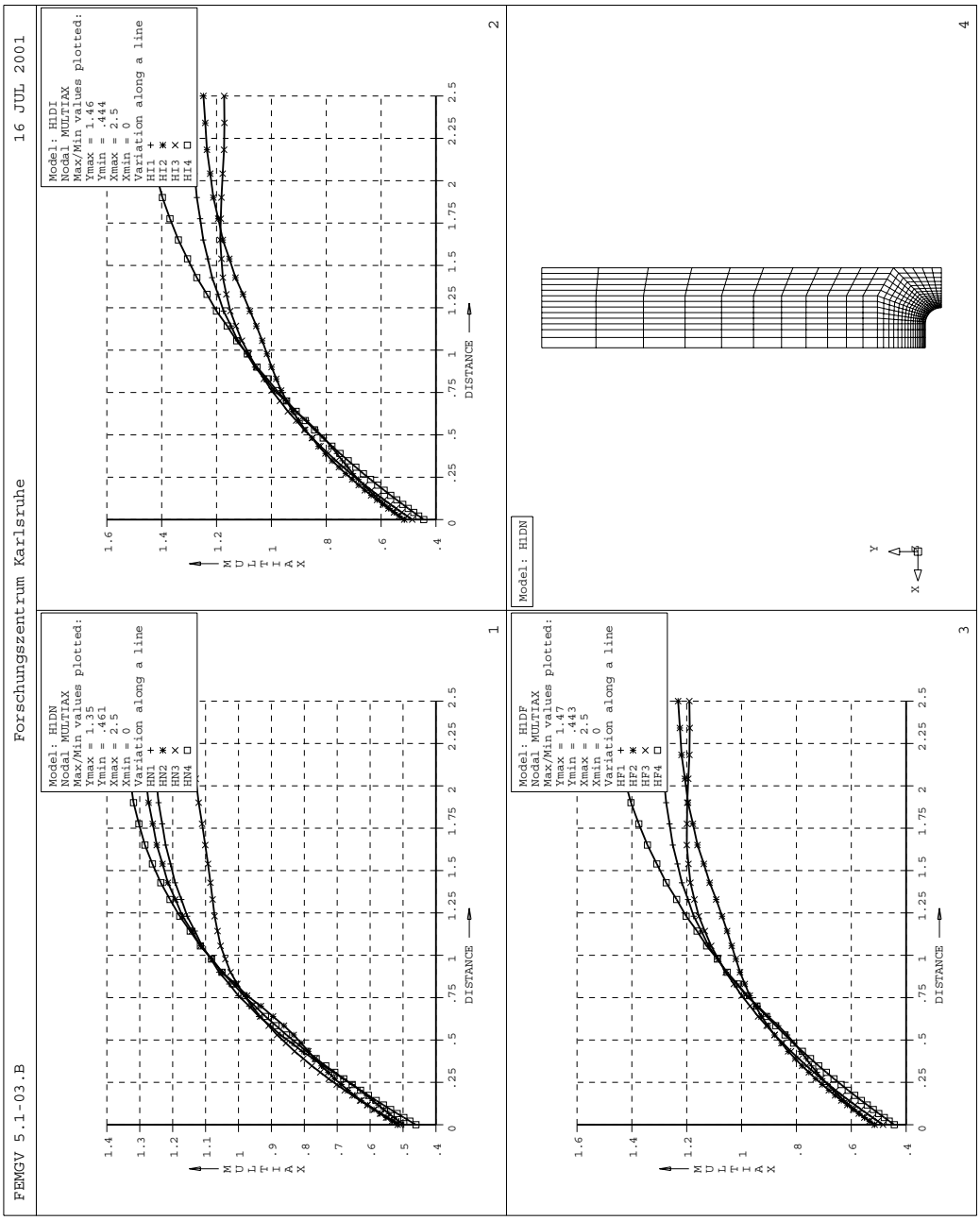

Figure A.20: F82Hmod multiaxiality curves for 1mm notched tensile specimens.

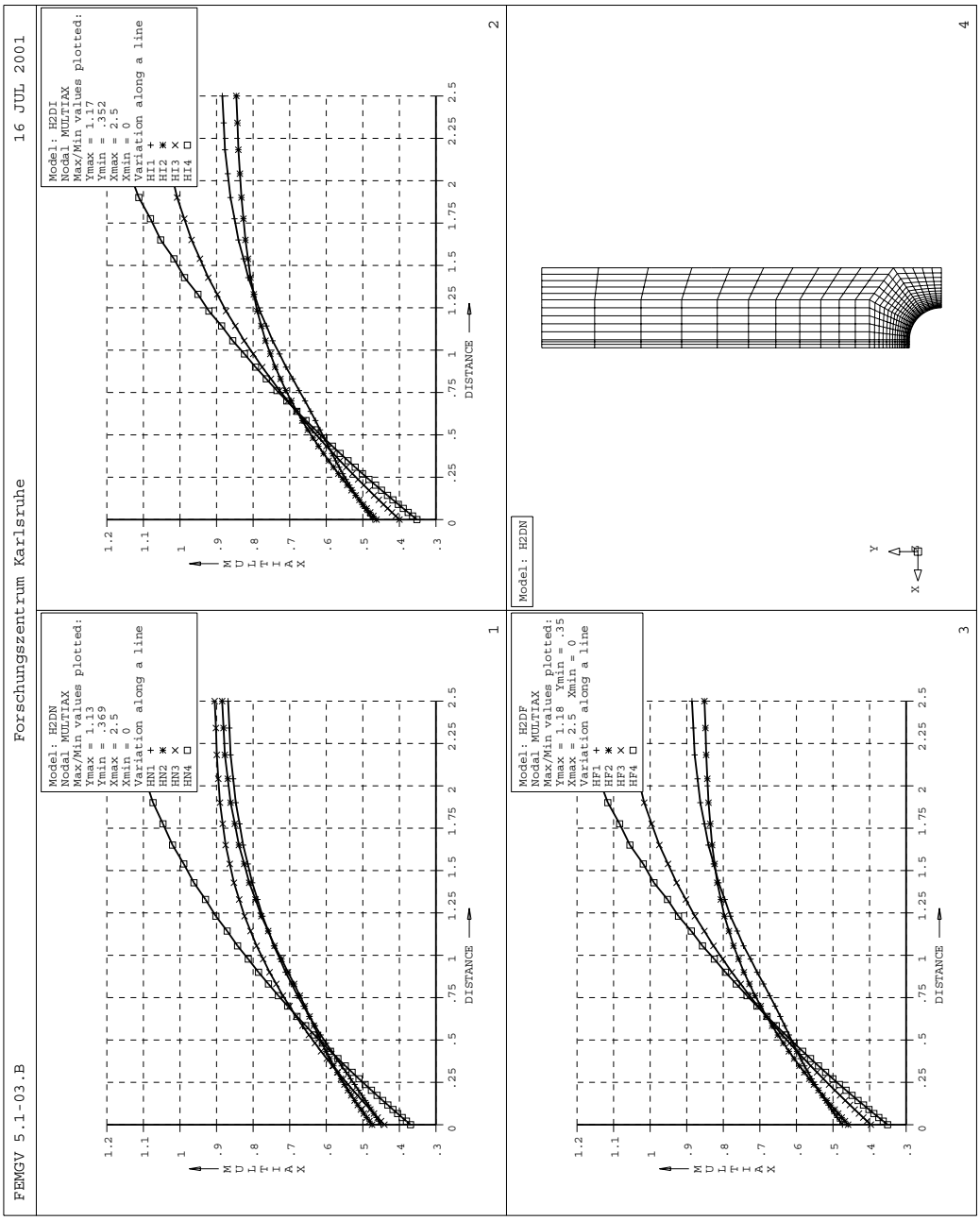

Figure A.21: F82Hmod multiaxiality curves for 2mm notched tensile specimens.

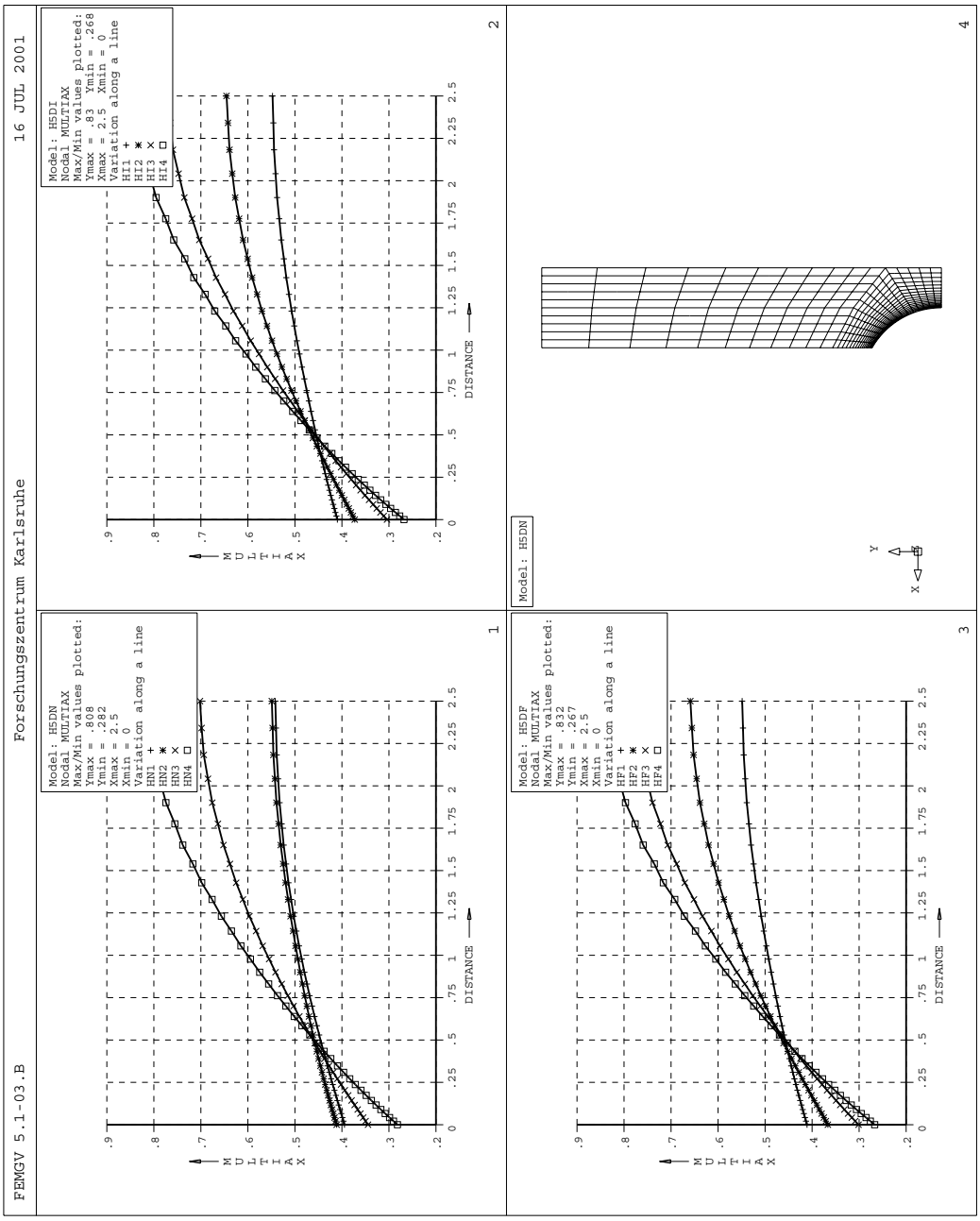

Figure A.22: F82Hmod multiaxiality curves for 5mm notched tensile specimens.

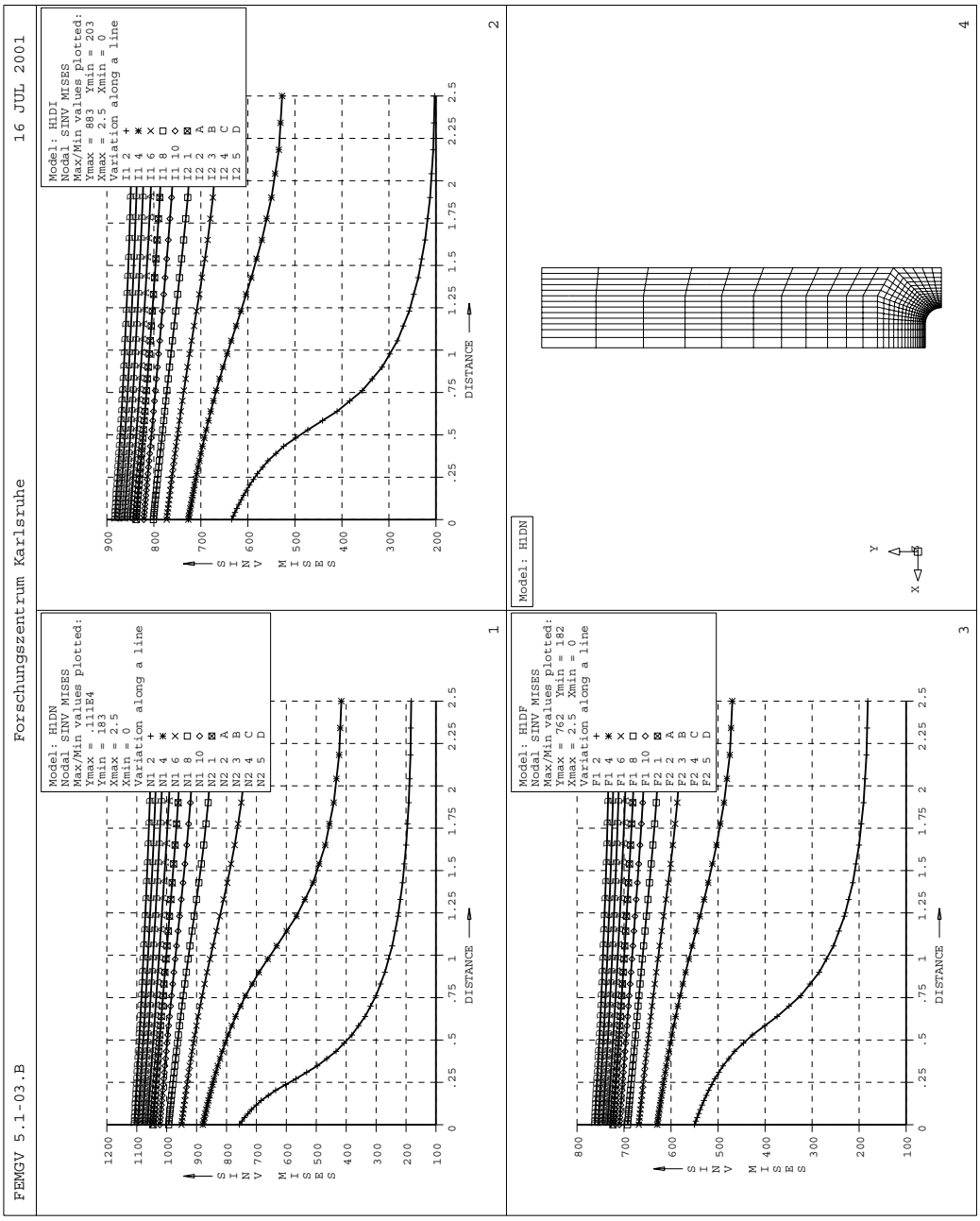

Figure A.23: F82Hmod von Mises stress curves for 1mm notched tensile specimens.

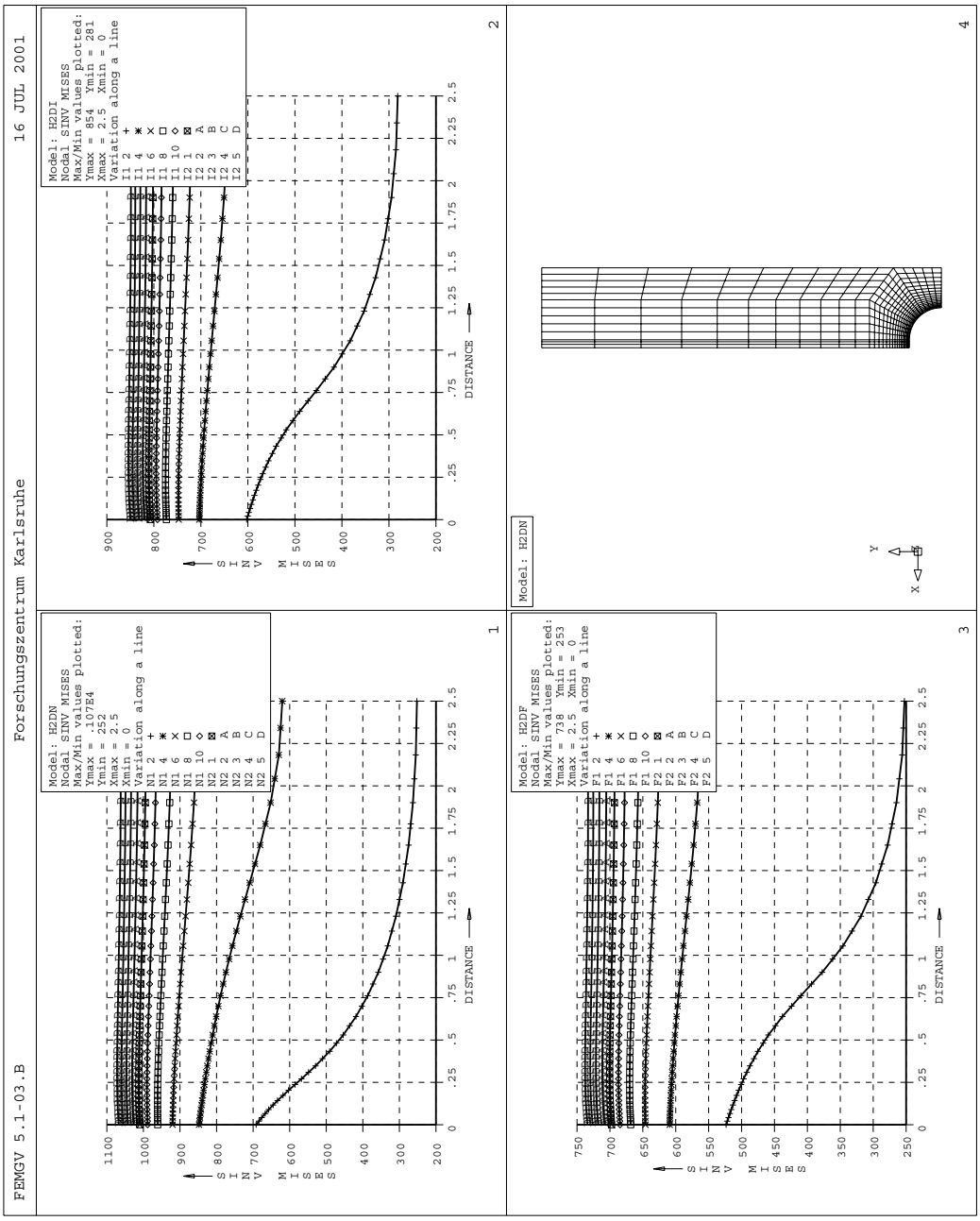

Figure A.24: F82Hmod von Mises stress curves for 2mm notched tensile specimens.

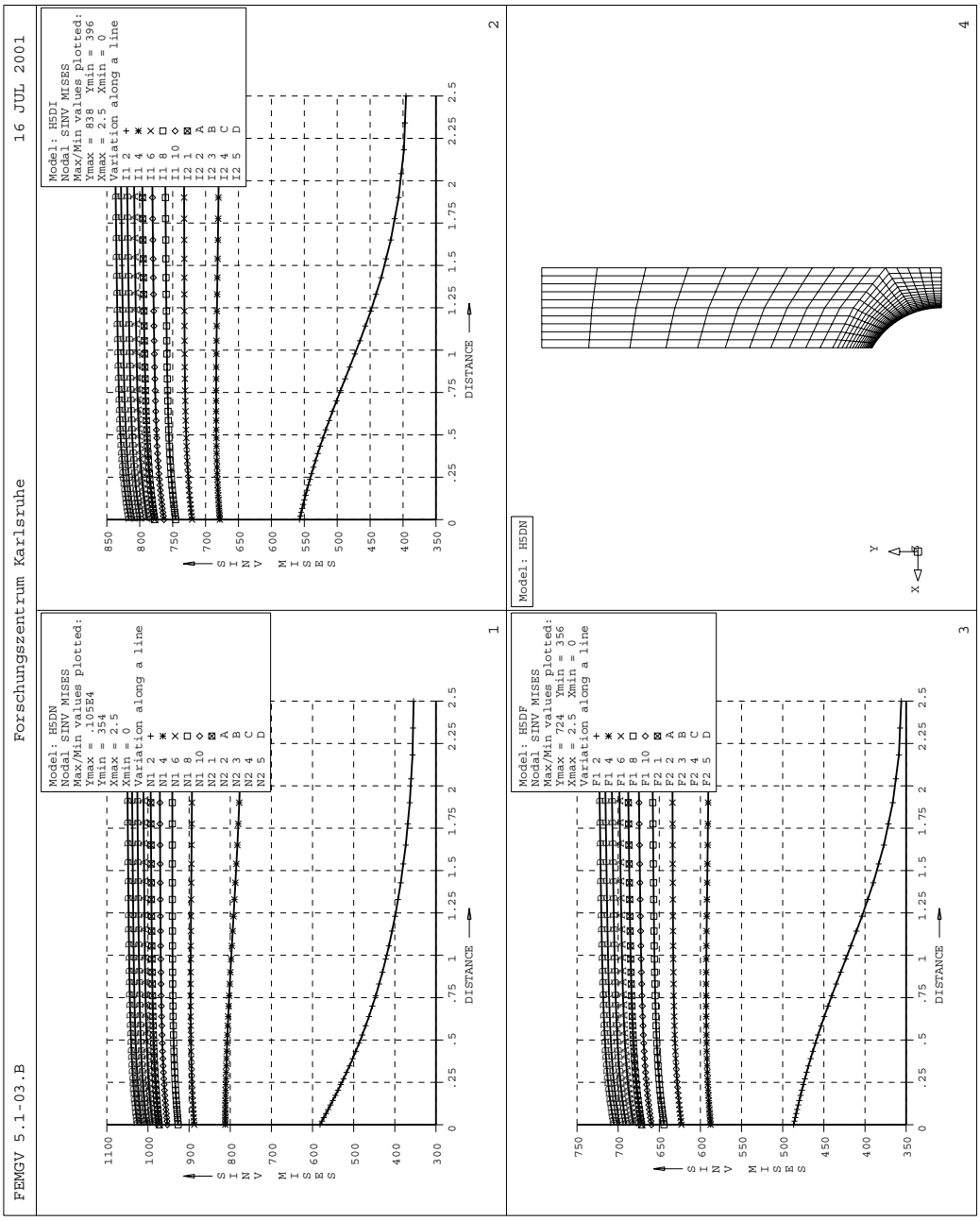

Figure A.25: F82Hmod von Mises stress curves for 5mm notched tensile specimens.

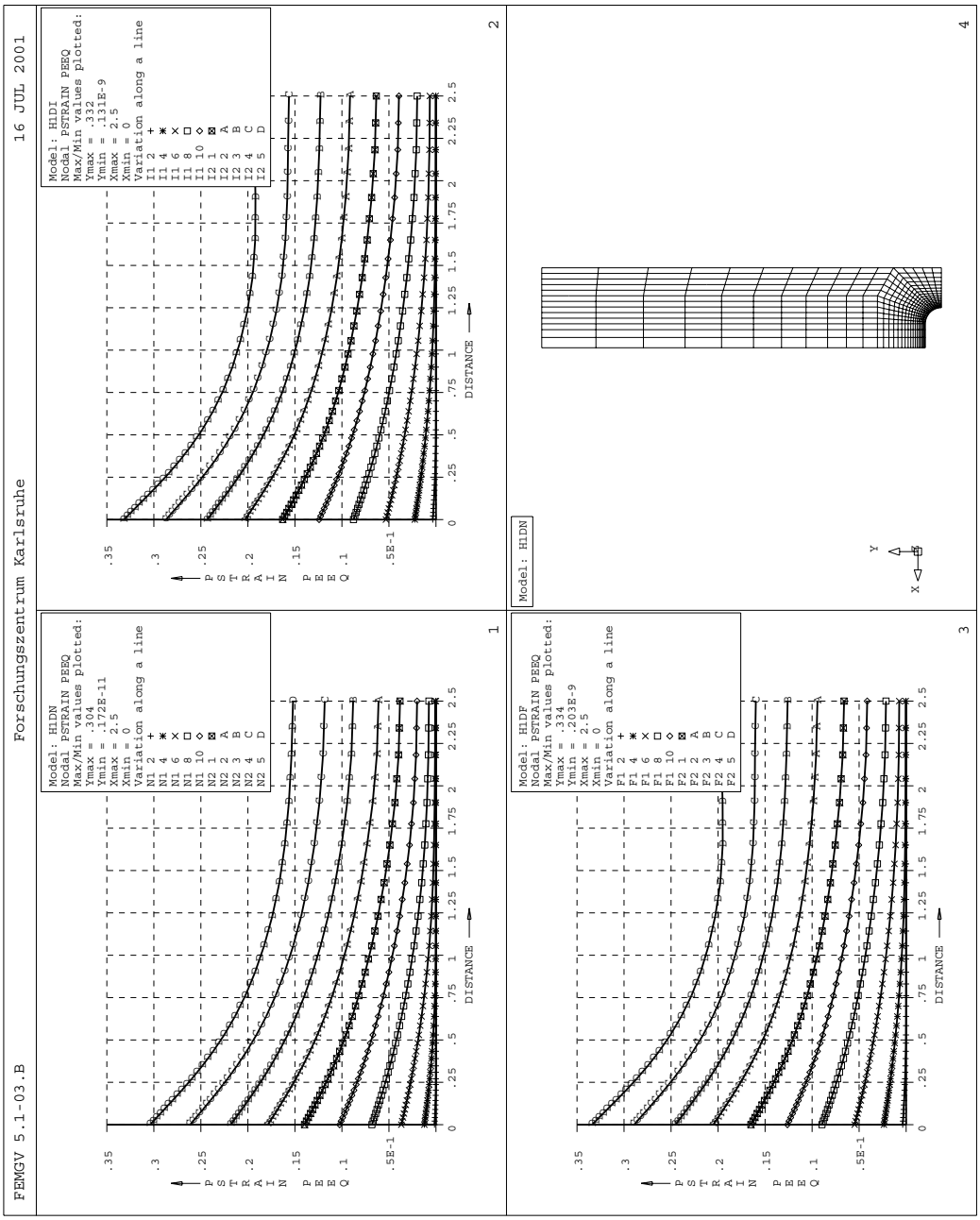

Figure A.26: F82Hmod equivalent plastic strain curves for 1mm notched tensile specimens.

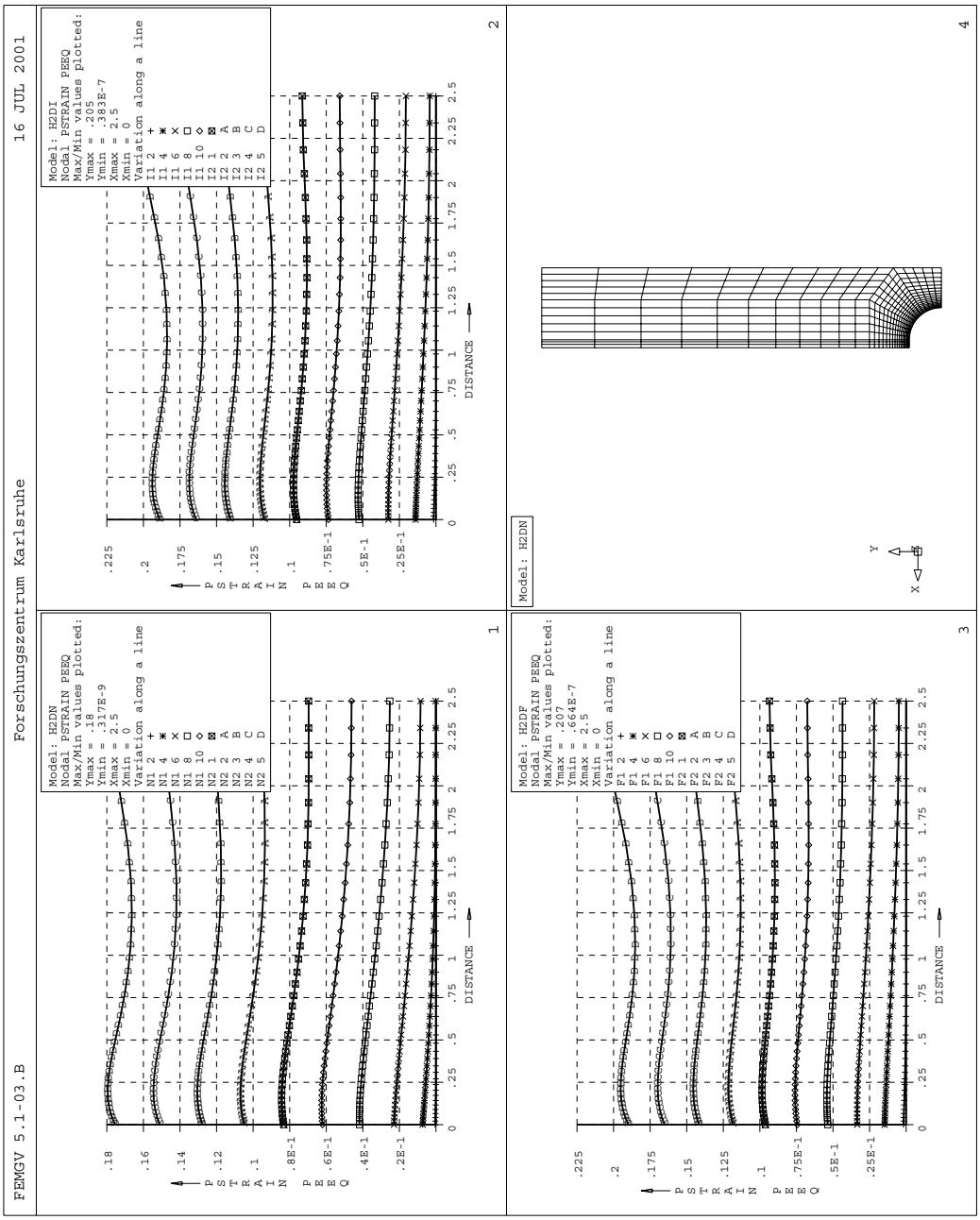

Figure A.27: F82Hmod equivalent plastic strain curves for 2mm notched tensile specimens.

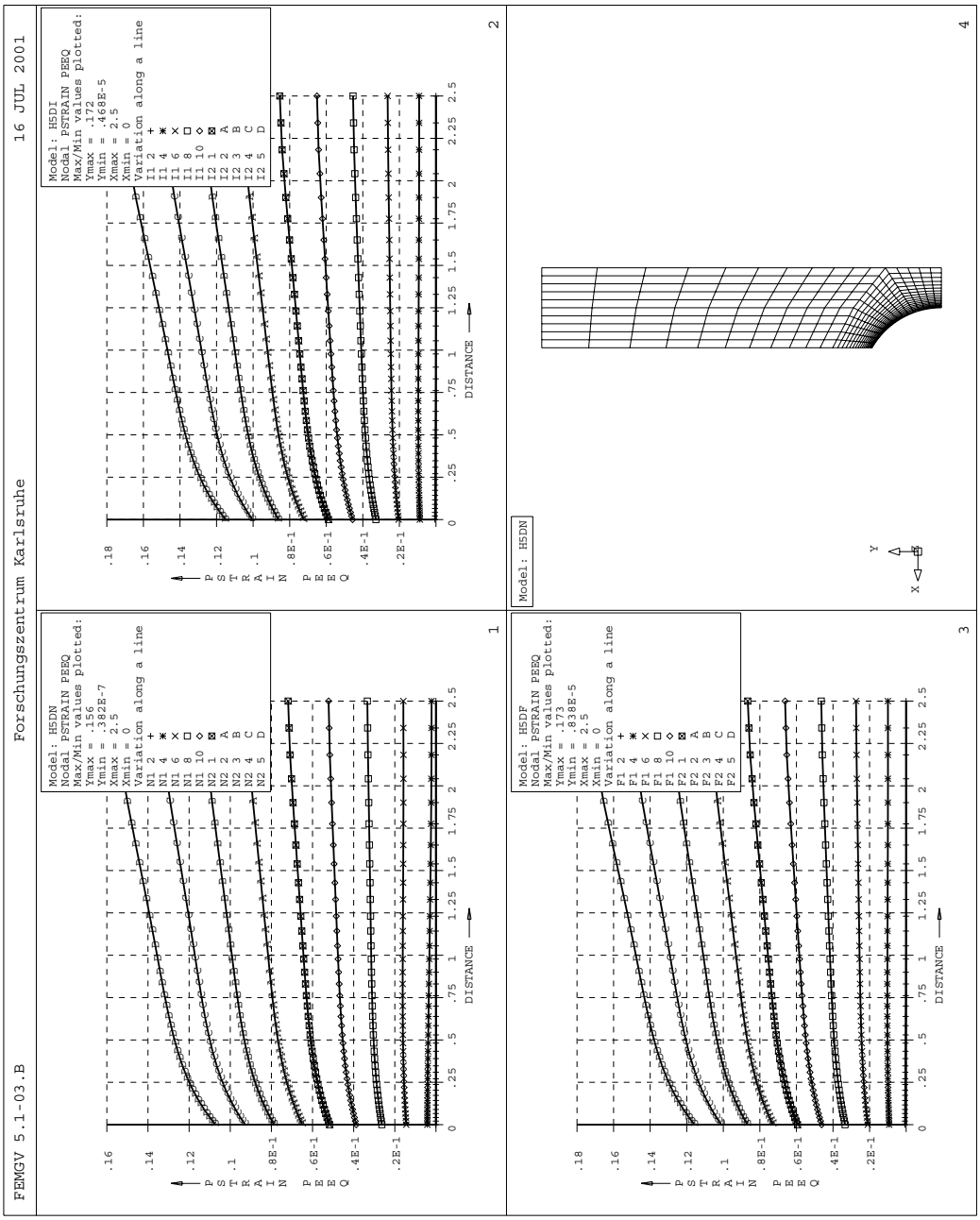

Figure A.28: F82Hmod equivalent plastic strain curves for 5mm notched tensile specimens.

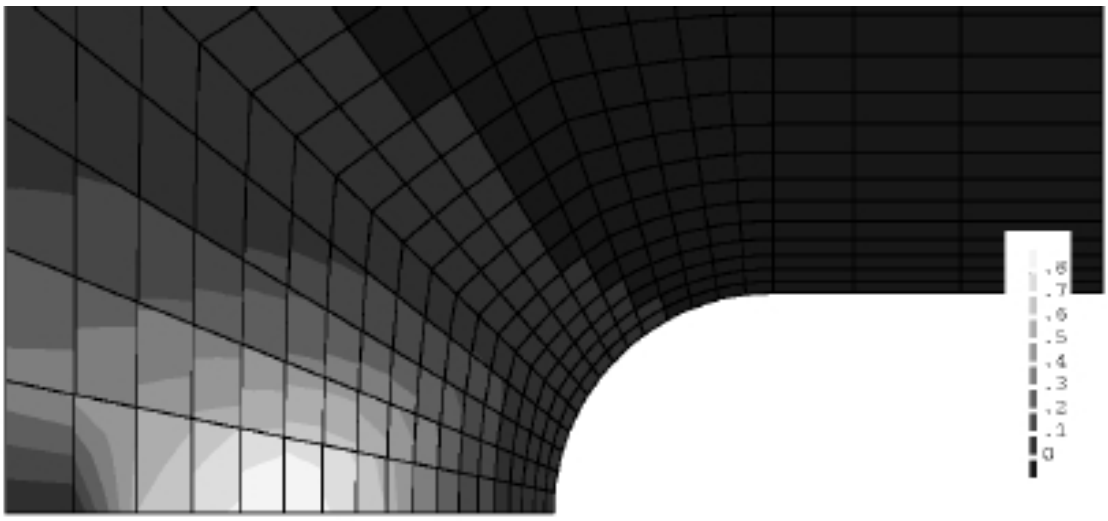

Figure A.29: Calculated local risk of rupture density for r=1mm notched specimen at -150° C at low load level.

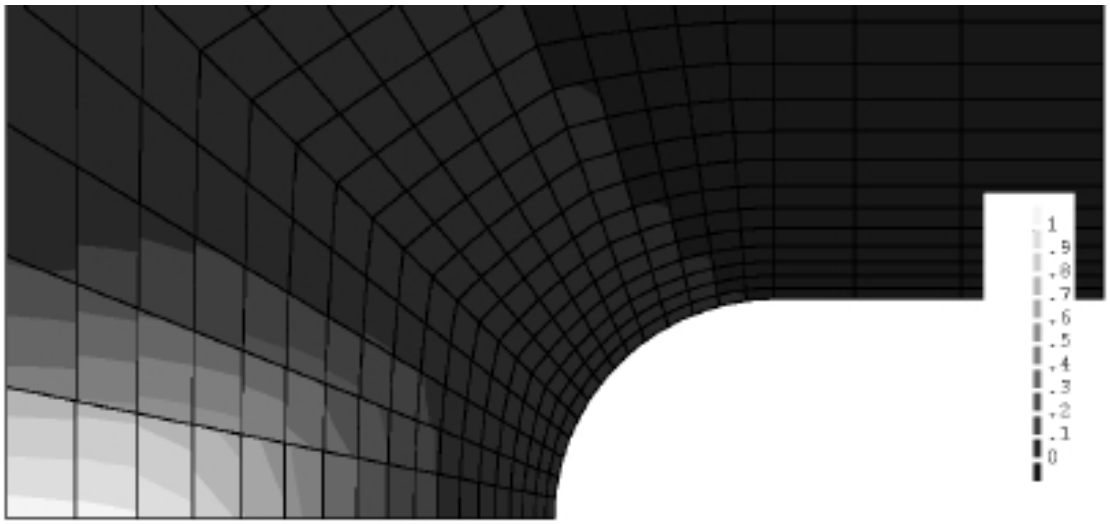

Figure A.30: Calculated local risk of rupture density for r=1mm notched specimen at -150° C at high load level.

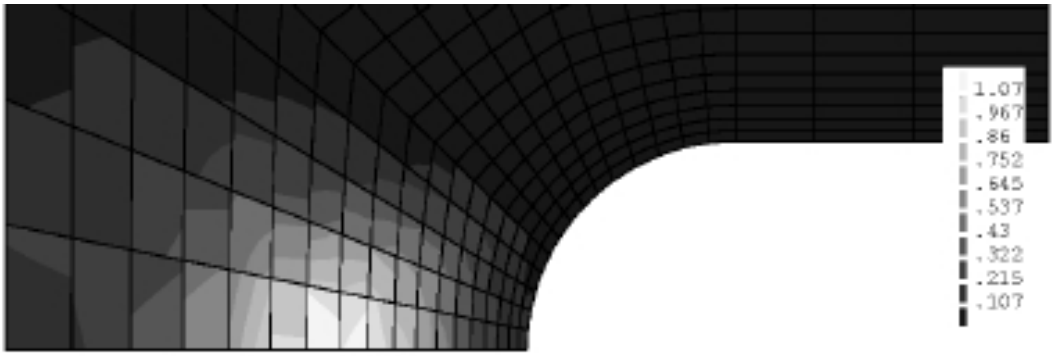

Figure A.31: Calculated fracture origin distribution for r=1mm notched specimen at -150° C.

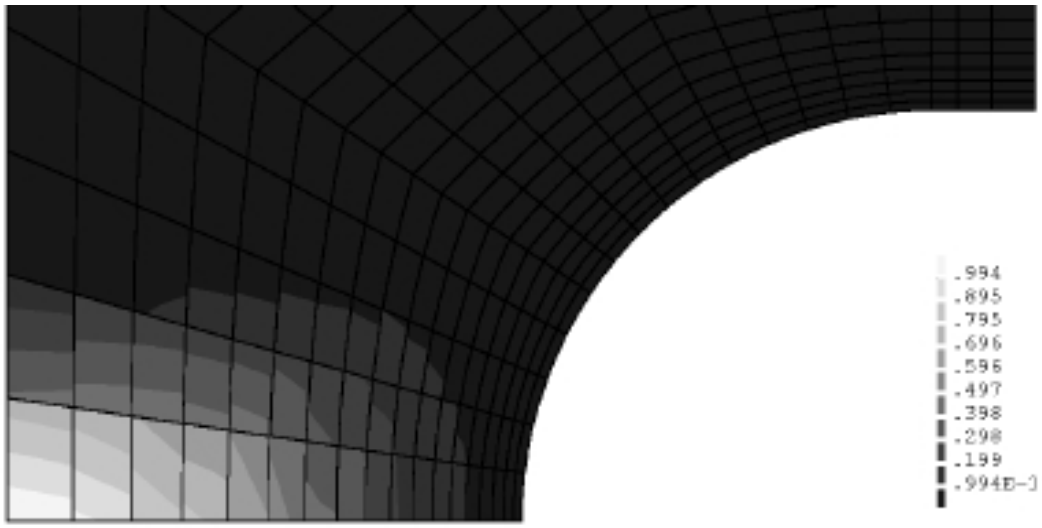

Figure A.32: Calculated fracture origin distribution for r=2mm notched specimen at -150° C.

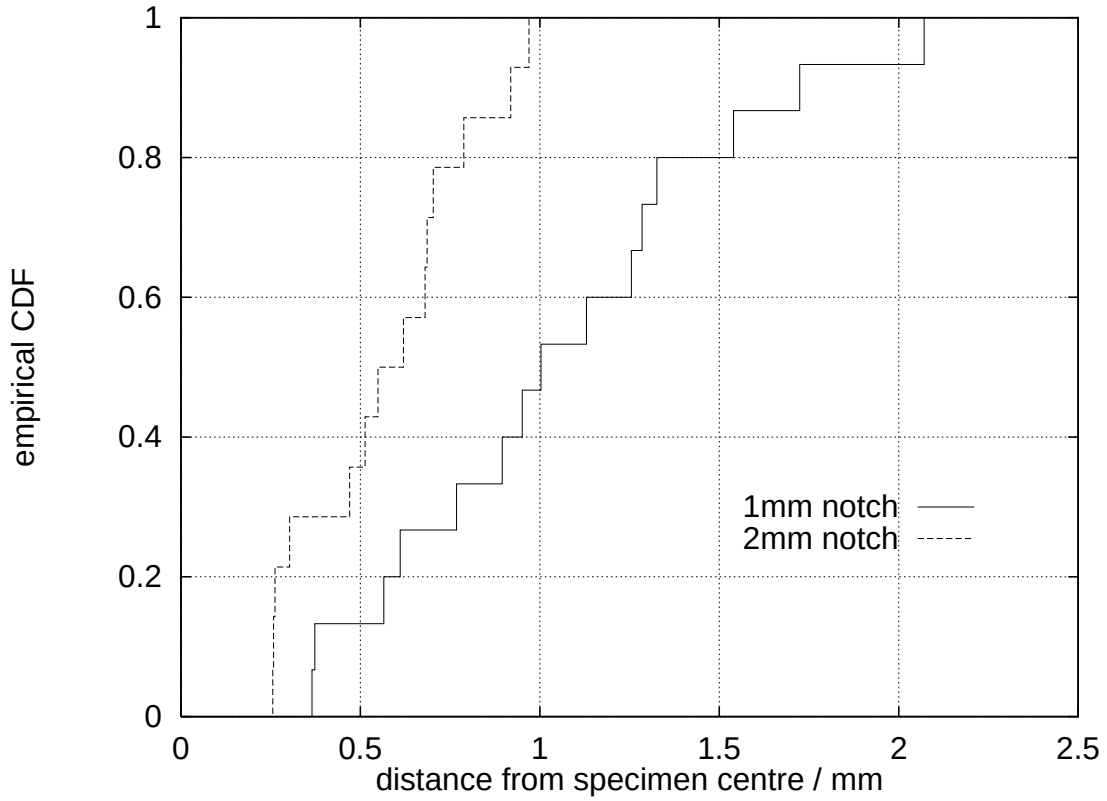

Figure A.33: Rupture origin location distribution of 1 and 2mm notched specimens tested at -150° C.

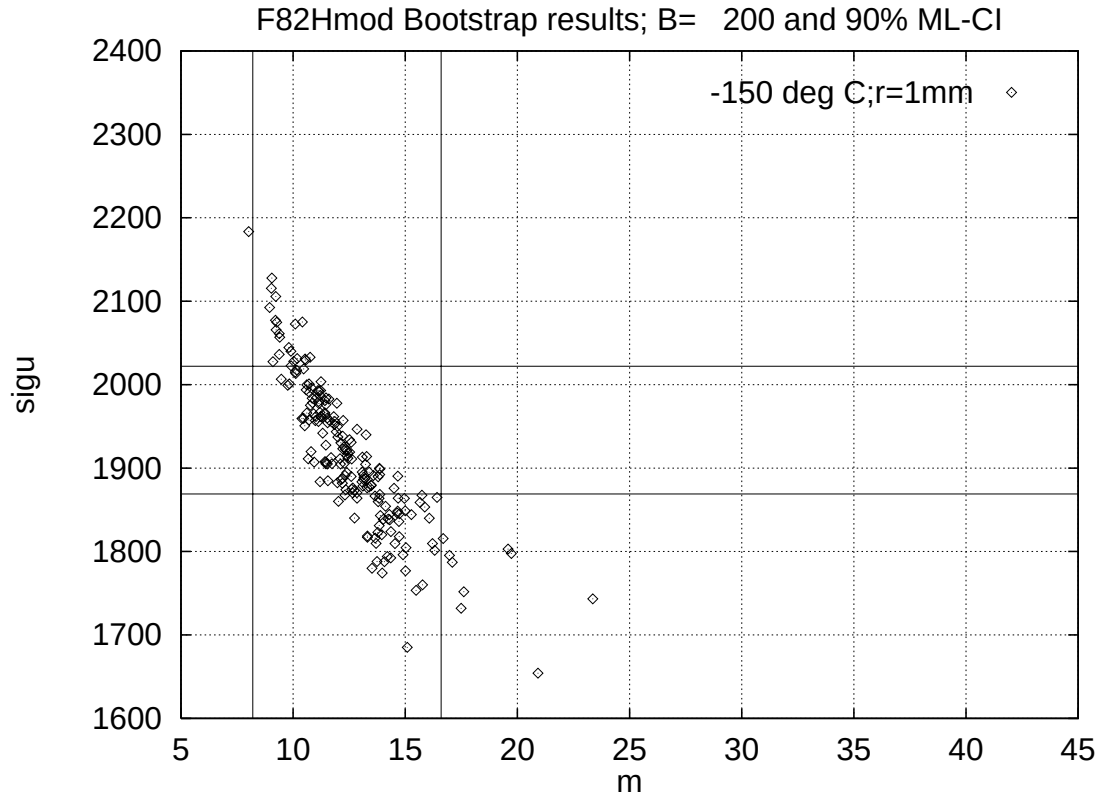

Figure A.34: Bootstrap simulation results for r=1mm notched specimens tested at -150° C. (Auxiliary lines indicate 90% Maximum-Likelihood confidence intervals)

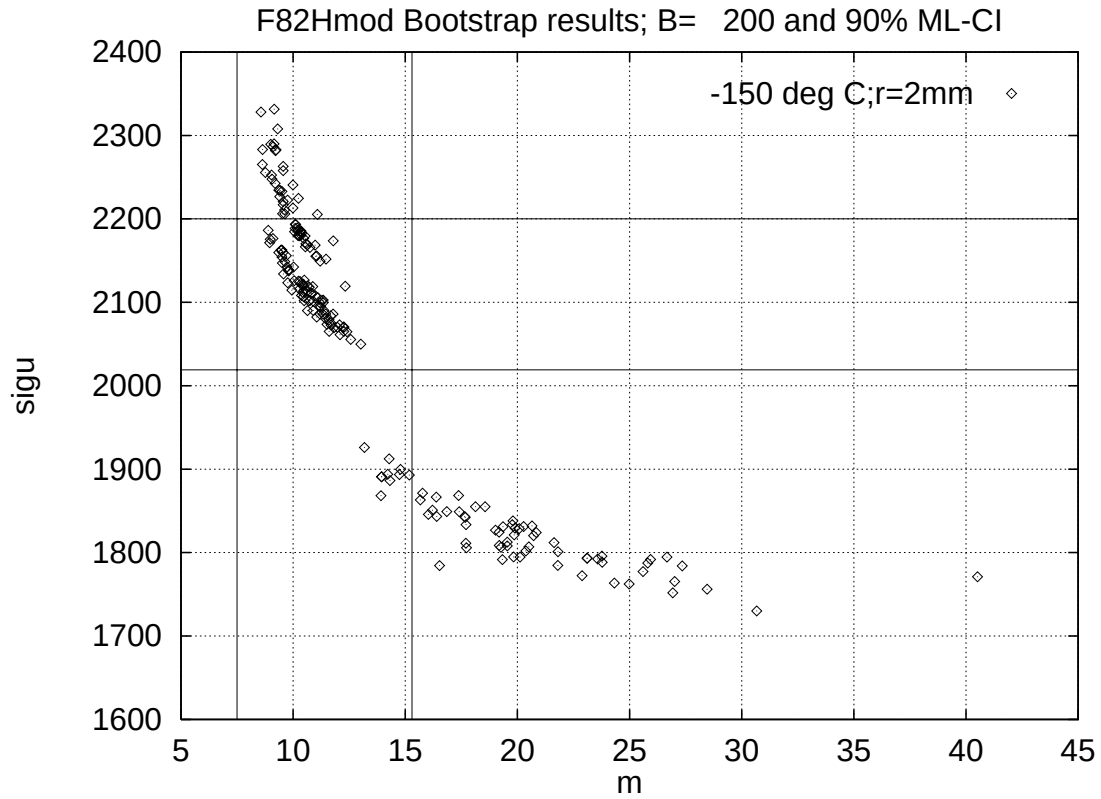

Figure A.35: Bootstrap simulation results for r=2mm notched specimens tested at -150° C. (Auxiliary lines indicate 90% Maximum-Likelihood confidence intervals)

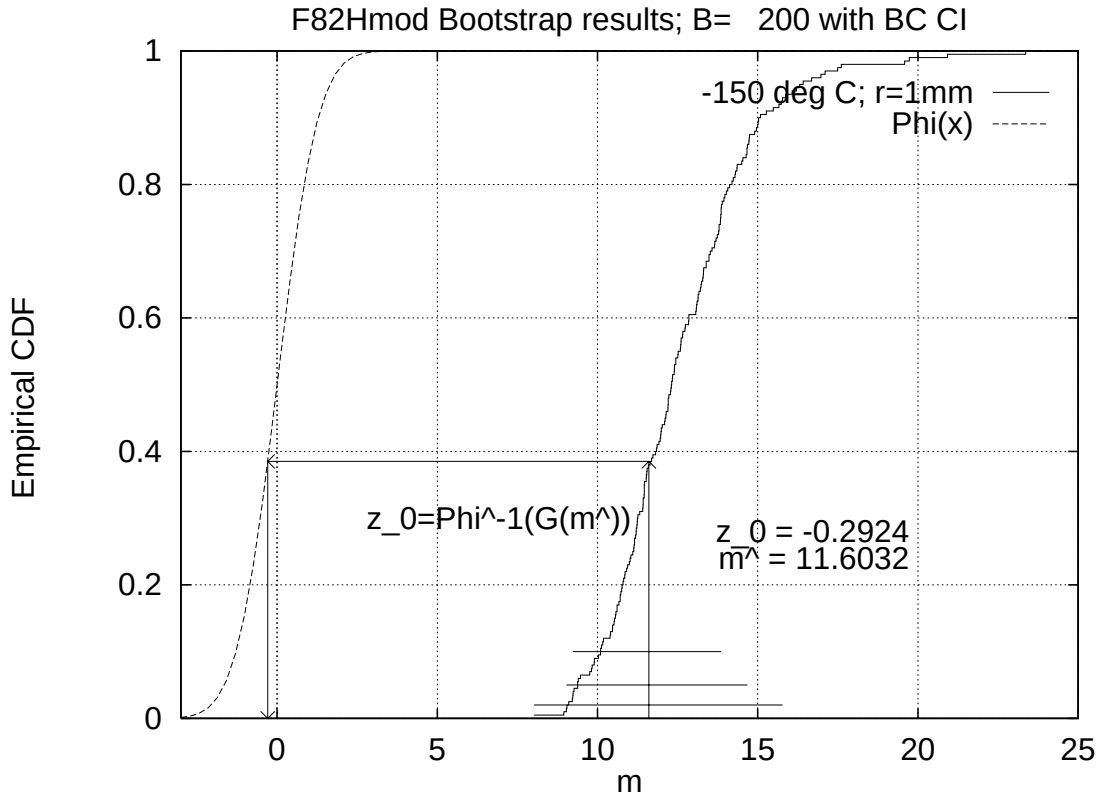

Figure A.36: Bootstrap empirical CDF $\hat{G}(m)$ for r=1mm notched specimens tested at -150° C. (Horizontal lines mark length of bias corrected bootstrap confidence intervals)

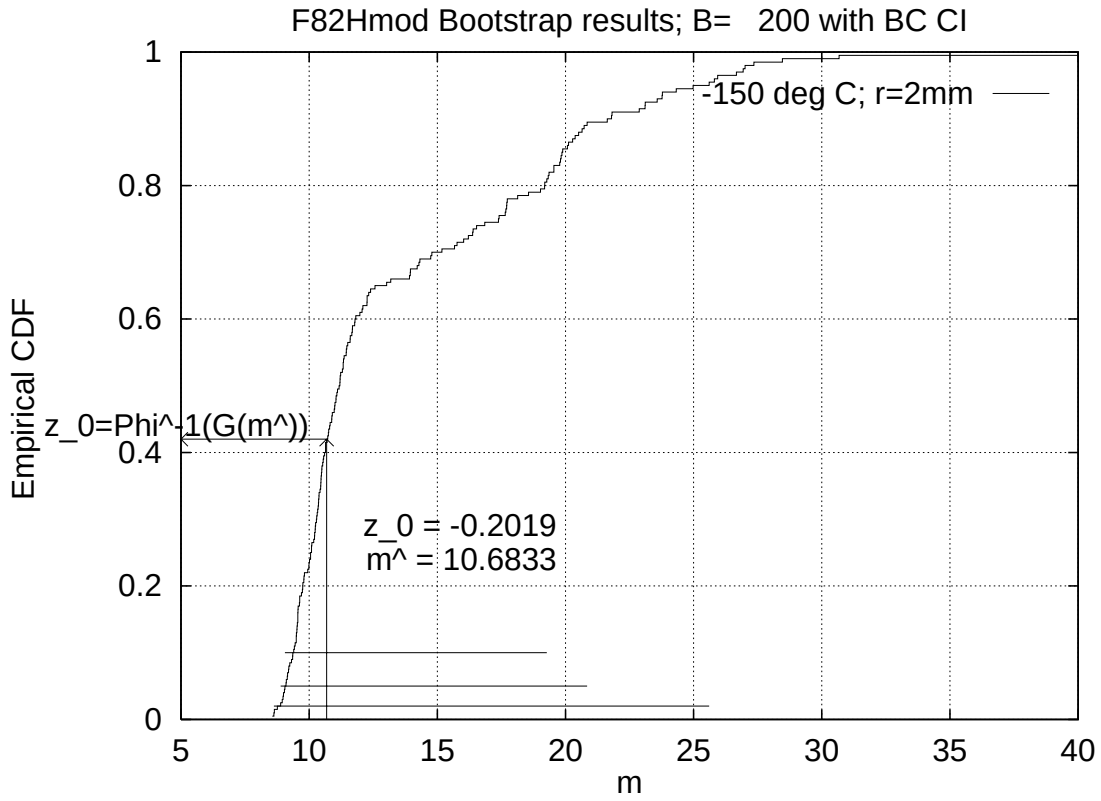

Figure A.37: Bootstrap empirical CDF $\hat{G}(m)$ for r=2mm notched specimens tested at -150° C. (Horizontal lines mark length of bias corrected bootstrap confidence intervals)

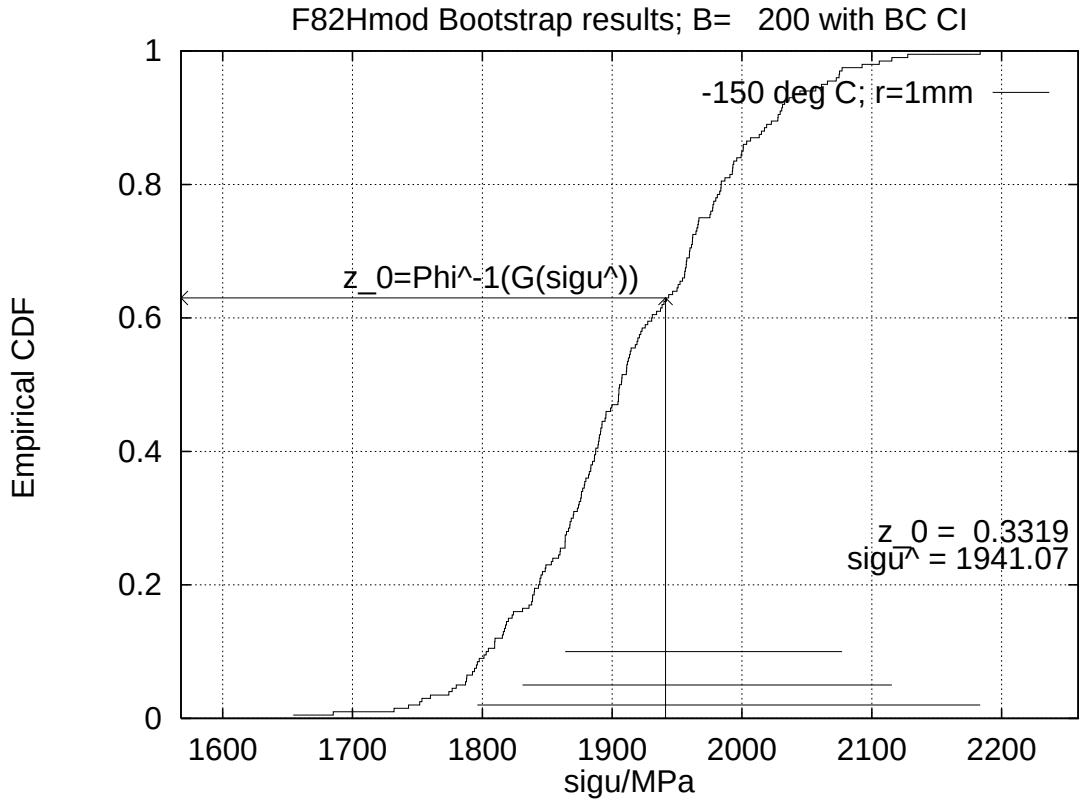

Figure A.38: Bootstrap empirical CDF $\hat{G}(\sigma_u)$ for r=1mm notched specimens tested at -150° C. (Horizontal lines mark length of bias corrected bootstrap confidence intervals)

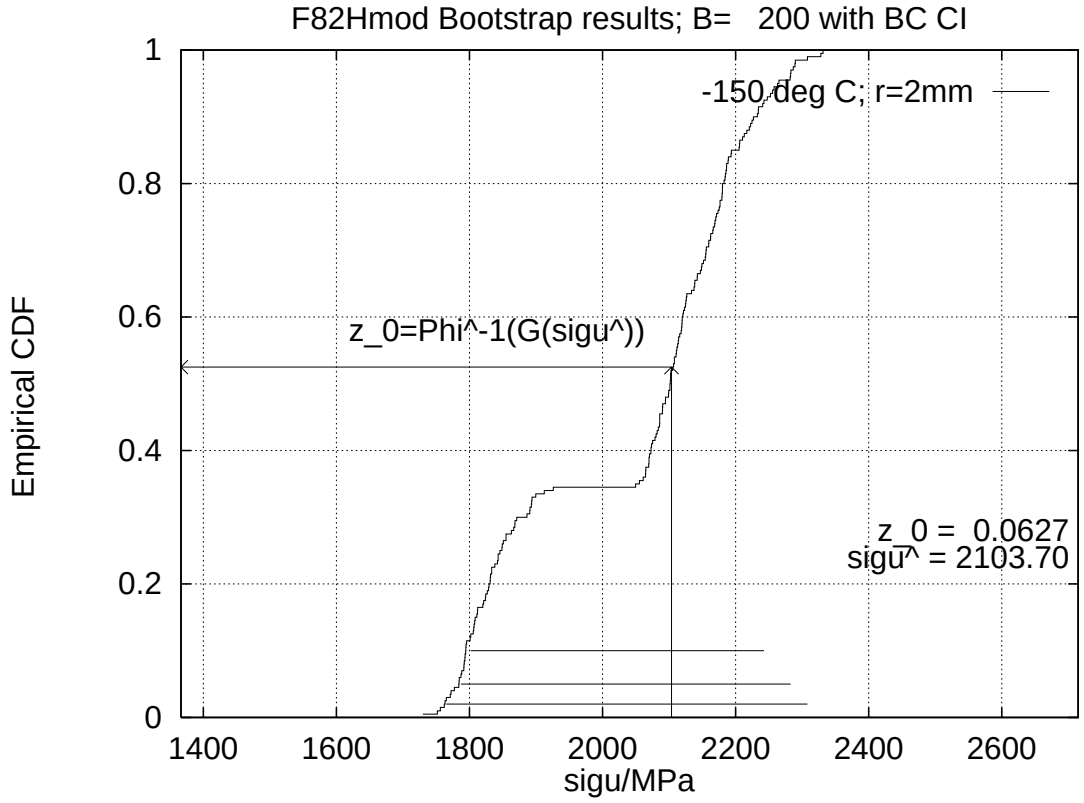

Figure A.39: Bootstrap empirical CDF $\hat{G}(\sigma_u)$ for r=2mm notched specimens tested at -150° C. (Horizontal lines mark length of bias corrected bootstrap confidence intervals)

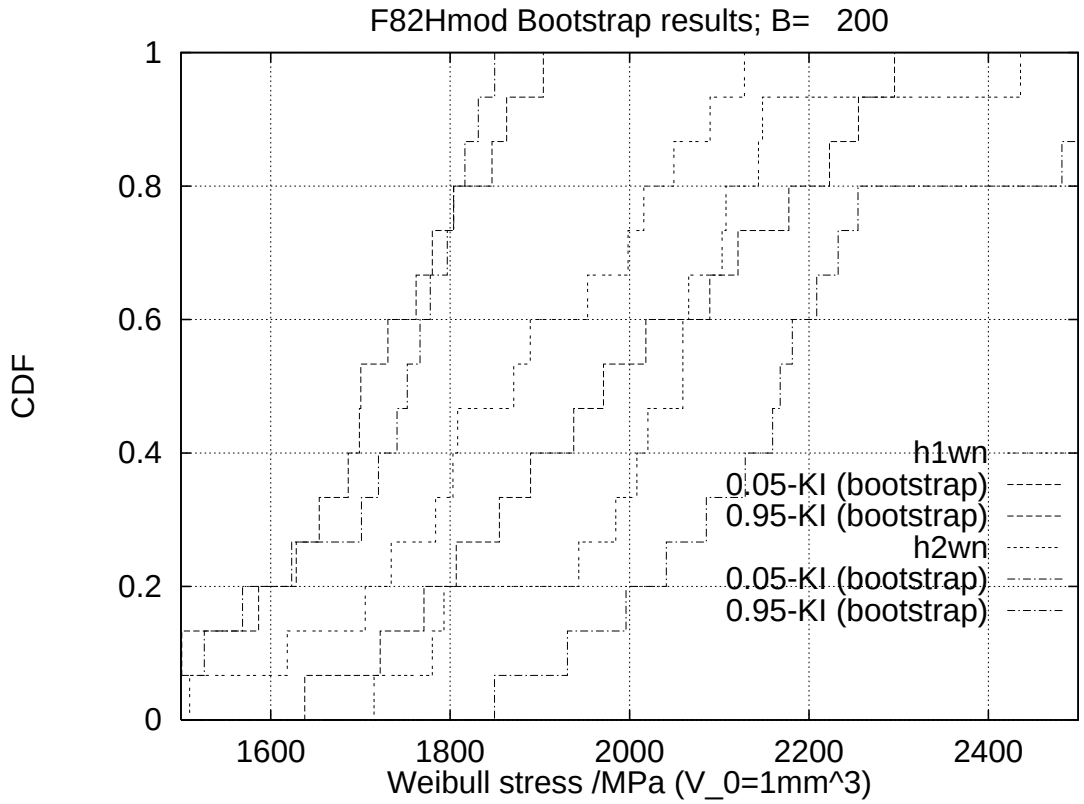

Figure A.40: Bootstrap empirical CDF of σ_W for r=1mm and r=2mm notched specimens tested at -150° C.

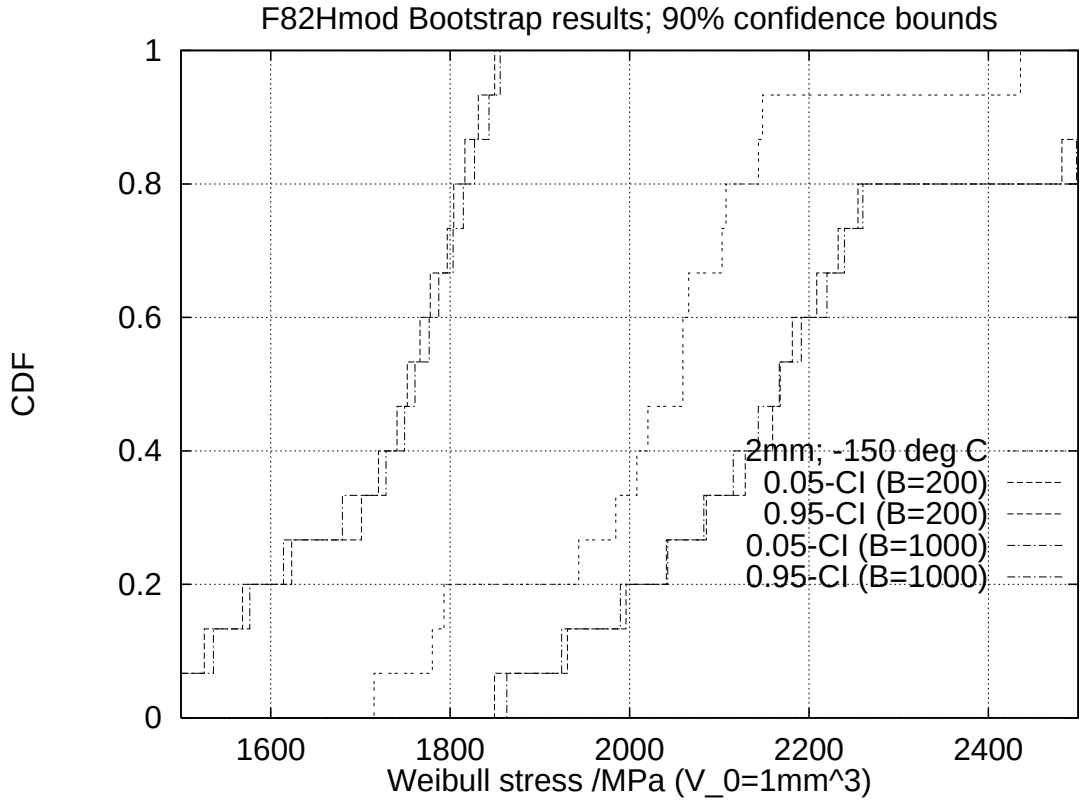

Figure A.41: Influence of bootstrap sample size on CDF confidence limits for r=2mm notched specimens tested at -150° C.

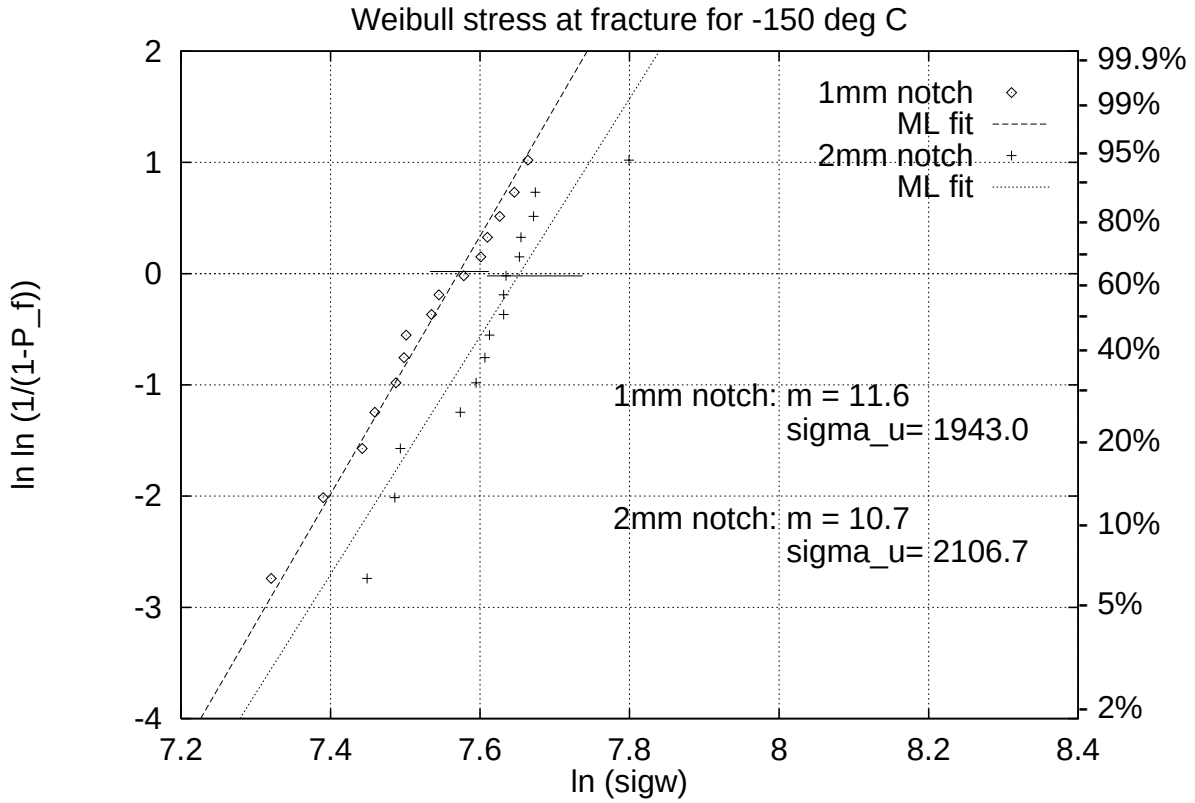

Figure A.42: Results of Weibull stress calculation for -150° C.

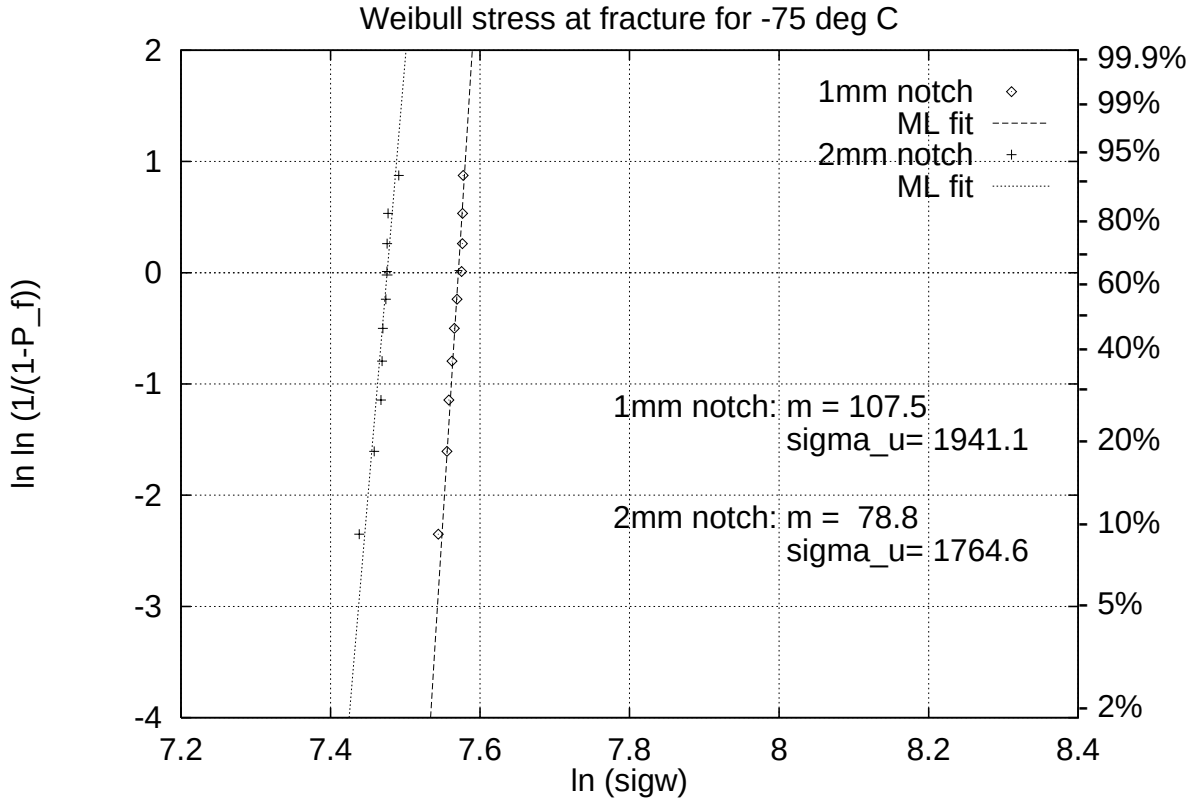

Figure A.43: Results of Weibull stress calculation for -75° C.

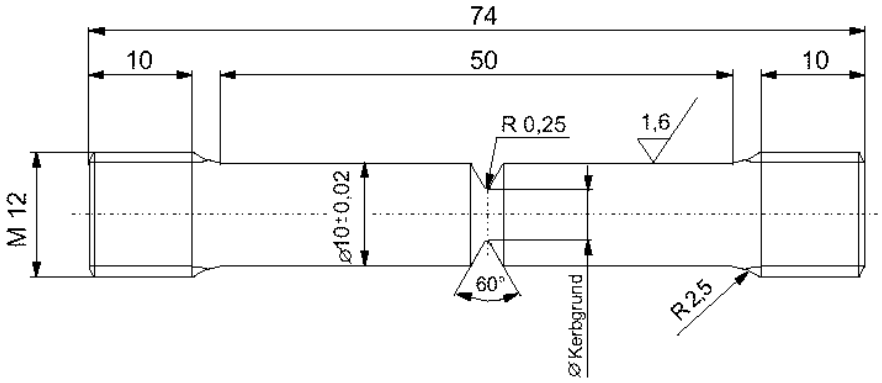

Figure A.44: Geometry of circumferentially pre-cracked bar (RCB) specimens.

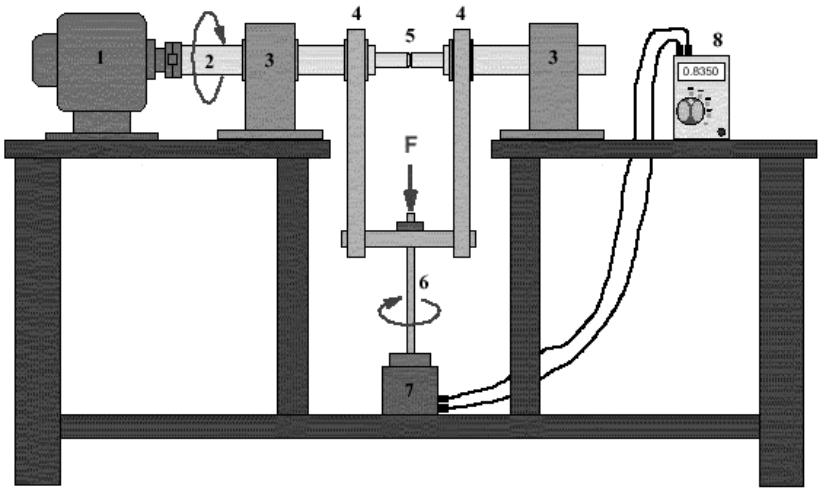

1. motor
2. driving shaft
3. bearing block
4. drive shaft bearing
5. specimen
6. prestressing adjustment
7. load cell
8. voltmeter

Figure A.45: Setup of the pre-cracking rig.

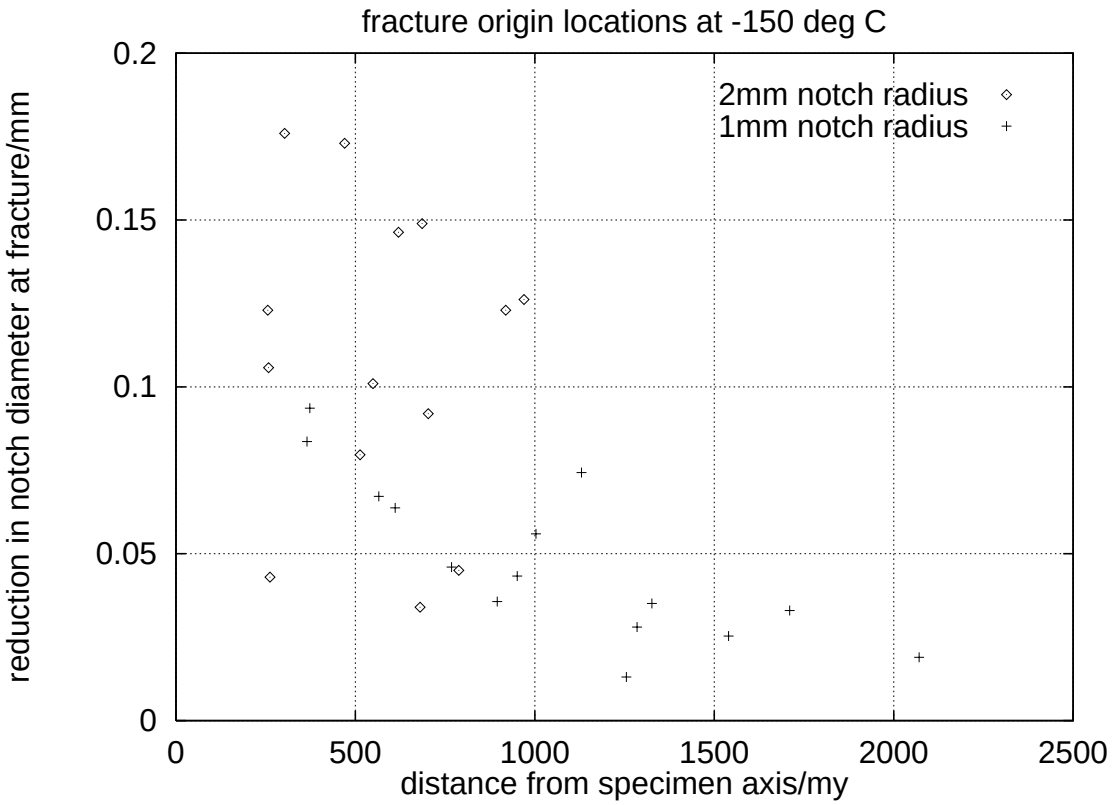

Figure A.46: Fracture origin locations vs. Δd values for r=1mm and r=2mm notched specimens tested at -150° C.

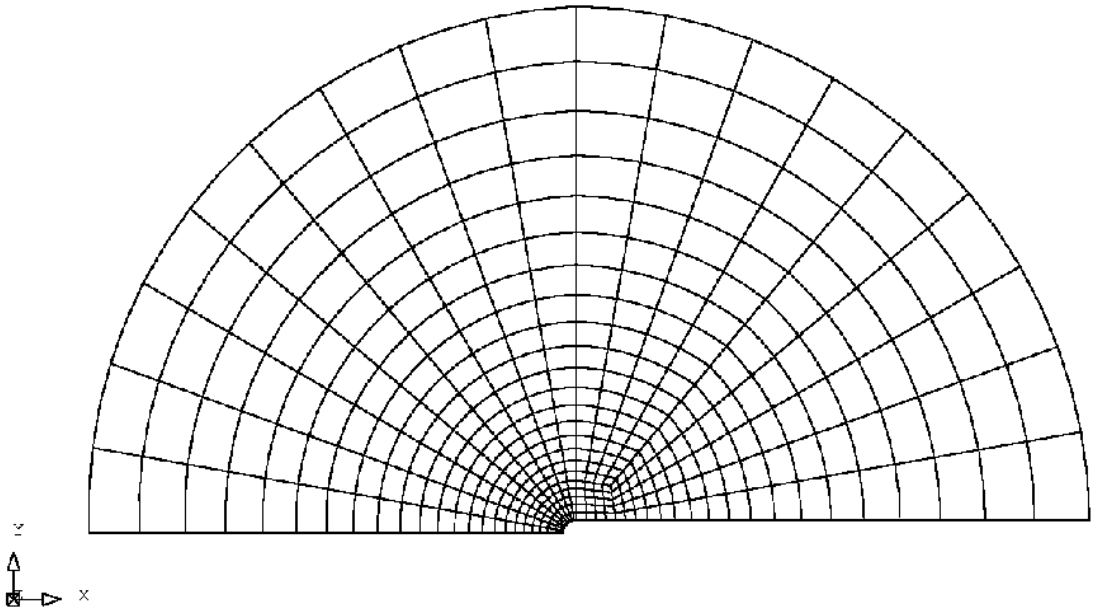

Figure A.47: Crack tip detail of the FE mesh used for the analysis of RCB specimens.

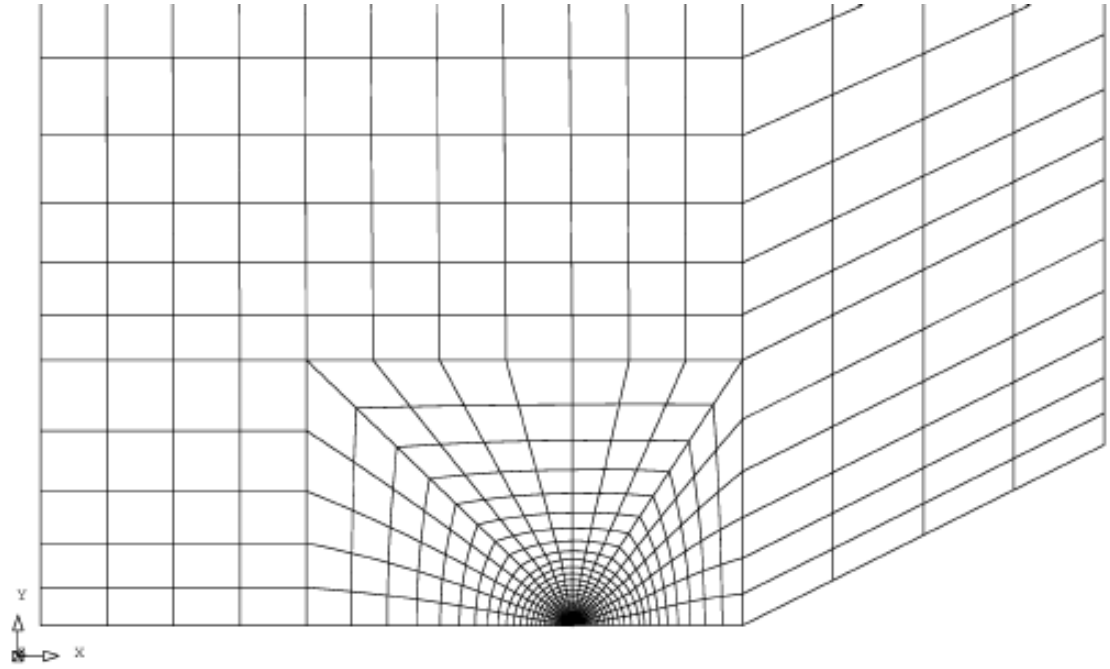

Figure A.48: Overall view at notch of the FE mesh used for the analysis of RCB specimens.

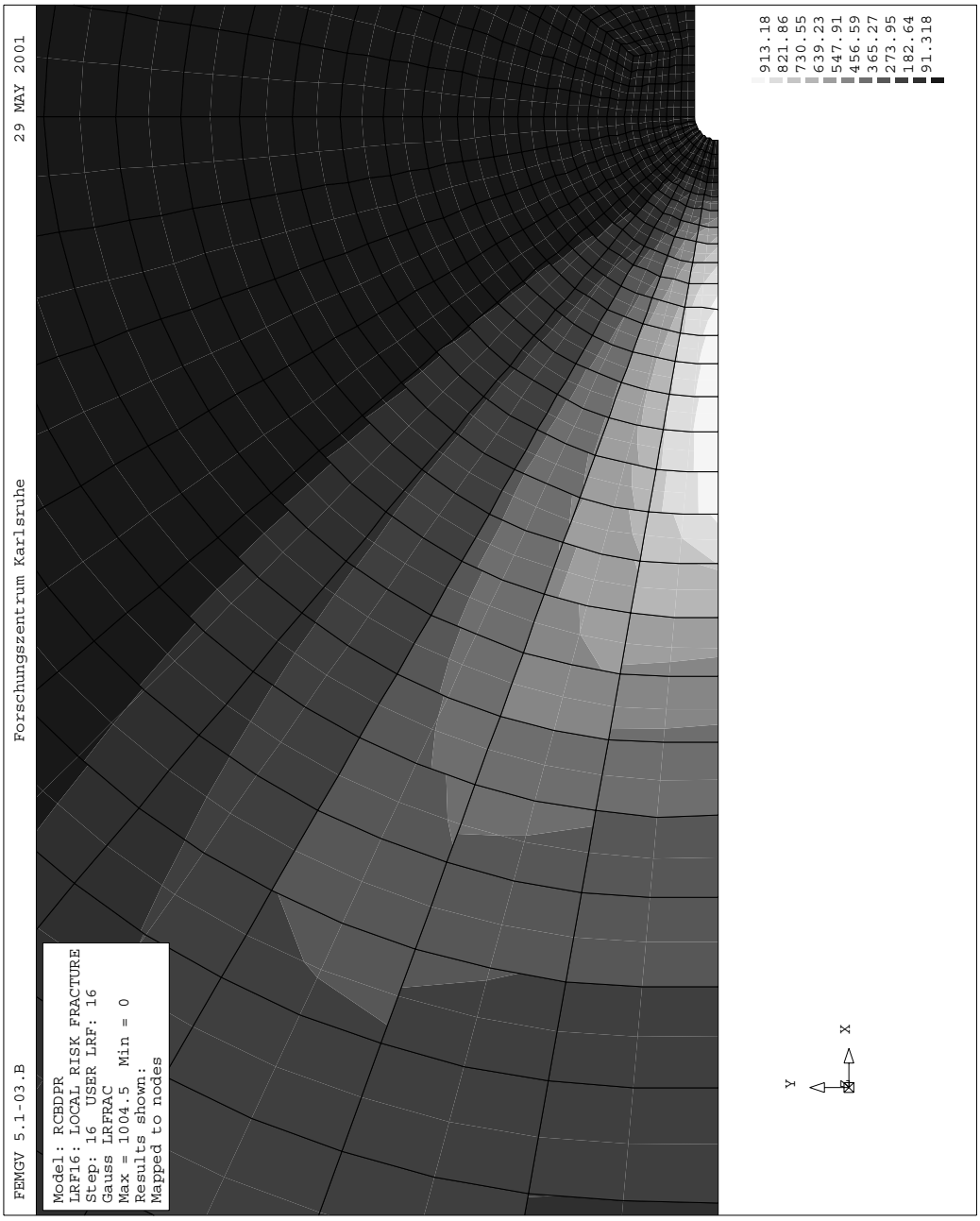

Figure A.49: Local risk of rupture density for deeply notched pre-cracked specimen (parameters correspond to -150° C).

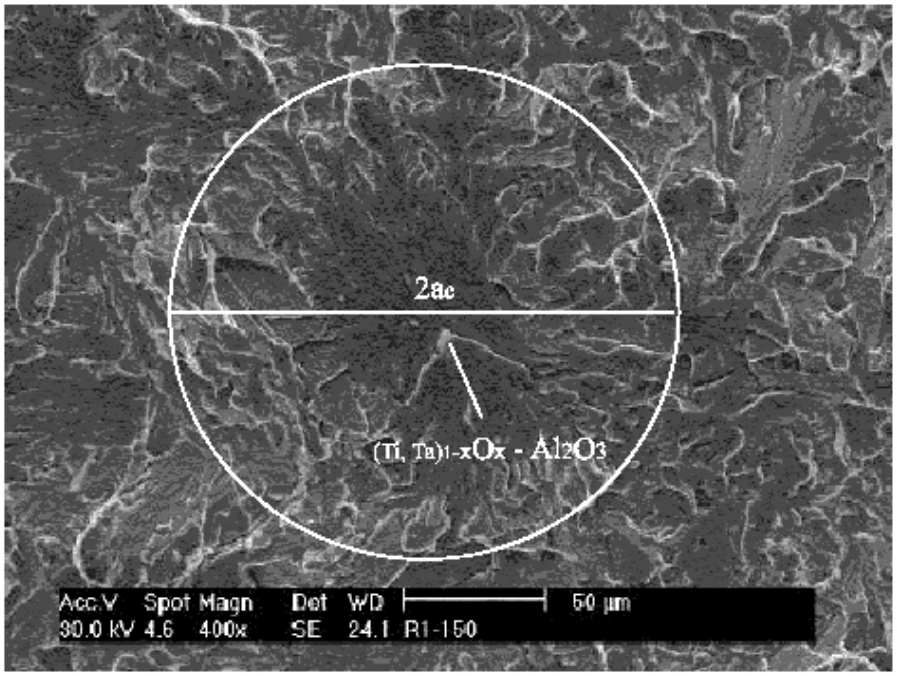

Figure A.50: Sizing of fracture initiation sites for calculation of local fracture toughness values.

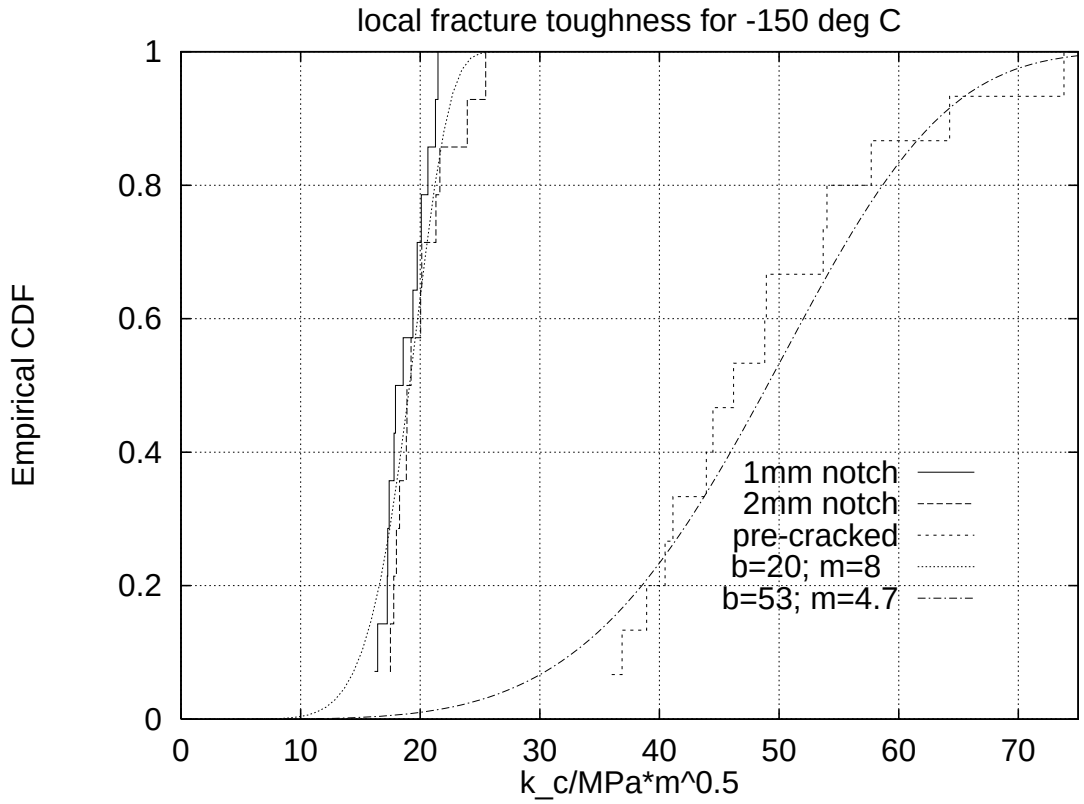

Figure A.51: CDF of local fracture toughness values from notched and pre-cracked specimens at -150° C.

Appendix B

Tables

C	Si	Mn	P	S	Cu	Ni	Cr	Mo
0.09	0.11	0.16	0.002	0.002	<0.01	0.02	7.66	<0.01
V	Nb	B	T.N	Sol. Al	Co	Ti	Ta	W
0.16	<0.01	0.0002	0.005	0.001	<0.01	0.001	0.02	2.00

Table B.1: Composition (wt-%) of F82Hmod; Heat No. 9741

RT			-75° C			-150° C		
K	σ_0	E	K	σ_0	E	K	σ_0	E
820	520	214000	950	570	240000	1200	810	220000

Table B.2: Material parameters K, σ_0 (0.2% offset yield strength), E (units are MPa).

		m	90% ML-CI	σ_u	90% ML-CI
$T = -150^\circ$C	$r = 1$mm	11.6	[8.2, 16.6]	1943.0	[1868.6, 2022.0]
	$r = 2$mm	10.7	[7.5, 15.3]	2106.7	[2019.3, 2199.7]
	$r = 5$mm	78.9	[50.8, 124.5]	1913.2	[1899.9, 1927.1]
$T = -75^\circ$C	$r = 1$mm	107.5	[69.2, 169.5]	1941.1	[1927.9, 1954.7]
	$r = 2$mm	78.8	[50.8, 124.3]	1764.6	[1752.2, 1777.4]
	$r = 5$mm	–	–	–	–

Table B.3: Maximum likelihood results for σ_W-parameters (V_0=1mm^3).

(r=1mm)	ML intervals		BC intervals	
Quantiles	m	σ_u	m	σ_u
0.02	7.4	1846.2	8.0	1863.9
0.05	8.2	1868.6	9.0	1831.0
0.10	9.0	1887.0	9.2	1796.1
0.90	15.5	2003.7	13.9	2183.5
0.95	16.6	2022.0	14.7	2115.5
0.98	17.8	2044.6	15.8	2183.5

(r=2mm)	ML intervals		BC intervals	
Quantiles	m	σ_u	m	σ_u
0.02	6.8	1993.1	8.6	1765.4
0.05	7.5	2019.3	8.9	1787.4
0.10	8.3	2040.8	9.1	1802.0
0.90	14.3	2178.1	19.3	2242.7
0.95	15.3	2199.7	20.8	2282.7
0.98	16.5	2226.4	25.6	2307.9

Table B.4: Maximum likelihood (ML) confidence intervals of -150° C results compared with bias-corrected (BC) bootstrap confidence intervals.

N	$b(N)$
5	0.669
6	0.752
7	0.792
8	0.820
9	0.842
10	0.859
11	0.872
12	0.883
13	0.893
14	0.901
15	0.908
16	0.914

N	$b(N)$
17	0.919
18	0.923
19	0.927
20	0.931
21	0.935
22	0.938
23	0.941
24	0.943
25	0.945
26	0.947
27	0.949
28	0.951

N	$b(N)$
29	0.953
30	0.955
31	0.957
32	0.958
33	0.959
34	0.960
35	0.961
36	0.962
37	0.963
38	0.964
39	0.965
40	0.966

Table B.5: Unbiasing factors $b(N)$

N	$\alpha_1 = 0.02$	$\alpha_1 = 0.05$	$\alpha_1 = 0.10$	$\alpha_2 = 0.90$	$\alpha_2 = 0.95$	$\alpha_2 = 0.98$
5	-1.631	-1.247	-0.888	0.772	1.107	1.582
6	-1.396	-1.007	-0.74	0.666	0.939	1.291
7	-1.196	-0.874	-0.652	0.598	0.829	1.12
8	-1.056	-0.784	-0.591	0.547	0.751	1.003
9	-0.954	-0.717	-0.544	0.507	0.691	0.917
10	-0.876	-0.665	-0.507	0.475	0.644	0.851
11	-0.813	-0.622	-0.477	0.448	0.605	0.797
12	-0.762	-0.587	-0.451	0.425	0.572	0.752
13	-0.719	-0.557	-0.429	0.406	0.544	0.714
14	-0.683	-0.532	-0.41	0.389	0.52	0.681
15	-0.651	-0.509	-0.393	0.374	0.499	0.653
16	-0.624	-0.489	-0.379	0.36	0.48	0.627
17	-0.599	-0.471	-0.365	0.348	0.463	0.605
18	-0.578	-0.455	-0.353	0.338	0.447	0.584
19	-0.558	-0.441	-0.342	0.328	0.433	0.566
20	-0.54	-0.428	-0.332	0.318	0.421	0.549
22	-0.509	-0.404	-0.314	0.302	0.398	0.519
24	-0.483	-0.384	-0.299	0.288	0.379	0.494
26	-0.46	-0.367	-0.286	0.276	0.362	0.472
28	-0.441	-0.352	-0.274	0.265	0.347	0.453
30	-0.423	-0.338	-0.264	0.256	0.334	0.435
32	-0.408	-0.326	-0.254	0.247	0.323	0.42
34	-0.394	-0.315	-0.246	0.239	0.312	0.406
36	-0.382	-0.305	-0.238	0.232	0.302	0.393
38	-0.37	-0.296	-0.231	0.226	0.293	0.382
40	-0.36	-0.288	-0.224	0.22	0.285	0.371
42	-0.35	-0.28	-0.218	0.214	0.278	0.361
44	-0.341	-0.273	-0.213	0.209	0.271	0.352
46	-0.333	-0.266	-0.208	0.204	0.264	0.344
48	-0.325	-0.26	-0.203	0.199	0.258	0.336
50	-0.318	-0.254	-0.198	0.195	0.253	0.328
52	-0.312	-0.249	-0.194	0.191	0.247	0.321
54	-0.305	-0.244	-0.19	0.187	0.243	0.315
56	-0.299	-0.239	-0.186	0.184	0.238	0.309
58	-0.294	-0.234	-0.183	0.181	0.233	0.303
60	-0.289	-0.23	-0.179	0.177	0.229	0.297
62	-0.284	-0.226	-0.176	0.174	0.225	0.292
64	-0.279	-0.222	-0.173	0.171	0.221	0.287
66	-0.274	-0.218	-0.17	0.169	0.218	0.282
68	-0.27	-0.215	-0.167	0.166	0.214	0.278
70	-0.266	-0.211	-0.165	0.164	0.211	0.274

Table B.6: Auxiliary variables for the confidence interval for σ_u

N	$\alpha_1 = 0.02$	$\alpha_1 = 0.05$	$\alpha_1 = 0.10$	$\alpha_2 = 0.90$	$\alpha_2 = 0.95$	$\alpha_2 = 0.98$
72	-0.262	-0.208	-0.162	0.161	0.208	0.269
74	-0.259	-0.205	-0.16	0.159	0.205	0.266
76	-0.255	-0.202	-0.158	0.157	0.202	0.262
78	-0.252	-0.199	-0.155	0.155	0.199	0.258
80	-0.248	-0.197	-0.153	0.153	0.197	0.255
85	-0.241	-0.19	-0.148	0.148	0.19	0.246
90	-0.234	-0.184	-0.144	0.143	0.185	0.239
95	-0.227	-0.179	-0.139	0.139	0.179	0.232
100	-0.221	-0.174	-0.136	0.136	0.175	0.226
110	-0.211	-0.165	-0.129	0.129	0.166	0.215
120	-0.202	-0.158	-0.123	0.123	0.159	0.205

Table B.6: Auxiliary variables for the confidence interval for σ_u (cont'd.)

N	$\alpha_1 = 0.02$	$\alpha_1 = 0.05$	$\alpha_1 = 0.10$	$\alpha_2 = 0.90$	$\alpha_2 = 0.95$	$\alpha_2 = 0.98$
5	0.604	0.683	0.766	2.277	2.779	3.518
6	0.623	0.697	0.778	2.03	2.436	3.067
7	0.639	0.709	0.785	1.861	2.183	2.64
8	0.653	0.72	0.792	1.747	2.015	2.377
9	0.665	0.729	0.797	1.665	1.896	2.199
10	0.676	0.738	0.802	1.602	1.807	2.07
11	0.686	0.745	0.807	1.553	1.738	1.972
12	0.695	0.752	0.811	1.513	1.682	1.894
13	0.703	0.759	0.815	1.48	1.636	1.83
14	0.71	0.764	0.819	1.452	1.597	1.777
15	0.716	0.77	0.823	1.427	1.564	1.732
16	0.723	0.775	0.826	1.406	1.535	1.693
17	0.728	0.779	0.829	1.388	1.51	1.66
18	0.734	0.784	0.832	1.371	1.487	1.63
19	0.739	0.788	0.835	1.356	1.467	1.603
20	0.743	0.791	0.838	1.343	1.449	1.579
22	0.752	0.798	0.843	1.32	1.418	1.538
24	0.759	0.805	0.848	1.301	1.392	1.504
26	0.766	0.81	0.852	1.284	1.37	1.475
28	0.772	0.815	0.856	1.269	1.351	1.45
30	0.778	0.82	0.86	1.257	1.334	1.429
32	0.783	0.824	0.863	1.246	1.319	1.409
34	0.788	0.828	0.866	1.236	1.306	1.392
36	0.793	0.832	0.869	1.227	1.294	1.377
38	0.797	0.835	0.872	1.219	1.283	1.363
40	0.801	0.839	0.875	1.211	1.273	1.351

Table B.7: Auxiliary variables for the confidence interval for m

N	$\alpha_1 = 0.02$	$\alpha_1 = 0.05$	$\alpha_1 = 0.10$	$\alpha_2 = 0.90$	$\alpha_2 = 0.95$	$\alpha_2 = 0.98$
42	0.804	0.842	0.877	1.204	1.265	1.339
44	0.808	0.845	0.88	1.198	1.256	1.329
46	0.811	0.847	0.882	1.192	1.249	1.319
48	0.814	0.85	0.884	1.187	1.242	1.31
50	0.817	0.852	0.886	1.182	1.235	1.301
52	0.82	0.854	0.888	1.177	1.229	1.294
54	0.822	0.857	0.89	1.173	1.224	1.286
56	0.825	0.859	0.891	1.169	1.218	1.28
58	0.827	0.861	0.893	1.165	1.213	1.273
60	0.83	0.863	0.894	1.162	1.208	1.267
62	0.832	0.864	0.896	1.158	1.204	1.262
64	0.834	0.866	0.897	1.155	1.2	1.256
66	0.836	0.868	0.899	1.152	1.196	1.251
68	0.838	0.869	0.9	1.149	1.192	1.246
70	0.84	0.871	0.901	1.146	1.188	1.242
72	0.841	0.872	0.903	1.144	1.185	1.237
74	0.843	0.874	0.904	1.141	1.182	1.233
76	0.845	0.875	0.905	1.139	1.179	1.229
78	0.846	0.876	0.906	1.136	1.176	1.225
80	0.848	0.878	0.907	1.134	1.173	1.222
85	0.852	0.881	0.91	1.129	1.166	1.213
90	0.855	0.883	0.912	1.124	1.16	1.206
95	0.858	0.886	0.914	1.12	1.155	1.199
100	0.861	0.888	0.916	1.116	1.15	1.192
110	0.866	0.893	0.92	1.11	1.141	1.181
120	0.871	0.897	0.923	1.104	1.133	1.171

Table B.7: Auxiliary variables for the confidence interval for *m* (cont'd)